Technische Universität München
Max-Planck-Institut für Quantenoptik

Resonance Fluorescence of an Atom Pair in an Optical Resonator

Andreas Neuzner

Vollständiger Abdruck der von der Fakultät für Physik der Technischen Universität München zur Erlangung des akademischen Grades eines

Doktors der Naturwissenschaften (Dr. rer. nat.)

genehmigten Dissertation.

Vorsitzende(r):		Univ.–Prof. Dr. W. Zwerger
Prüfer der Dissertation:	1.	Hon.–Prof. Dr. G. Rempe
	2.	Univ.–Prof. Dr. J. Finley
	3.	Prof. B. Dayan, Weizmann Institute of Science, Israel (nur schriftliche Begutachtung)

Die Dissertation wurde am 22.12.2015 bei der Technischen Universität München eingereicht und durch die Fakultät für Physik am 14.07.2016 angenommen.

Abstract

In this thesis, scattering of light from two single atoms into the single light mode of an optical resonator is studied experimentally. The atoms are spatially confined to discrete positions by a two-dimensional optical lattice and their positions are detected by single-site resolved fluorescence imaging. The intensity of the light emitted from the resonator and time-resolved correlations thereof are investigated as a function of the optical phase difference with which the atoms couple to the resonator and a perpendicular excitation laser field. Saturation of fluorescence and emission of coherent light is found for constructive interference and non-zero emission characterized by giant photon bunching is found for destructive interference. The latter is explained as a consequence of atomic saturation followed by photon-pair emission.

The described experiments require a high level of control over the internal and external degrees of freedom of the atom. To this end, a series of experiments was conducted to characterize the motional dynamics of the trapped atoms and perturbations of the atoms internal energy eigenstates caused by the presence of the strong dipole trapping light. As results, an avoided crossing of eigenmotions in the trapping potential due to a small non-orthogonality of the lattice with consequences for optical cooling was observed. Breakdown of atomic hyperfine structure caused by the presence of the strong dipole trapping light was predicted theoretically and found in the experiment and a technique was developed to measure the population of individual mechanical eigenstates of the trapping potential in a non-destructive way. This technique was then applied to characterize different classical and non-classical motional states.

Contents

1. Introduction

Quantum mechanics originated from Max Planck's successful description of the black-body spectrum [1]. Planck's analysis hinges on the description of the black body as a set of quantized emitters. The notion of replacing the concept of energy as a continuous quantity with a description of energy as an integer multiple of smallest quanta was later extended to electromagnetic radiation by Albert Einstein [2] in his famous description of the photo effect. The interaction of light and matter has remained at the forefront of scientific interest throughout the development of quantum mechanics.

The laser [3] appeared in 1960 as a source of intense monochromatic radiation that propelled experimental possibilities to a whole new level. Resonance fluorescence of quantum emitters became an intensely studied subject in the nascent field of *quantum optics*, and many of its counterintuitive properties were initially described in theory [4–6] and later observed in the laboratory. The demonstration of a Mollow triplet in the emission spectrum [7,8], anti-bunching of photons [8,9], and recently squeezing in single-emitter fluorescence [10] are milestones in the development of experimental quantum optics.

A second technological breakthrough was marked by the development of techniques to trap and spatially confine individual atoms. Single ions were prepared and observed for the first time in a Paul trap in 1980 [11]. Keeping atoms at rest enabled long observation times. New effects in resonance fluorescence such as discrete quantum jumps [12–14] were observed that had previously gone unnoticed in the atom beam apparatuses that were used thus far.

With the opportunity to isolate and study a single quantum emitter, the addition of a second emitter while maintaining a high degree of control appears as a consequent next step. Studying fluorescence that is emitted from two stationary but spatially separated emitters is analogous to performing a classical Young's double slit experiment [15] in which the slits are replaced by atoms. Atoms, in contrast to slits, are quantum emitters in that they are saturable two-level systems rather than harmonic oscillators and novel interference effects in collective atomic fluorescence have been predicted [16–26].

Yet the experimental challenges are greater than those of single-emitter physics. The relative position of the two emitters appears as a new degree of freedom. Since the observable effects are related to interference between the partial fields that are emitted by both emitters, they are sensitive to this distance on a length scale that is provided by the radiation's wavelength. It was not until 1993 that a seminal experiment, performed in David Wineland's group [27] observed interference fringes in the far field of resonance fluorescence from two ions that were

held at a short distance within the same Paul trap. Three years later, another publication reported the observation of super- and subradiance in a similar two-ion system [28]. Although these two publications attracted a huge interest, no related further experimental work was published in subsequent years.

Complementary to the free-space situation, a large body of theoretical work exists on the collective radiation effects, which are expected from atom pairs that are embedded in the tailored electromagnetic environment provided by optical resonators [29–34]. In contrast to the intrinsically dissipative emission into free space, the light emitted into an optical resonator can have a back-action on the atoms. These effects are not only of fundamental interest but were predicted to have a broad range of applications in *quantum information processing* [34–42].

The combination of a two-ion system with an optical resonator, as described in [27], is complicated by unpredictable surface charges on the resonator's mirrors that tend to interfere with the electrodynamic trap. Still, in a proof-of-principle experiment by Herbert Walther's group, fluorescence light from a single ion could be captured [43]. The authors conclude their paper with the statement

"An equally attractive goal in the area of cavity QED is the simultaneous interaction of two or more ions with a single cavity mode."

Until recently, few similar results were published [44, 45]. The experiments reported in this thesis aim to pick up on the topic of interference phenomena in collective resonance fluorescence in a modern experimental setting. Instead of ions in Paul traps, pairs of neutral atoms in optical lattices are used as scatterers. Thanks to the advent of optical cooling and trapping techniques [46–48], neutral atoms are nowadays routinely levitated in ultrahigh vacuum and cooled to their motional ground state by purely optical means. In contrast to ion traps, optical dipole traps (ODT) enable the holding of atoms close to dielectric surfaces. Atoms as individual optical emitters can thus be coupled to the single light mode of miniaturized Fabry-Perot type resonators. For sufficiently small resonators, the so-called strong-coupling regime [49] of cavity quantum electrodynamics (CQED) is reached, in which the rate at which the emitter and the quantized light field coherently exchange energy dominates all the other (dissipative) rates. The atomic beam and fountain based setups of early cavity QED experiments [50–54] were ultimately succeeded by apparatuses in which single atoms were permanently trapped and strongly coupled to miniaturized Fabry-Perot resonators [55, 56].

As a technological result of this thesis, an existing cavity QED apparatus [57–59] was extended to permit deterministic loading and subwavelength localization of atom pairs. The theoretical paradigm of a pair of identical two-level emitters that are simultaneously coupled to a single cavity mode and a transversal excitation laser with precisely known optical phases was realized. To this end, a two-dimensional optical lattice in the cavity was combined with single-site resolved fluorescence imaging to enable tight spatial confinement of the atoms and exact detection of their (discretized) difference position.

The system was then applied to study the collective scattering of light from an excitation laser into the single cavity mode, as a function of the optical phase difference between the two atoms. For the first time, it was possible to demonstrate interference effects that manifest themselves not only in the observed intensity, but in the photon statistics of the emitted field. A transition from coherent light emission for constructive interference of the two atoms' partial fields to strong super-Poissonian light statistics for destructive interference was found. The latter was explained as a non-linear effect that stems from atomic saturation followed by photon-pair emission; quantitative agreement between a theoretical model and the data was achieved.

The described optical interference experiment requires a high level of control over the internal and external degrees of freedom of the atoms. A series of experiments was conducted to characterize the motional dynamics of the atoms and perturbations of the internal energy structure of the atoms inflicted by the presence of the strong dipole trapping light. AC Stark shifts of electronically excited states were theoretically calculated. In quantitative agreement with theory, the breakdown of atomic hyperfine structure caused by strong tensor polarizabilities of the excited states was observed experimentally. A small non-orthogonality in the two-dimensional optical lattice was observed in single-site resolved fluorescence imaging. The coupling between orthogonal eigenmotions within individual trapping sites caused by this non-orthogonality was observed spectroscopically and unexpected consequences for the dynamics of optical cooling were experimentally observed. Further, a technique was developed that allows to measure the atomic population of individual energy eigenstates of the trapping potential in a non-destructive way. The technique was applied to characterize several classical and non-classical motional states of a single atom. This latter result transcends characterization measurements of the apparatus. While it has no direct relevance for the two-atom experiments, which are the main result of this thesis, the novelty of the results warrants discussion in a separate chapter.

This thesis is organized as follows: A general overview of the apparatus and experimental techniques that were commonly used in all of the described experiments is discussed in Chapter 2. The theory of AC Stark shifts is outlined in Chapter 3 and spectroscopic results are presented and discussed. Chapter 4 describes the geometry of the trapping potential and discusses motional dynamics of the trapped atoms. A characterization of the eigenmotions via Raman sideband transitions is carried out and the experimentally observed formation of stable and unstable trapping regions is identified as a consequence of motional coupling. Chapter 5 discusses the technique used to measure the atomic population of the trapping potential's energy eigenstates. The topics covered in this chapter are self-contained and an outlook for potential future research possibilities enabled by these findings is discussed separately at the end of chapter 5. Chapter 6 describes the two-atom interference experiments in theory and experimentally. A summary of the main results together with an outlook for future experimental opportunities conclude the manuscript.

2. Experimental Apparatus and Techniques

2.1. Overview

This chapter summarizes important experimental techniques and properties of the experimental apparatus that are relevant to all subsequent chapters. Where applicable, references to earlier theses are provided. Such topics are covered in detail only when warranted by a significant gain in theoretical understanding or achieved experimental performance.

Figure 2.1 shows the main building blocks of the apparatus. At the heart of the setup is a Fabry-Perot-type high finesse resonator [60] that is built into an ultra-high vacuum apparatus. A piezo-ceramic tube that is used to stabilize the resonator length, a rubidium dispenser, and a mirror that is required to generate a magneto-optical trap are the only additional elements in the vacuum chamber [61]. Atoms are trapped in a two-dimensional optical lattice within the resonator, which is formed by two intersecting standing wave beams. The first standing-wave beam is a TEM_{00} mode of the cavity, with a wavelength of 772.37 nm. The second beam traverses the cavity along the x-axis and intersects the intracavity trap close to the resonator's center. After traversing the cavity and the vacuum chamber, the beam is retroreflected with a cat-eye setup to form a standing wave.

Additional beams are shone onto the trapped atoms at 45° in the xy-plane. One of these beams (the −45° beam) is impinged in a running-wave configuration and dumped into a beam block after it has traversed the vacuum chamber. It is linearly polarized with its electric field oriented along the cavity axis (z-axis). The −45° beam is used for manipulation and detection of the internal atomic state (see Chapter 2.5). The second beam in this plane (the +45° beam) is linearly polarized and retroreflected after transmission through a $\lambda/4$ wave plate yielding a lin⊥lin polarization lattice. This beam is used for optical cooling of the atoms with an optical molasses [61]. During optical cooling, atomic fluorescence light is emitted into free space. A small fraction of this light is collected through an objective with a high numerical aperture that looks down on the atoms along the y-axis (see Chapter 2.4). The design of this objective resulted from a Master's thesis [62] and details of the design can be found therein. A partly reflective beam sampler is used behind the objective to overlay light with the imaging beam path that is focused downward into the plane of the

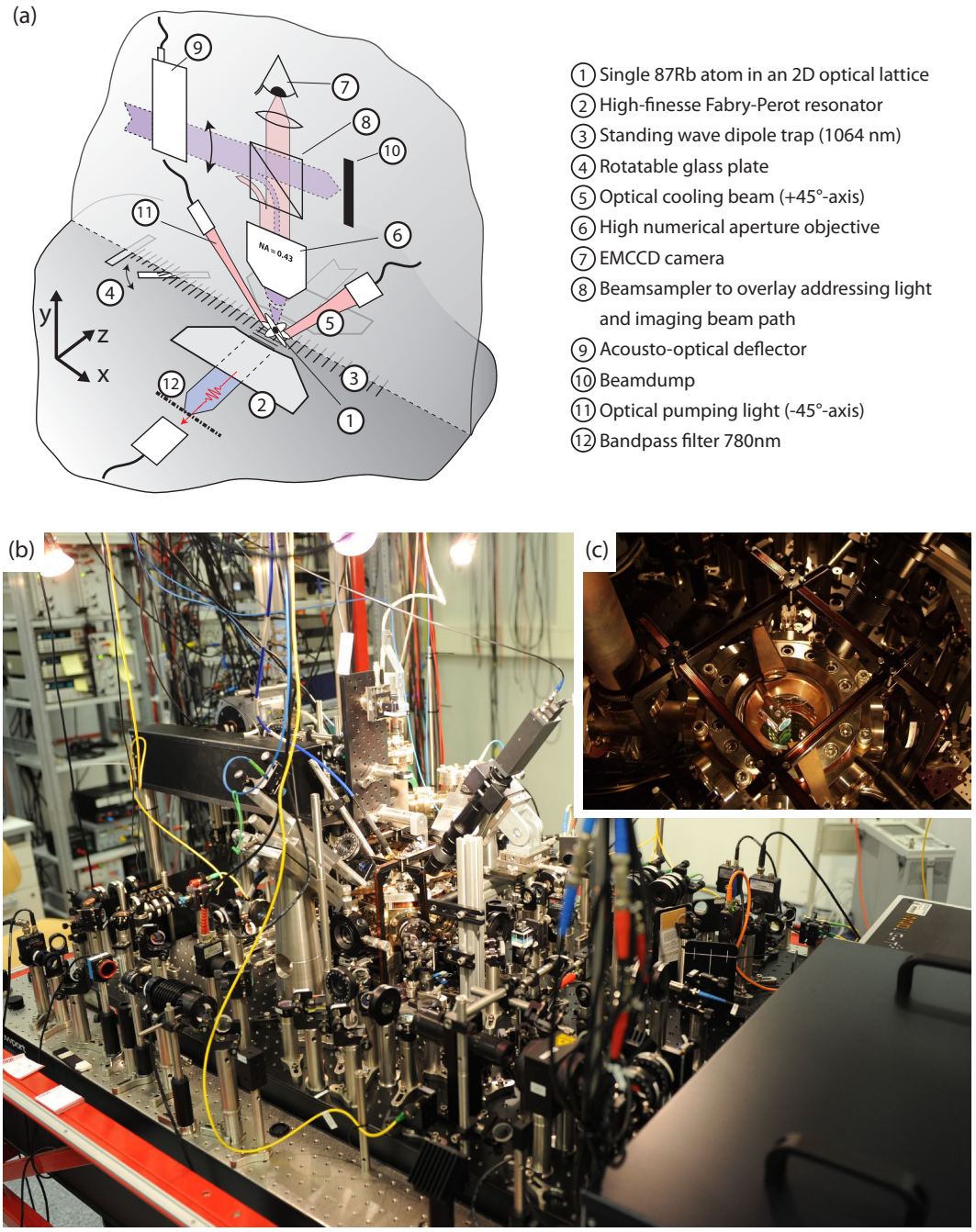

Figure 2.1.: Experimental Setup (a) Sketch of the main parts of the experimental setup. Not shown are the laser system, experimental control system and the detection setup. (b) Photograph of the setup that covers the parts shown in panel (a). All remaining parts sit on another optical table. (c) Close-up of the vacuum chamber during assembly of the surrounding optics.

atoms. An acousto-optical deflector allows stearing the generated spot along the x-axis. By selectively removing excess atoms with resonant light from an initial unsorted sample, a deterministic atom loading procedure was developed. Details of this technique are provided in Chapter 2.3.

The light that is emitted from the cavity through the outcoupling mirror is filtered to remove the intracavity trapping light at 772 nm. The remaining light is coupled into a single-mode fibre with a coupling efficiency of 90 %. This optical fibre is connected to a detection setup consisting of four single-photon detection modules with a quantum efficiency of 55 %. In the detection setup, the light is split by a non-polarizing beam splitter into two identical detection paths. Each of the two paths consist of a motorized $\lambda/4$ and $\lambda/2$ wave plate in front of polarizing beam splitter and two single-photon detection modules. Each path forms a single-photon Stokes polarimeter. An additional beamsampler allows to overlay an auxiliary lightfield propagating backwards from the detection setup through the fibre towards the resonator. This field is used for spectroscopy of the atom-resonator system in reflection [63]. Details of the detection setup can be found in reference [59].

A total of five external-cavity diode lasers were used in combination with acousto-optical modulators to provide all of the light fields used in the described experiments. The lasers are referenced to a frequency comb thus eliminating the need for transfer cavities [57]. The radio-frequency signals, which are needed as local oscillators for the laser locks and to drive the acousto-optical modulators, are derived from a versatile, direct digital synthesis generator that was designed over the course of this thesis. All of the relevant frequencies covering the whole spectrum from radio frequency to infrared light are thus related to each other through digital counting. The laser system was set up on a separate table and connected to the actual apparatus with polarization-maintaining[1] single-mode optical fibres.

2.2. The Resonator

The resonator consists of two super polished substrates that are made of fused silica. A high-reflection coating is applied to one and an antireflection coating with a residual reflectivity of approximately 0.02 % [60] is applied to the other side. The substrates have a maximum diameter of 7.74 mm and are milled to a conical shape that leaves a mirror facette with a diameter of 1.5 mm. The curvature of the concave mirrors is 50 mm and the reflectivities of the mirrors are intentionally chosen asymetrically. The high-reflective mirror on one side is specified to have a residual transmission of $T_{\mathrm{HR}} = 4\,\mathrm{ppm}$ and the output-coupling mirror is specified with $T_{\mathrm{OC}} = 101\,\mathrm{ppm}$. The asymmetric design causes

[1] The only non-PM fibre connects the cavity output and the detection setup, as this fibre must preserve all polarization states in contrast to two guided linearly polarized modes in pm fibres.

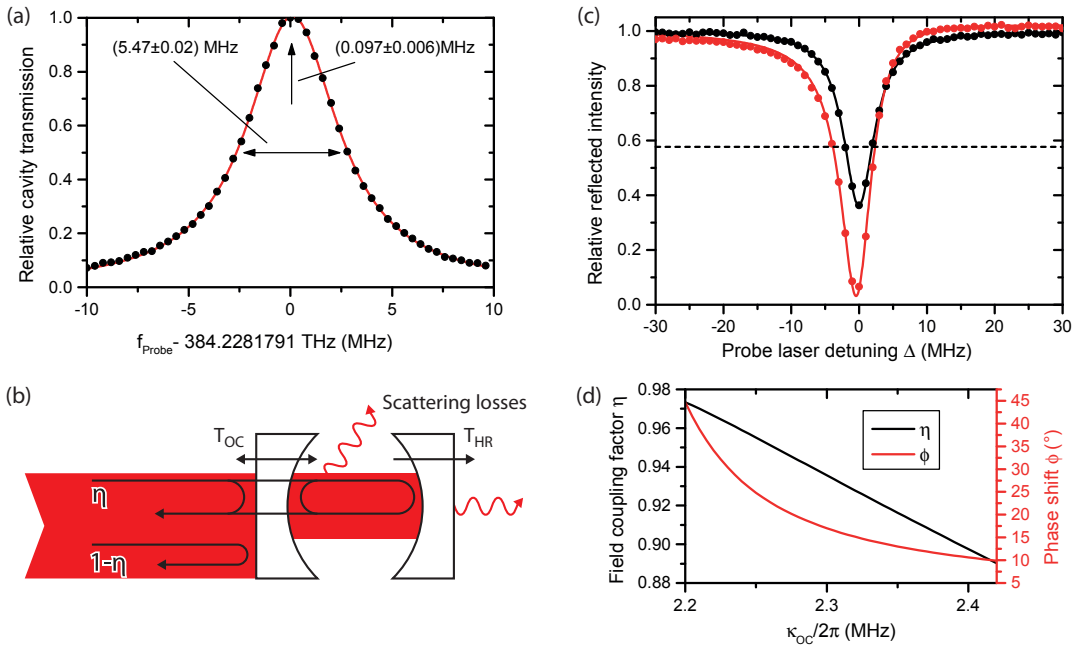

Figure 2.2.: Spectroscopy of the empty resonator (a) Spectroscopy of the stabilized resonator in transmission. The red line is a Lorentzian fit to the data. (b) Interference of coupled and uncoupled partial fields in a reflection measurement. (c) Measurement of the cavity reflectivity with a single-mode fibre in the case of a well-aligned fibre (black dots) or an intentionally misaligned fibre (red dots). The dotted lines are a fit of the described model to the data. The dashed line marks the theoretical value of $R = 0.577$ on resonance assuming $\kappa_{\mathrm{OC}} = 2\pi \cdot 2.42\,\mathrm{MHz}$ and perfect mode matching. (d) Range of output coupler transmission that could be explained by the described model.

photons that are lost from the cavity mode to be emitted predominantly through the outcoupling mirror, where they are fibre-coupled and guided to the detection setup. The mirrors are built into a piezo tube such that the two mirrors enclose a distance of 0.5 mm. Since the distance of the mirrors is small compared to the curvature of the mirrors, the TEM_{00} cavity mode is almost cylindrical; its waist ($1/e^2$ intensity radius) is $w_0 = 29.6\,\mu\mathrm{m}$ with a Rayleigh range of $z_0 = 3.5\,\mathrm{mm}$. The light that creates the repulsive intracavity trap is coupled into the resonator through the high reflector. Sidebands modulated onto this beam are used to generate an error signal for the length stabilization with the Pound-Drever-Hall technique [64] which uses the piezo-ceramic tube as an actuator.

Characterization measurements of the resonator were carried out complementary to earlier measurements [60]. To this end, spectroscopy light was coupled into the stabilized resonator through the high reflector. The frequency of this light was resonant with a longitudinal mode that was different from that used to stabilize the resonator length. Figure 2.2(a) shows the measured

power of the transmitted light as a function of the laser's frequency with a Lorentzian fit to the data. The resonator length was stabilized to light with a frequency of 388.14343365 THz and the frequency difference of the two longitudinal modes was 3.9152545 THz. From this value, a free spectral range of $\mathrm{FSR} = c/2L = 301.173\,\mathrm{GHz}$ and a value for the length of $L = 497.7\,\mu\mathrm{m}$ was calculated. Due to residual fluctuations of the length stabilization, the observed linewidth is an upper limit for the intrinsic resonator linewidth; thus a lower bound for the resonator finesse of $\mathcal{F} = \mathrm{FSR}/\mathrm{FWHM} = 55{,}059$ was found. This corresponds to total round-trip losses of $L_{\mathrm{tot}} = 2\pi/\mathcal{F} = 114\,\mathrm{ppm}$.

The field decay rate of the cavity $\kappa = L_{\mathrm{tot}} \cdot \mathrm{FSR}/2 = 2\pi \cdot 2.75\,\mathrm{MHz}$ can be expressed as a sum of contributions $\kappa = \kappa_{\mathrm{OC}} + \kappa_{\mathrm{Loss}}$, where κ_{OC} is the partial field decay rate due to transmission through the outcoupling mirror; κ_{Loss} subsumes scattering losses, absorption losses and transmission through the high reflector. While transmission spectroscopy of the cavity only permits measurement of the total κ, spectroscopy in reflection is sensitive to the contribution of κ_{OC} to κ [63].

In the following, a model of cavity reflectivity is described, which incorporates the effects of imperfect mode matching of the probe light to the resonator. Figure 2.2(b) shows a sketch of the partial fields that are involved in a cavity reflection measurement. The incident field is the sum of one partial field that couples perfectly to the resonator mode and has a relative strength of η, and a remaining field with a relative strength of $1 - \eta$ that does not interact with the cavity mode and is reflected directly off of the output-coupling mirror. The existence of two partial fields may be a consequence of the incident beam being transversally displaced from the mode, as shown in Fig. 2.2(b). The complex field reflectivity $r(\Delta)$ as a function of the detuning Δ of the coupled field from the cavity resonance is calculated by finding self-consistent values for the incident, reflected and circulating fields and is:

$$r(\Delta) = 1 - \frac{2\kappa_{\mathrm{OC}}}{\kappa + i\Delta}. \tag{2.1}$$

After the reflected light propagates through free space towards the detector, the far field images of the two partial reflections will overlap and form a complex interference pattern. A free-space detector with a large enough sensitive area will integrate across the entire interference pattern and the effect of an uncoupled partial field will be reduced to a constant background signal [63]. A single-mode fibre will however pick a small part from the interference pattern and the observed signal will thus be sensitive to the phase between the reflected coupled and uncoupled fields. Normalized to the observed intensity for $\Delta \to \infty$, the following expression determines the generalized reflectivity:

$$R(\Delta) = \frac{|\eta\, r(\Delta) + (1-\eta)e^{i\phi}|^2}{\eta^2 + (1-\eta)^2 + 2\eta(1-\eta)\cos(\phi)} \tag{2.2}$$

The quantity ϕ describes a constant phase between the coupled and uncoupled

field that exists even within the limit of $\Delta \to \infty$[2]. Figure 2.2(c) shows a measurement of the cavity reflectivity for a well-aligned fibre that picks up the reflected signal (black dots) and an intentionally misaligned fibre (red dots). The dashed line at $R = 0.577$ marks the theoretical value expected for probing on resonance, assuming perfect coupling efficiency ($\eta = 1$) and $\kappa_{\mathrm{OC}} = 2\pi \cdot 2.42\,\mathrm{MHz}$. Both datasets drop significantly below this value. The effect of an uncoupled field is most pronounced on resonance ($\Delta = 0$), as the reflected coupled field will be out of phase with the incident. By intentionally misaligning the fibre, the ratio of the fields' strength is changed. At equal field strength, perfect extinction is observable at a suitable detuning. The dataset shown by the red dots was collected close to this situation. The solid lines are calculated by fitting equation 2.2 to the data, assuming $\kappa_{\mathrm{OC}} = 2\pi \cdot 2.42\,\mathrm{MHz}$, and fitting η and ϕ to the data. All of the features that are present in the data, including an asymmetric broadening of the observed line and shift of the line center, are reproduced. Similar observations were recently reported in the context of microscopic fibre cavities [65] and the same effect was proposed to be exploited for cavity length stabilization [66].

Unfortunately, the described method cannot be used as a tool to measure κ_{OC} due to a large covariance between the parameters κ_{OC}, η, and ϕ. Figure 2.2(d) shows the value of parameters η and ϕ, which were found by fitting the model to a dataset with a well-aligned fibre as a function of the assumed κ_{OC}. The quality of the achieved fits was equally good throughout the parameters range shown in the figure. The total decay rate κ was kept constant, such that a smaller κ_{OC} corresponds to increased scattering losses. A smaller value of κ_{OC} yields a greater η, as the small observed minimum reflectivity is now explained by the increased losses. On the other hand, ϕ rises to unrealistic values in order to reproduce the asymmetry that is present in the data. The values found for the theoretical value $\kappa_{\mathrm{OC}} = 2\pi \cdot 2.42\,\mathrm{MHz}$ (corresponding to $T_{\mathrm{OC}} = 101\,\mathrm{ppm}$) are $\eta = 0.89$ and $\phi = 0.173$. These values appear reasonable and were used for further application of the model presented in this Chapter in the context of reflection spectroscopy of coupled single- and two-atom cavity systems (see chapter 6.4).

The coherent light-matter coupling strength that is relevant to the cavity QED experiments is given by:

$$g = \sqrt{\frac{\omega_c}{2\epsilon_0 V \hbar}}\mu_{ge}, \tag{2.3}$$

where μ_{ge} is the atomic transition dipole moment, ϵ_0 is the vacuum permittivity, ω_c is the cavity frequency, and the mode volume of the cavity (V) is $\pi w_0^2 L/4 =$

[2] In contrast to the phase which is imprinted onto the coupled part of the field by the resonator, the phase ϕ does not vanish for infinite detuning. Its origin is probably mostly geometric, as the paths that are taken by the two partial fields towards the pick-up fiber differ.

Cavity length L	$497.708\,\mu$m
Radius of curvature	50 mm
TEM_{00} mode waist w_0	$29.6\,\mu$m
Rayleigh range z_0	3.5 mm
Free spectral range	301.173 GHz
Finesse $\mathcal{F}$	55059
Round-trip losses L_{tot}	114 ppm
Transmission of output coupler T_{OC}	101 ppm
$(\kappa, \kappa_{\mathrm{OC}}, \gamma, g)$	$2\pi \cdot (2.75,\ 2.42,\ 3.03,\ 7.62)$ MHz

Table 2.1.: Properties and important cavity QED properties. The value for γ ist taken from [67] and the value for g is the experimentally found value that deviates from the theoretical maximum value by only 3 %.

$3.4249 \cdot 10^{-13}\mathrm{m}^3$ ($= 721000\,\lambda^3$). On the cycling transition $|5S_{1/2}, \mathrm{F}{=}2, m_F{=}2\rangle \leftrightarrow |5P_{3/2}, \mathrm{F}{=}3, m_F{=}3\rangle$ of ^{87}Rb, the transition dipole moment is $\mu_{ge} = 2.53444(52) \cdot 10^{-29}$Cm. These values result in a maximum theoretical value of $g = 2\pi \cdot 7.84$ MHz. This value is only realized for an atom that is centered on the resonator axis and within a mode antinode. Different measures were taken to ensure that this is the case (see Chapter 3). A measurement of g by means of cavity reflection spectroscopy performed on the coupled atom-cavity system (see Chapter 6.4) yielded a value of $g = 2\pi \cdot 7.62$ MHz, which agrees by up to 3 % with the theory. Table 2.1 summarizes the parameters as they are used in the remainder of this thesis.

2.3. Atom Preparation

Every experimental run is initiated by loading a magneto-optical trap (MOT) that is located 13 mm away from the cavity center along the x-axis. The MOT is loaded directly from the ^{87}Rb background gas that is generated continuously by the Rb dispenser. After a typical loading time of one second, a running-wave dipole trap at a wavelength of 1064 nm is switched on. The trap beam is focused half-way between the center of the atom cloud and the cavity. After switching off the MOT magnetic fields and laser beams, some atoms remain trapped in the optical trap and oscillate between their initial position and the cavity. Following a transfer time of 100 ms, the coaligned standing-wave dipole trap along the x-axis is switched on and the transfer trap is switched off. Some atoms are transferred into individual trapping sites of this one-dimensional lattice within the cavity region.

The loaded atoms can be translated along the x-axis by tilting a glass plate that is mounted at 45° in the retroreflected trapping beam outside of the vacuum chamber. The orientation of this plate defines the optical path and thus the interference condition, resulting in a translation of the entire standing wave pat-

tern. This initial part of the loading procedure and the translation mechanism are described in greater detail in Stefan Nußmann's thesis [61].

The ability to image the atoms is a great advantage [68] as it allows the number of atoms that are loaded in a single attempt to be counted. In earlier experiments, a single atom was loaded by adjusting the size of the MOT, such that on average $\bar{n} \approx 1$ atom would be loaded in a single attempt. The first image exposed after loading the atoms was then used to identify successful loading attempts and interrupt experimental runs in which more than a single atom or no atoms were loaded. Since the trapping potential can be translated along the x-axis, it was sufficient to load a single atom somewhere within the traveling range of the translation mechanism.

The atoms that are loaded in a single shot are independent; thus, the numbers of trapped atoms per loading attempt are expected to follow a Poissonian distribution. An average number of loaded atoms of $\bar{n} = 1$ maximizes the probability of loading a single atom to 37 %, such that a minimum average number of almost three loading attempts were needed. As atom trapping times ($1/e$-time) $> 10\,\mathrm{s}$ were achieved in the experiment, which far outnumber the duration of a single loading attempt, a high single-atom duty cycle of up to 85 % can still be achieved.

This situation changes for two or more atoms. The probability of loading precisely k atoms is maximized for an average loading rate of $\bar{n} = k$. However, the attained maximum value $P_k(k) = k^k/k!\, e^{-k}$ will quickly drop to small values if $k > 1$. Furthermore, although the atom distribution can be translated along the x-axis, interatomic distances cannot be changed. Loading an exact number $k \geq 1$ of atoms with additional boundary conditions on their mutual distances thus complicates probabilistic loading to beyond applicability.

To tackle this problem, an active loading mechanism was implemented. A beam sampler installed in the imaging path enables the launch of a collimated beam from above into the objective. The beam is thus focused down into the plane of the atoms and the angle of incidence onto the objective defines the position of its focal point. An acousto-optical deflector allows to actively change this angle along the x-axis. A sketch of the setup is shown in Fig. 2.1 and further details about the optical setup can be found in reference [62]. By illuminating an atom with resonant light, the random recoils of the scattered photons excite motion in the trap. Since typical trap depths are in the order of 1 mK, the atom is quickly lost from the trap.

Figure 2.3 shows a calibration measurement of the pushout system. By manually translating[3] the red one-dimensional lattice along the z-axis and through automatized shuffling along the x-axis, atoms were scanned over a two-dimensional region. For every position, the probability of an atom surviving a series of

[3] While the atoms can be positioned deterministically along the x-axis using the motorized glass plate, the distribution of trapped atoms can be translated along the cavity axis (z-axis) only by manually translating the whole 1064 nm standing-wave beam.

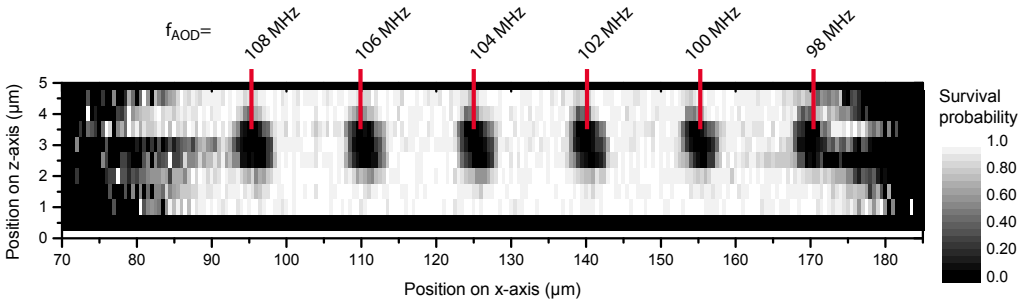

Figure 2.3.: Deterministic removal of individual atoms Spatially resolved measurement of the probability with which an atom survives a series of six pushout pulses at different addressing positions. The frequency of the pushout light was close to the cycling transition of ^{87}Rb and was impinged for 1 ms. The resulting pushout patterns have a full width at half maximum of 4.5 μm.

pushout-attempts was recorded by comparing images taken prior to and after the pushout sequence. In Fig. 2.3, six pulses with durations of 1 ms each were fired consecutively with different frequencies applied to the acousto-optical modulator[4]. The resulting six well discriminable pushout regions have a full width at half maximum of 4.5 μm, in which the survival probability drops to zero. The achieved size of a single pushout region was far above the theoretical optical resolution power of the objective (see Chapter 2.4) but it was sufficient to reliably remove atoms from an initial sparsely filled trap.

The addressing system was planned and installed prior to the implementation of a two-dimensional optical lattice and permits only one-dimensional addressing along the x-axis. In order to hit atoms independent of their (typically small) displacement along the z-axis, the addressing beam was later prolonged along the z-axis by artificially restricting its numerical aperture along this direction.

In contrast to the direct resonant push-out used here, the authors of [69] pursued a strategy based on imprinting AC Stark shifts on optically addressed atoms that would then render these atoms off-resonant to a globally performed microwave Landau-Zener sweep. Another approach to single-atom addressing that can potentially be used for deterministic loading is based on magnetic field gradients [70] that detune all but a single target atom.

In the final system, the experimental control system was programmed to either load a single atom or a pair of atoms with an interatomic distance within a predefined interval of typically $4-15\,\mu$m. The average number of loaded atoms was high enough to ensure that the initial atomic pattern contained a pair of atoms with an accepted interatomic distance. On the other hand, it was set low enough to prevent the average interatomic distance from being comparable

[4]The resulting shift in the deflected light's frequency is compensated through an additional double-pass AOM-track prior to the deflector

to the resolution of the pushout system. The achieved efficiency of atom pair preparation with the parameters used for the experiments in Chapter 6 was approximately 75 %.

2.4. Single-Site-Resolved Imaging

The imaging and rudimentary image evaluation that is used for atom loading (see references [68, 71]) can reliably detect the number of the loaded atoms and their position along the x-axis. For all of the experiments that were conducted with a single atom this was fully sufficient, as the relevant parameters, such as the intensity of the cavity mode and additional beams, varied on spatial scales that far exceeded the achieved resolution.

The experiments that were conducted on atom pairs introduce a new degree a freedom, namely the relative displacement of the two atoms. Since interference effects occur in the two atoms' individual emissions, these experiments are sensitive to changes in the atoms' relative displacements Δ_x, Δ_z, which are small compared to the wavelength of the excitation light $\lambda = 780\,\mathrm{nm}$. The atomic fluorescence light that was used for imaging had the same wavelength; thus, it was impossible to generate a diffraction-limited image of a single atom with a diameter $d < \lambda/2$ on the required scale. Nevertheless, the center of mass of the imaged light can be localized far beyond the diffraction limit. When the point-spread function of the imaging system is symmetric around the origin, the found center-of-mass position is identical to the emitters position. The achievable resolution is then limited only by the achievable signal-to-noise ratio of the images. Measuring the atoms' relative distance is further simplified by the fact that the two-dimensional optical lattice provides only discrete trapping sites with well-known geometry. Therefore, the image evaluation only needs to detect which sites are occupied by the atoms and calculate their separation from the lattice geometry. Neighbouring sites are separated by 512 nm along the x-axis and by 386 nm along the z-axis.

Figure 2.4(a) shows a sketch of mechanical apertures in the imaging beam path that limit the achievable numerical aperture. The objective sits outside of the vacuum chamber, directly above the 8 mm thick, fused silica glass windows. The center of the resonator is 24.9 mm below the objective. The piezo tube, which is used for length stabilization of the cavity, is indicated by the thick black lines. A hole with a diameter of 5.3 mm is machined into its top. The entrance aperture of the objective, with a diameter of 23.1 mm, limits the achievable numerical aperture along the x-axis to $\mathrm{NA}_x = 0.46$ (including the refractive effects of the glass window). Along the z-axis the numerical aperture is limited by the presence of the cavity mirrors. The mirror substrates are milled conically from an outer diameter of 7.74 mm to a minimum diameter of 1.5 mm. In combination with the cavity length of 498 μm, the numerical aperture along the z-axis is thus $\mathrm{NA}_z = 0.32$. The achievable spot size in terms of the full width

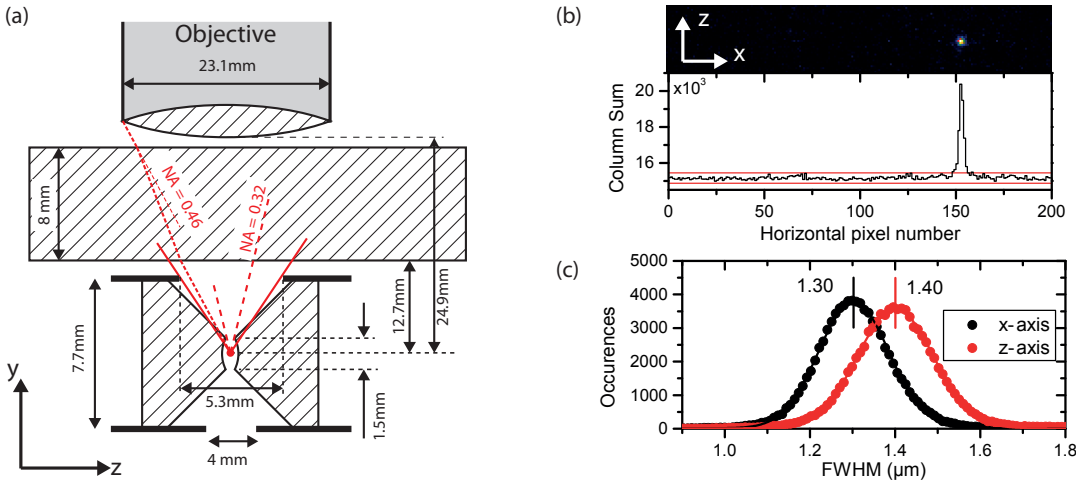

Figure 2.4.: Atom Imaging (a) Geometrical sketch (not to scale) of the imaging beam path and the different apertures that limit the achievable spot size. (b) Typical image of a single atom and column sum of the image. The red bars indicate a $\pm 3\sigma$ region around the average background signal. (c) Histogram of the full widths at half maximum along the x- and z-axis of the fitted Gaussian point-spread functions.

at half maximum of the image intensity is approximately $0.353 \cdot \lambda/\mathrm{NA}$. For the x-axis with its greater numerical aperture, a value of 599 nm is found and the smaller numerical aperture on the z-axis results in a value of 860 nm.

A typical image of a single atom is shown in Fig. 2.4(b) with a plot of column sums. An exposure time of 0.75 s yields a background signal of 425 counts per pixel. The signal collected from a single atom rises to a maximum additional pixel amplitude of 200 counts. The image is truncated to a region of interest that extends 35 pixels along the z-axis. The red lines in the graph indicate a $\pm 3\sigma$ region around the average value of the column sum. The single atom appears as a $> 50\sigma$ signal and can be unambiguously identified. In the first step of the image evaluation, a simple peak detection algorithm identifies well-isolated peaks and two-dimensional Gaussian point-spread functions are then fitted to the discerned peaks.

Figure 2.4(c) shows a histogram of the full-width at half maximum intensity diameters along the x- and z-axis that were found by evaluating 84,000 images of single atoms. The data is well described by Gaussian distributions and a mean diameter of 1.3 μm (1.4 μm) along the x-axis (z-axis) was found. In accordance with the qualitative expectation, the atom images appear to be elongated along the z-axis. Quantitatively, the images deviate strongly from the theoretical expectation; the observed diameters were almost double the minimum possible value and the ellipticity was smaller than expected. This discrepancy was likely a consequence of the atoms being imperfectly localized in the focal plane. The mechanical mount of the objective does not permit reproducible translations of

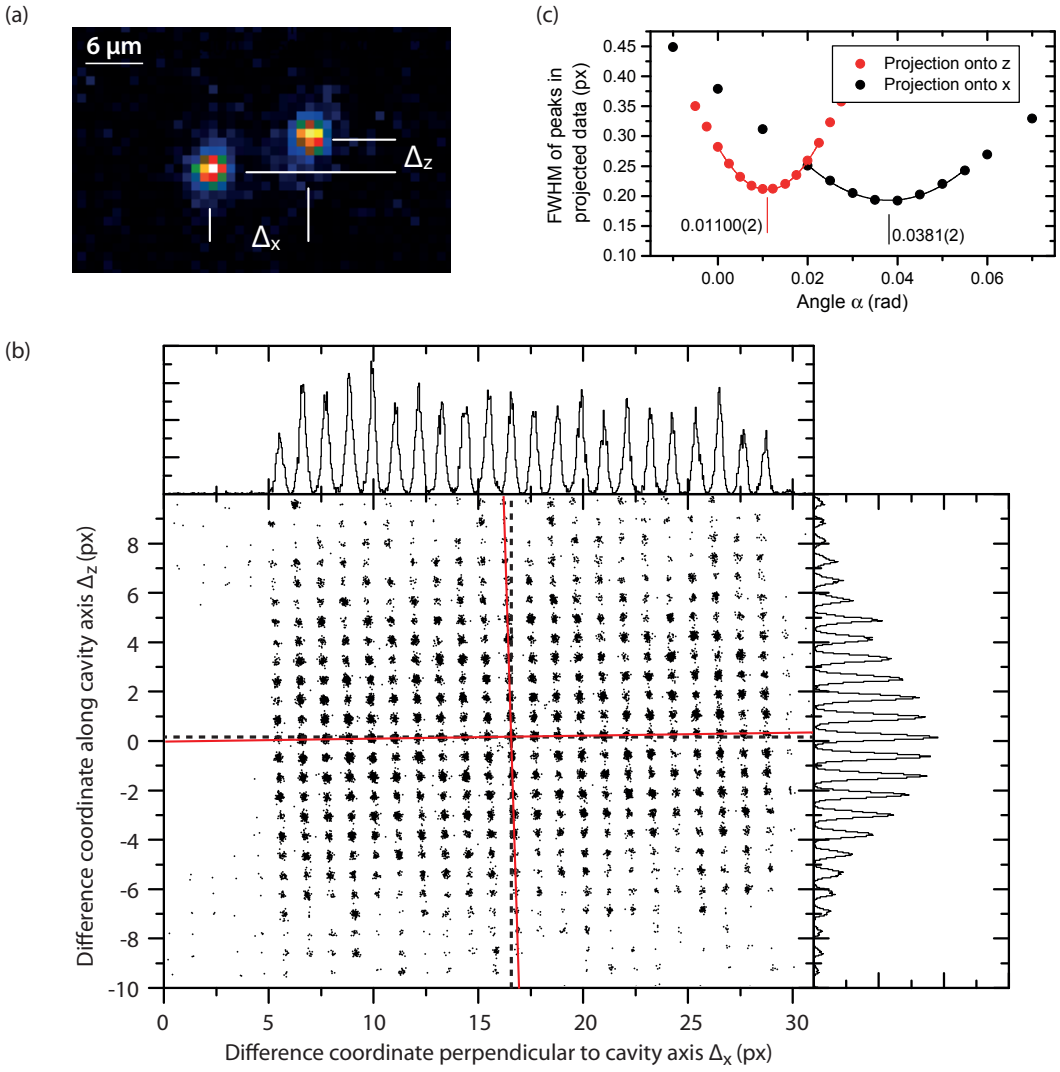

Figure 2.5.: Single-site-resolved image evaluation (a) Single fluorescence image showing two well-separated atoms that are displaced along the x- and z-axis. (b) Difference coordinates of the origins of Gaussian point-spread functions that were fitted to 45.000 atom pairs together with projections of the data onto the coordinate axes. (c) The widths of the discrete peaks found in the projections onto the x- and z- axis as a function of a global rotation about the y-axis by angle α.

the objective along the y-axis on the order of only a few micrometers. Also, the atoms are only weakly confined along the y-axis (see Chapter 3); even at the low temperatures realized in the experiments, they can travel by distances that are comparable to the focal depth of the objective.

In experimental setups with more demanding imaging requirements, these problems are addressed by populating only a single layer in a three-dimensional lattice and recording an entire stack of images while translating the objective

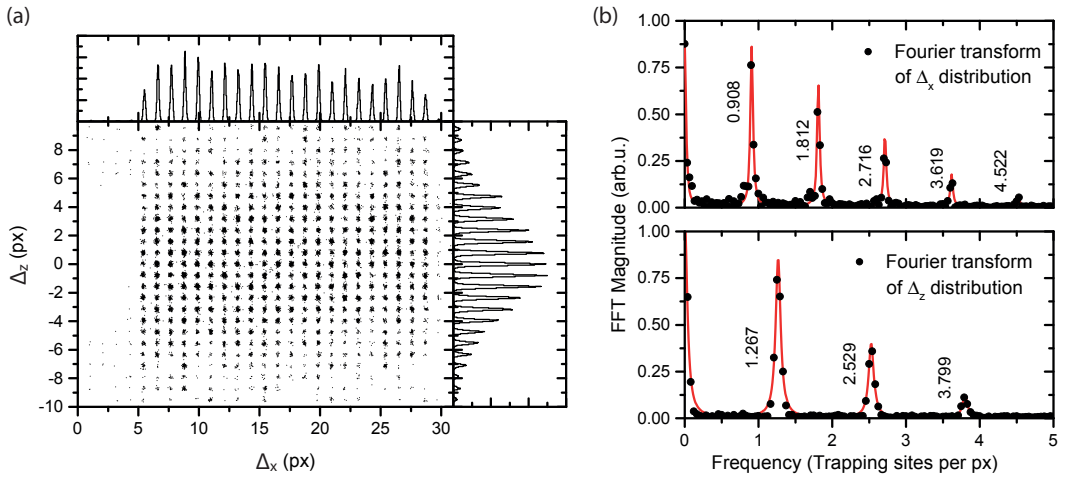

Figure 2.6.: Evaluation of the lattice geometry (a) Difference coordinates of atom pairs after application of the geometric transformation 2.4. (b) Fourier transformation of the projection of the data onto the coordinate axes, which are shown at the edges of (a). The red lines are multiple Lorentzian fits.

on an automatic piezo stage [72]. The focal position can then be found from the image stack in each individual experiment. Because the achieved imaging resolution was sufficient, no such measures were implemented in the apparatus that was used in the experiments described in this thesis.

Figure 2.5(a) shows an example image of a pair of atoms that are displaced along both axes of the two-dimensional optical lattice. A histogram of binned single-atom coordinates shows a periodic structure along both axes. This structure disappears for long integration times, as the relative alignment of lattice, objective, and camera slowly changes. However, the geometry of the lattice can as well be observed in differential coordinates of atom pairs instead of absolute single-atom coordinates [72, 73]. Figure 2.5(b) shows the two-dimensional difference coordinates of 45,000 atom pairs with the projections of the data onto the x- and z-axis. The white space between $0 < \Delta_x < 5\,\mathrm{px}$ stems from the data evaluation software that discards loading attempts that result in two atoms that are so narrow that the individual atoms' images start to overlap. Well separated accumulation points that form a rectangular lattice are easily recognized. The axes along which the accumulation points are aligned (red lines) appear to be tilted with respect to the coordinate axes (black dashed lines). Figure 2.5(c) shows the full width at half maximum of the discrete peaks observed in the projections onto the two axes as a function of a global rotation α that is applied to the data. Two clear minima are observed at $\alpha_x = 0.01100(2)$ for the projection onto the x-axis, and $\alpha_z = 0.0381(2)$ for the projection onto the z-axis. The fact that the two minima are found at different values of α indicates that the lattice is not perfectly orthogonal. The 1064 nm standing wave trap

along the x-axis intersects the intracavity trap at an angle that deviates from orthogonality by $\beta = \alpha_z - \alpha_x = 27.0(3) \cdot 10^{-3}\,\mathrm{rad}$. As a consequence of this non-orthogonality, motional coupling between the atomic motion along the x- and z-axes is observed (see Chapter 4.4).

To account for the non-orthogonality and a global rotation α_x of the camera's coordinate frame with respect to the lattice, the following transformation was applied to the data:

$$\begin{pmatrix} x' \\ z' \end{pmatrix} = \begin{pmatrix} \cos(\beta) & -\sin(\beta) \\ 0 & 1 \end{pmatrix} \begin{pmatrix} \cos(\alpha_x) & \sin(\alpha_x) \\ -\sin(\alpha_x) & \cos(\alpha_x) \end{pmatrix} \begin{pmatrix} x \\ z \end{pmatrix} \tag{2.4}$$

Figure 2.6 shows the same data as in Fig. 2.5 after the application of this transformation. The cluster points now clearly lie on an orthogonal lattice and the width of the peaks in both projections are minimized.

The Fourier transform of the two distributions is shown in part (b) of the figure. A periodicity of 0.906 trapping sites per image pixel was found for the x-axis and a value of 1.267 trapping sites per image pixel for the z-axis. The ratio of the two deviates by 1.5 % from the theoretical value given by the two wavelengths of the traps (772.37 nm/1064 nm). Possible explanations include the objective's optical axis not being orthogonal to the plane of the atoms or a geometrical distortion, as would be expected in the peripheral areas of the objective's field of view [62]. A pixel on the camera corresponds to 490 nm in real space (calculated with the values found along the z-axis).

2.5. Detection and Manipulation of the Internal State

Interaction of the electronic shell's angular momentum J with the nuclear spin I splits the $5S_{1/2}$ ground state of alkali atoms into two manifolds with different hyperfine spins F=J+I. In the case of ^{87}Rb with a nuclear spin I=$^3/_2$, two tuples of states with hyperfine spins F=1 and F=2 are formed that enclose an energy difference of 6.835 GHz [74]. Electronic dipole transitions between these two states are forbidden and the radiative lifetime of the energetically higher F=2 state can be regarded as infinite for all of the experiments that are described in this thesis. Interaction with external light or microwave fields can cause changes in the population of these states. By observing these changes, the electronic structure of trapped atoms (see Chapter 3.2.2), the geometry of the trapping potential (see Chapter 4), and individual mechanical eigenstates (see Chapter 5) can be probed.

2.5.1. Cavity-Assisted Hyperfine-State Detection

The natural linewidth of electronic transitions from the ground states to the electronically excited $5P$ states of ^{87}Rb is 6 MHz. The two hyperfine ground states can thus be spectroscopically resolved, as their splitting outnumbers the transition linewidth by three orders of magnitude. Different schemes for hyperfine state detection were published recently. Two different types are distinguishable based on whether the employed physical mechanism is based on observing fluorescence from the atom [75] or probing the transmission of a coupled atom-cavity system [76]. A comparison of both schemes performed on the apparatus described in this thesis can be found in [77]. In the following paragraph, a fluorescence-based scheme is described:

The population of one ground state $|1\rangle$ can be probed by impinging a laser with a frequency that resonantly couples this state to some excited state $|e\rangle$ for probing time T, and observing light that is scattered out of the laser's propagation direction. When picking up this light with a sensitive detector, a rate Γ_1 of detected photons is registered. The transition from the second ground state $|0\rangle$ is far detuned, such that excitation is highly unlikely and no fluorescence is detected. Ideally, the average number of detected photons $T \cdot \Gamma_1 \gg 1$ is high enough to clearly separate the number distribution of detected photons for the atom in state $|1\rangle$ from the distribution recorded when the atom is in state $|0\rangle$[5]. In this case, an unambiguous measurement result can be obtained in a single shot.

In an experimental implementation, the radiative decay that leads to the signal rate Γ_1 typically competes with different decay channels that bring the atom to the dark hyperfine state with rate Γ_0. A single decay on such a transition immediately terminates the generation of the signal, as the atom is removed from the interaction with the light once it is in state $|0\rangle$.

Assuming signal photons are uncorrelated, the expected photon number distribution $P_n(\Gamma_1, \Gamma_0, T)$ for an atom in state $|1\rangle$, as a function of the two rates and the probing duration, can be calculated:

$$\begin{aligned} P_n(\Gamma_1,\Gamma_0,T) &= e^{-\Gamma_0 T}\frac{(\Gamma_1 T)^n}{n!}e^{-\Gamma_1 T} + \int_0^T \Gamma_0 e^{-\Gamma_0 t}\frac{(\Gamma_1 t)^n}{n!}e^{-\Gamma_1 t}dt \\ &= e^{-\Gamma_0 T}\frac{(\Gamma_1 T)^n}{n!}e^{-\Gamma_1 T} + \\ &\quad \frac{\Gamma_0 T(\Gamma_1 T)^n}{((\Gamma_0+\Gamma_1)T)^{n+1}}\frac{\Gamma(1+n)-\Gamma(1+n,(\Gamma_0+\Gamma_1)T)}{n!} \end{aligned}$$

[5] In a typical experimental implementation of the described fluorescence based state-detection scheme, the photon-number distribution of the dark state will be zero photons with unity probability. Only unlikely far-off-resonant excitation and technical problems, such as detector dark count can result in a detected signal although the atom was in the dark state $|0\rangle$

Here, $\Gamma(a)(\Gamma(a,z))$ is the (incomplete) Gamma function. For long probing times the probability of not observing a single photon approaches $P_0(T \to \infty) = \Gamma_0/(\Gamma_0 + \Gamma_1)$. This defines an upper bound of discrimination efficiency. It is thus beneficial to interrogate the system on a cycling transition that by definition cannot decay to other states. A residual Γ_0 can still be caused by off-resonant excitation of other excited states or perturbations of the electronically excited states by the presence of the dipole light that opens decay channels to other states (see Chapter 3.2.2).

Achieving a great Γ_1 in free-space is hampered by the technological challenge of collecting atomic fluorescence light covering a large solid angle. An optical resonator surrounding the atom opens up a way to solve this problem by enhancing the coupling of the atom to a single light mode, which can be efficiently observed. Cavity-assisted hyperfine-state detection was already demonstrated in the described setup [77] with a discrimination efficiency of $> 99\,\%$ after a probing time of $T = 85\,\mu$s. The atoms in this experiment were trapped in a one-dimensional lattice along the x-axis only. The confinement along the z-axis originated solely from the Gaussian envelope of the standing-wave beam and permitted mechanical excursions exceeding a full period of the cavity mode. The successful implementation of a two-dimensional trapping geometry that confines the atoms constantly to antinodes of the cavity mode (see Chapter 3) makes it possible to achieve comparable discrimination efficiencies within a shorter probing duration.

The state-detection scheme is sketched in Fig. 2.7(a), and Fig. 2.7(b) shows experimental data that was collected with the $|1\rangle \leftrightarrow |e\rangle$ transition being the cycling transition on the D_2-line. The photon number distributions were recorded with a probing time of $15\,\mu$s after initializing the atom (see Chapter 2.5.2) in either F=1 or F=2 and are well separated. A discrimination threshold of a single detected photon allows a discrimination efficiency of $> 98\,\%$. The data is well reproduced by assuming Γ_1=370 kHz and Γ_0=1 kHz as shown in Fig. 2.7(c). The large ratio Γ_1/Γ_0 results in a near Poissonian distribution. In contrast, Fig. 2.7(d) shows the result of an attempt to perform state detection with $|1\rangle = |5S_{1/2}, \mathrm{F}{=}1\rangle$ and $|e\rangle = |5P_{3/2}, \mathrm{F}{=}0\rangle$. In this case, a larger Γ_0 is expected as the detuning to other excited states is smaller. Furthermore, a $\Delta F{=}-1$ transition necessarily has two dark Zeeman states for every given polarization of the probing light. Decay to these contributes to Γ_0. While the average number of detected photons after a prolonged interrogation time of $T = 75\,\mu$s is similar to case shown in (b), the number distribution is different with a high residual probability of detecting zero photons. Panel (e) shows a fit of the theory to the data that finds Γ_1=100 kHz and Γ_0=13 kHz. The theoretical limit of $P_0 = \Gamma_0/(\Gamma_1 + \Gamma_0) = 0.115$ is already reached at the given probing duration and the achieved discrimination efficiency is for these parameters physically limited rather than by insufficient probing duration.

Motivated by the possibility of implementing a heralding signal for the hyperfine-state transfer in a quantum-memory protocol [78], different detunings and

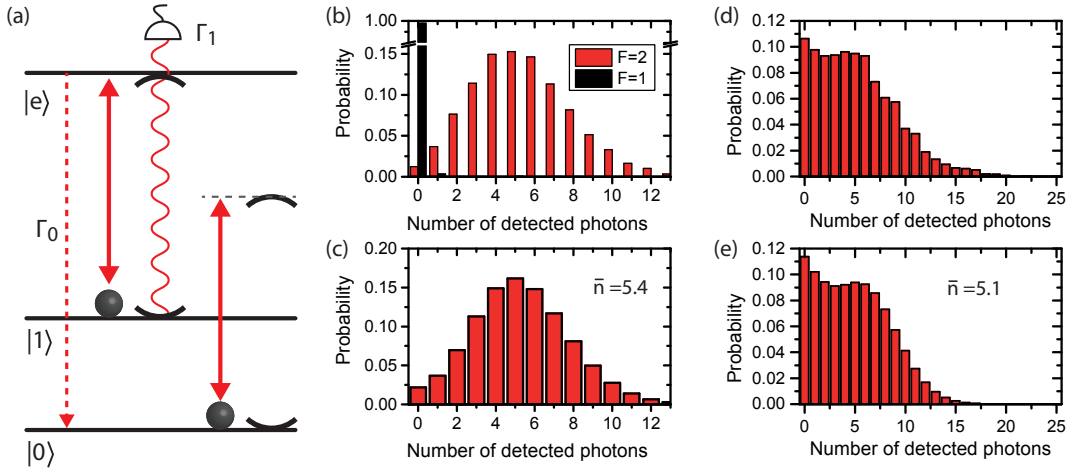

Figure 2.7.: Hyperfine state detection (a) Sketch of the scheme for cavity-assisted hyperfine-state detection. (b) Measured photon number distribution for a probing time of $T = 15\,\mu$s in the case of $|1\rangle = |5S_{1/2}, F = 2\rangle$ and $|e\rangle = |5P_{3/2}, \mathrm{F}{=}3\rangle$. The red (black) bars show data that was measured after intializing the atom in the F=2 (F=1) ground state. (c) Theory values calculated with $\Gamma_1{=}370\,$kHz and $\Gamma_0{=}1\,$kHz. The atom in this case is lost to a dark state only after an average of 370 signal photons has been detected. (d) Result of an attempt to perform state detection with $|1\rangle = |5S_{1/2}, \mathrm{F}{=}1\rangle$ and $|e\rangle = |5P_{3/2}, \mathrm{F}{=}0\rangle$. (e) Theory values calculated for $\Gamma_1{=}100\,$kHz and $\Gamma_0{=}13\,$kHz.

polarization schemes for state detection with the $F = 1$ ground state as the light state were tested, including schemes with changing polarization of the excitation light. No scheme has been found that resulted in significantly better performance than the data presented. Still, with regions of the large parameter space left undiscovered, this can remain an interesting field of research in the future.

The short discussion of cavity-assisted hyperfine-state detection provided in this chapter spares some complications that are induced by the heating of the atom during probing and the presence of multiple Zeeman states in the hyperfine ground states. Furthermore, the detuning of the resonator, and the excitation laser's polarization and detuning provide experimental degrees of freedom to influence the performance of the scheme. As cavity-enhanced state detection is merely a tool for the experiments discussed in this thesis rather than a field of research, no thorough characterization of these dependencies was performed. For all experiments that make use of the described technique, parameter sets that allow for high discrimination efficiencies (above 95 %) could be found experimentally.

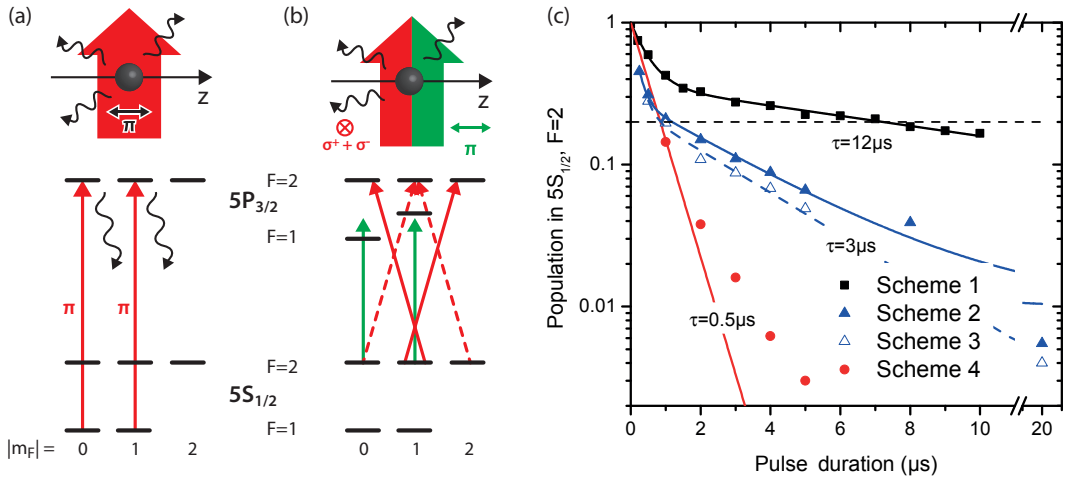

Figure 2.8.: Optical pumping of the hyperfine ground state (a) Optical pumping scheme for preparation of the atom in $5S_{1/2}$, F=2. (b) Optical pumping scheme for preparation of the atom in $5S_{1/2}$, F=1. (c) Residual population in the F=2 ground state when attempting to pump to F=1 as a function of optical pumping duration for different schemes: (1) A single, linearly polarized field resonant with the $2 \rightarrow 2'$ transition. (2) The same resonant field driving the $2 \rightarrow 2'$ transition together with a π-polarized field resonant that drives transitions from the F=2 ground state to the F=1,$m_F = \pm 1$ excited states. (3) The same as the aforementioned scheme but with twice the intensity of the $2 \rightarrow 2'$ field. (4) Same as before but with the frequency of the $2 \rightarrow 1'$-field reduced by 30 MHz to make it resonant with the excited m_F=0 state. The lines are fitted double exponential decays (see text).

2.5.2. Optical Pumping of Hyperfine Ground States

Complementary to the faithful detection, the initialization of the hyperfine ground state is of equally high importance. After optical molasses cooling that typically precedes experiments described in this thesis, the atom is left in a statistical mixture of both hyperfine states and their Zeeman sub-states. Preparation is carried out by impinging light fields that selectively drive transitions from one of the two hyperfine states to an electronically excited state that has a finite decay probability to the other hyperfine ground state. Atomic population will then be completely transferred to the other hyperfine state following a long enough pumping duration.

Throughout the experiments that are described in this thesis, different pumping schemes were employed based on the availability of frequencies and polarizations of laser fields. This chapter provides a short overview over the problems that typically arise and the timescales that have been achieved.

Figure 2.8(a) shows the optical pumping scheme for initialization of the atom in the $|5S_{1/2}, \mathrm{F}{=}2\rangle$ ground state. A single, arbitrarily polarized laser field that resonantly excites the atom from F=1 to the $|5P_{3/2}, \mathrm{F}{=}2\rangle$ state in this case suf-

fices. The excited state can decay to the F=2 ground state and the ΔF=1 excitation does not have any dark states independent of the excitation laser's polarization. For the sake of simplicity, the polarization in Fig. 2.8(a) is linear and oriented along the quantization axis, such that it drives π-polarized transitions in the atomic coordinate frame. The lifetime of the excited state is 26 ns and decay from the excited F=2 states branches in equal fractions into both hyperfine ground states. Saturation of the transition is therefore expected to lead to a maximum possible population transfer rate of $(108\,\mathrm{ns})^{-1}$. In accordance with theory, pumping durations on the order of 1 μs were found to be sufficient for emptying the F=1 ground state to a residual population $< 1\,\%$. The choice of an excitation field that is π-polarized but resonant with the transition to the excited F=1 rather than the F=2 state will render the F=1,m$_F$=0 state dark.

In combination with the subsequently discussed repumping from the F=2 ground state, this can be used to pump atomic population into one of the two hyperfine manifolds, and to a certain Zeeman state within one hyperfine manifold [58]. The initialization of the atom in $|5S_{1/2}, \mathrm{F}{=}1, m_F{=}0\rangle$ by pumping with a π-polarized field on the F=1$\leftrightarrow$F'=1 transition was used for the experiments reported in Chapters 4.3 and 5.

In the opposite case of transferring atomic population from the F=2 to the F=1 hyperfine ground state, complications arise from the existence of uncoupled dark states. Figure 2.8(b) shows one of the coupling schemes that was used in many experiments throughout this thesis. The red arrows indicate couplings caused by a light field that is resonant with the transition to the excited $|5P_{3/2}, \mathrm{F}{=}2\rangle$ state. The polarization of this field is linear and oriented perpendicular to the quantization axis (z-axis); in the atomic coordinate frame, it therefore drives σ^+ and σ^- transitions with a well-defined phase relation. The complex coupling pattern conceals a dark state, which is equivalent to the F=2,m_F=0 state in an alternative atomic coordinate frame that is aligned with the light's polarization. In the coordinate frame of Fig. 2.8 this state appears as a superposition state of $m_F \in \{-2, 0, 2\}$ states. Thus, only four out of five Zeeman states can be excited. Accumulation of population in the dark state, due to decay from the excited state during probing, further limits the achievable efficiency to over 20 %. Pumping of the population in the dark state can only be caused by off-resonant excitation to other excited states or Larmor precession out of the dark state due to an external magnetic field. Both mechanisms are slow compared to the resonant excitation of the coupled states.

Figure 2.8(c) shows the dynamics of the pumping process by plotting the residual population $P_2(t)$ in the F=2 state versus the duration of the pumping pulse t. The data was obtained by emptying the F=1 ground state as described above, attempting optical pumping back into F=1 for a time t and finally testing for population in F=2 through cavity-assisted hyperfine-state detection (see Chapter 2.5.1).

The discussed scheme of a single light field that is resonant with the $2 \rightarrow 2'$ transition is shown as black squares. The black line is a double exponential fit

to the data $P_2(t) = A\exp(-t/\tau_1) + (1-A)\exp(-t/\tau_2)$. A quick initial decay of $A = 64\,\%$ of the atomic population with a decay constant of $\tau_1 = 490\,\text{ns}$ is followed by drastically slower decay of the remaining population with a decay constant of $\tau_2 = 12\,\mu\text{s}$.

Additional light fields that couple the dark state to other excited states can be used to increase the population transfer rate. The solid blue triangles (Scheme 2) in Fig. 2.8 show $P_2(t)$ after the addition of a linearly polarized field that couples the F=2 ground state to the F=1 excited state. This field is shown as green arrows in Fig. 2.8(b). As detailed in Chapter 3.2.2, a strong tensor light shift caused by the presence of the 1064 nm dipole trap lifts the degeneracy of the $m_F = 0$ and $m_F = \pm 1$ states in the excited F=1 manifold. Here, the additional laser was tuned such that it could resonantly excite the $m_F = \pm 1$ states. The hollow blue triangles (Scheme 3) show data that was collected for the same coupling scheme with twice the intensity of the light field coupling the $2 \rightarrow 2'$ transition. Both datasets that were obtained with an additional field show identical behaviour in that a large part of the initial population decays rapidly.

While the introduction of the additional light field increased the decay constant of the remaining population by a factor of four, the whole process still appears to be limited by an insufficient transfer rate out of the dark state. The red dots (Scheme 4) show data that was collected with the frequency of the additional field reduced by 30 MHz. The trap depth ($U = h \cdot 37\,\text{MHz} = k_B \cdot 1.7\,\text{mK}$), used in these experiments, renders the additional laser field at this reduced frequency resonant with the excited F=1,m_F=0 state (see chapter 3). Resonant excitation of the F=2,m_F=0 ground state is expected to lead to a significantly higher transfer rate out of the dark state. In fact, the level of $< 1\,\%$ residual population in the F=2 ground state is reached after $3\,\mu$s of optical pumping in this scheme. While this value is still a factor of six above the theoretical limit of 500 ns, it is sufficient for all of the experiments reported in this thesis.

Throughout the experiments covered in this thesis, different schemes for optical pumping were used. Details of the implementation may differ, but the underlying principles discussed in this chapter remain valid. It was easy to faithfully empty the F=1 ground state with a single light field. In order to empty the F=2 ground state, different combinations of additional fields with the aim of exciting the otherwise dark state were used.

2.6. Stimulated Raman Transitions

The term *Raman scattering* subsumes many different light scattering mechanisms in atoms, molecules, and solid-state systems that have in common that they are inelastic and the energy of emitted radiation is different from the energy of the exciting radiation. In many Raman spectroscopy experiments, only one excitation laser is used and the spectral properties of the emitted light are

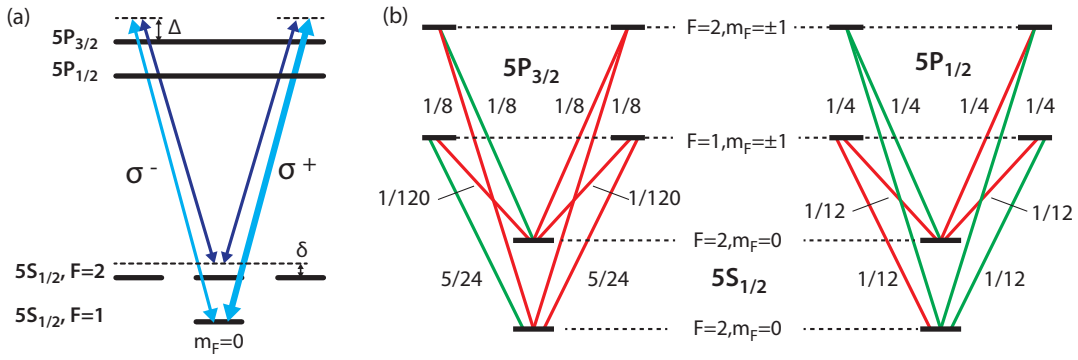

Figure 2.9.: Stimulated Raman transitions (a) Transitions between the atom's internal states coupled by the trapping light (light blue) and the additional running-wave Raman laser (dark blue). The elliptical polarization of the intracavity trap causes an imbalance in the σ^+ vs σ^- driving strength of the trap. (b) Clebsch-Gordan coefficients (squared) between relevant states on the D_1 and D_2 lines that define the transition matrix elements. The color denotes the sign of the coefficient (green is negative, red is positive).

analyzed in order to extract properties of the scatterer's energy eigenvalues. If the scatterer's internal structure is well known, two light fields that are impinged simultaneously can drive stimulated Raman transitions between states in order to perform controlled manipulations rather than spectroscopy. To this end, the two fields must enclose a frequency difference that is compatible to the energy difference of the states.

Stimulated Raman couplings are an established tool in ultracold atom experiments and their theory is well understood and documented [79, 80]. In experiments with individual atoms, these couplings are often used to perform coherent rotations between pairs of states in the atom's ground-state manifold [81,82] and for cooling to the motional ground state of the trapping potential [81, 83–86]. In the experiments reported in this thesis, Raman transitions are used as a tool to characterize eigenmotions of the trapping potential (Chapters 4.2 and 4.4), for ground-state cooling of a single atom (Chapter 4.3) and for the controlled preparation of mechanically excited states (Chapter 5.3.2).

In the experimental apparatus, Raman transitions can be driven using the intracavity dipole trapping light in combination with light from a laser that is phase-locked to the trapping light. The light from this laser is shone onto the atom in a running-wave configuration along the x-axis. Figure 2.10(a) shows the transitions that are driven by the two fields when the atom is initialized in the $|5S_{1/2}, \mathrm{F}{=}1, m_F{=}0\rangle$ state. The light blue arrows denote transitions that are driven by the intracavity trap. For the majority of experiments that are described in this thesis, the polarization of this light was elliptical (see Chapter 5.2). In the atomic coordinate frame, the σ^+-polarized transition is therefore driven with a greater Rabi frequency than the σ^--polarized transition. The

running wave beam on the x-axis is tuned by the exact hyperfine splitting of 6.834682 GHz below the intracavity trapping light and is polarized linearly with its electric field aligned perpendicular to the cavity axis. It thus drives σ^+ and σ^- transitions with equal strength (and well-defined phase relation). The two fields have a wavelength of 772 nm and thus a so-called one-photon detuning $\Delta \gg \Gamma$ that exceeds the radiative lifetime of the excited states $1/\Gamma = 25\,\mathrm{ns}$ by orders of magnitude. A total of eight possible transition paths is formed by coupling the two ground states to the excited $m_F = \pm 1$ states in the $F \in \{1, 2\}$ manifolds of the $5P_{1/2}$ and $5P_{3/2}$ states. These paths are shown in Fig. 2.9(b).

It was shown theoretically (e.g. [80]) that in the case of $\Delta \gg \Gamma$ and vanishing two-photon detuning $\delta = 0$, every single transition path causes an effective Rabi frequency:

$$\Omega_{\mathrm{eff}} = \frac{\Omega_1 \Omega_2}{2\Delta}, \tag{2.5}$$

where Ω_1 and Ω_2 are the Rabi frequencies of the two coupling fields and Δ is the one-photon detuning with respect to the considered excited state. The effective Rabi frequency Ω_{eff} causes coherent Rabi flopping between the two ground states with a negligible excitation probability of the excited state. The two Ωs are given by the transition dipole matrix element of the respective transitions for all of the eight mentioned paths. For identically oriented, linear polarization of the two fields (i.e., the same phase between the σ^+ and σ^- components for both fields), all partial transition amplitudes interfere destructively. The indicated $\Delta m_F = 0$ transfer is therefore not possible.

The situation in the described apparatus deviates from this situation in two ways, both of which are related to the polarization of the intracavity trap. The principal axis of the electric field's polarization ellipse is oriented almost perfectly along the x-axis. Therefore, even if the trap's polarization was linear, the phases between the two circular components' couplings would be opposite. In combination with the transition matrix elements' phases, all partial couplings would interfere constructively and the transfer would be possible. The elliptical polarization of the trap leads to an additional breaking of the symmetry, in that it causes the σ^+ components to be stronger than the σ^- components. Perfect destructive interference of the transition paths in this situation is impossible, regardless of the orientation of the polarization.

The described relative orientation of the two polarizations and the resulting $\Delta m_F = 0$ transfer was used for all of the experiments discussed in this thesis. By rotating the linear polarization of the coupling laser towards the cavity axis, π-polarized couplings are generated and a $\Delta m_F = \pm 1$ transfer becomes possible (while this as well was observed experimentally, it is not relevant to the experiments discussed in this thesis).

Effects of coherent interference of different transition pathways are not only present in the atom's internal spin-degree of freedom. The effective Rabi frequency given by equation 2.5 can always be chosen to be real without loss of

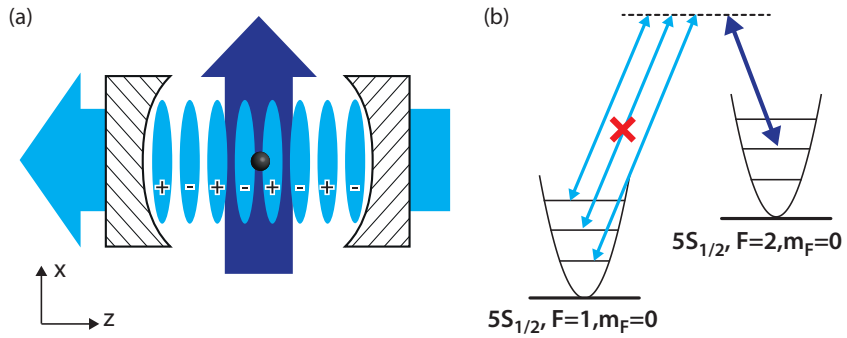

Figure 2.10.: Raman geometry and mechanical selection rules (a) The repulsive intracavity trap (light blue), which confines the atom (black sphere) to light nodes is used as one of the two Raman fields. The phase of the trapping light's electric field alternates in neighbouring field antinodes. The second field (dark blue) is shone in a running-wave configuration onto the atom along the x-axis. (b) Due to the symmetry of the coupling and the motional wave functions, combined spin-mechanical transitions are only possible between mechanical states of opposite parity.

generality in case of a pointlike atom by application of a suitable gauge transformation. But in the case of a coherently delocalized atom, relative phases appear between the couplings at different positions. These couplings must be added before their net effect on the atom is calculated, analogous to the interference of different internal pathways discussed above. A related peculiarity of the experimental setup is the geometry of the Raman coupling shown in more detail in Fig. 2.10(a). The trapping light that confines the atoms to light nodes serves as one of the Raman beams. As a consequence, the effective Raman coupling (equation 2.5) that is proportional to the trapping light's electric field rather than its intensity will be spatially antisymmetric with respect to inversion of the z-axis. The mechanical wavefunctions of the atom are localized around a node of the blue-detuned trap's standing wave and have well-defined spatial parity. Mechanical states of identical parity will be left uncoupled by the Raman lasers, as the corresponding spatial integral will always be antisymmetric and will evaluate to zero.

This argument hinges on the fact that the intracavity trap is blue detuned and thus creates a repulsive mechanical potential. For red-detuned dipole traps, the opposite argument holds. The atoms are confined to intensity maxima, the electric field, and correspondingly the Raman coupling, will be symmetric around the potential's minimum. In this scheme, only mechanical states of identical parity are coupled. For a harmonic trap with eigenstates $|n\rangle$, the parity is given by $(-1)^n$ and the resulting mechanical selection rules for motional states along the z-axis[6] can be summarized as:

[6]With the same argument, it becomes clear that the motional states along the x- and y-axis cannot be addressed at all through this scheme. Exceptions are higher-order transitions

$$\begin{aligned} \Delta n &= \pm 1, \pm 3, \pm 5 \ldots \text{ for a blue-detuned dipole trap} \\ \Delta n &= 0, \pm 2, \pm 4 \ldots \text{ for a red-detuned dipole trap} \end{aligned}$$

Figure 2.10(c) summarizes the different transitions of an atom in a given mechanical state of the $|5S_{1/2}, \mathrm{F}{=}2, m_F{=}0\rangle$ spin state. The transition on two-photon resonance ($\delta = 0$) is forbidden due to the discussed parity-effects. Transitions to higher and lower mechanical states are possible. In the figure, only the $\Delta n = \pm 1$-transitions are shown; while the transition-matrix elements for higher order transitions ($\Delta n = \pm 3, \pm 5..$) do not vanish, they will generally be small.

Stimulated Raman transitions were used in different ways in the experiments that are described subsequently and much information about the motional states could be extracted from experimentally recorded Raman spectra (see chapters 4.3 and 4.4).

[86] and the case in which the trapping potentials eigenmotions are not aligned with the x- and z-axis (see chapter 4.4).

3. AC Stark Shifts and Hyperfine Breakdown

3.1. Introduction

The AC Stark effect describes a shift of atomic energy eigenstates that is caused by interaction with far-off resonant light. The shift is proportional to the intensity of the light and for an atom in a given internal state, a force along the gradient of the light's intensity will arise. Through a suitable choice of wavelength, intensity, and geometry of the light, optical dipole traps (ODT) can be generated that confine atoms in free space using only laser light [87]. Since their first demonstration [88] in 1986, optical dipole traps have grown to become a well-established tool in experimental quantum optics. Because the geometry of the created potential is defined only by the light's spatial intensity pattern, all of the tools of conventional wave optics can be used to create almost arbitrary potential landscapes [89].

The experiments reported in this thesis make use of dipole traps in order to hold single neutral atoms at well-known positions and in close vicinity to the dielectric surface of a Fabry-Perot cavity. In order to achieve a tight spatial confinement of the atom, deep traps are used. Along the x-axis, the atoms are held by a standing wave trap with a typical potential depth of $U_0 = h \cdot 35\,\mathrm{MHz} = k_B \cdot 1.7\,\mathrm{mK}$. This corresponds to a light intensity of $1\,\mathrm{MW/cm^2}$ in the trap. Because the light not only shifts the ground states, but as well perturbs electronically excited states of the atom, transition frequencies of the atom are changed by the presence of the trap. In order to resonantly excite the atom, it is therefore crucial to have a quantitative understanding of the changes inflicted by the presence of the trapping light onto the internal energy eigenstates of the atom.

While doing spectroscopy on the electronically excited $5P_{3/2}$ state of ^{87}Rb, it was found that the tensor polarizability of this state can lead to a breakdown of atomic hyperfine structure. This is similar to the transition from the Zeeman into the Paschen-Back regime in the case of an applied magnetic field. Hyperfine breakdown must be taken into account in order to predict AC Stark shifts quantitatively. Besides changes in the energy eigenvalues, also energy eigenstates are changed. The latter has consequences for optical pumping schemes that rely on dipole selection rules for hyperfine spin states, which are not energy eigenstates any more in a deep dipole trap. A full account of the AC Stark shift including

hyperfine breakdown is provided in the theory section of this chapter. In the experimental section, a sequence to carry out spectroscopy on a single trapped atom is described and data are presented. An AC Stark shift that is quadratic in the applied intensity and violation of a hyperfine dipole selection rule are observed as unambiguous signs of hyperfine breakdown.

3.2. Theory

The classical Stark effect describes a shift of an atomic energy eigenstate $|i\rangle$ that is caused by an external electric field $\vec{E}$ [90]. Due to the spatial symmetry of an atom's nuclear electrostatic potential, all electronic energy eigenfunctions have well-defined parity: $\Psi_i(\vec{r}) = \pm\Psi_i(-\vec{r})$. In the absence of degeneracy among the energy eigenstates, the expectation value of the perturbation $\langle\delta E\rangle = \langle i|\vec{E}\cdot e\vec{r}|i\rangle$ caused by the field is therefore zero. A linear Stark effect is thus only present in the case of degenerate energy eigenstates.

In second order perturbation theory, coupling to states of opposite parity can give rise to a quadratic Stark effect $\Delta E^{(2)} = \sum_f \frac{|\langle i|\vec{E}\cdot e\vec{r}|f\rangle|^2}{E_i - E_f}$, where the sum runs over all of the remaining states $|f\rangle$. The resulting shift can be mathematically phrased by attributing a polarizability α to each state, which quantifies an atomic dipole $\vec{p} = \alpha\vec{E}$ that is induced by an applied electric field. The interaction of this induced dipole with the inducing electric field leads to a potential energy $\Delta E = -\frac{1}{2}\alpha|E|^2$ that is quadratic in the applied electric field. The quantity $\alpha = -2\sum_f \frac{|\langle i|\hat{e_z}e|f\rangle|^2}{E_i - E_j}$ is called the static electric polarizability. When the applied electric field is oscillating rapidly compared to other dynamic processes, its effect can be averaged over one optical period and the time-averaged energy shift due to the quadratic Stark shift will be $\Delta E = -\frac{1}{4}\alpha E^2$. This energy shift is typically referred to as a light shift or AC Stark shift.

For atoms with finite angular momentum, α will be dependent on the laser polarization. Furthermore, optical resonances make $\alpha(\omega)$ dependent on the frequency ω of the applied laser. A full account of the topic can be found in [91, 92] and only the most important results are reproduced here.

For states $|n\,J\,m_J\rangle$ where n is the principal quantum number, J is the total angular momentum and m_J is its projection onto the quantization axis (z-axis), the dynamic polarizability is expressed in terms of a scalar $\alpha^{(s)}(\omega)$, vector $\alpha^{(v)}(\omega)$ and a tensor component $\alpha^{(t)}(\omega)$ which leads to a shift of energy levels that is independent (scalar), linearly dependent (vector), or quadratically (tensor) dependent on the Zeeman quantum number m_J. The applied electric field is denoted as $\vec{E}(t) = \frac{1}{2}|E|\hat{\epsilon}e^{i\omega t} + c.c.$ where $|E|$ is the field amplitude and $\hat{\epsilon}$ is a polarization vector of unit length. Note that $\hat{\epsilon}$ can be complex denoting elliptical polarization components. The resulting AC Stark shift can then be expressed

as [92]:

$$\Delta E = -\frac{|E|^2}{4}\left[\alpha^{(s)} - \alpha^{(v)}\Im(\epsilon_x^*\epsilon_y)\frac{m_J}{J} - \alpha^{(t)}\frac{(1-3|\epsilon_z|^2)}{2}\frac{(3m_J^2 - J(J+1))}{J(2J-1)}\right] \tag{3.1}$$

From this equation, if follows that linearly polarized light ($\Im(\epsilon_x^*\epsilon_y) = 0$) does not cause vector AC Stark shifts, even in case of a non-zero $\alpha^{(v)}$. With the remaining scalar and tensor terms, the energy shift then depends only on $|m_J|$[1]. Furthermore, it is interesting to note that the factor $(1 - 3|\epsilon_z|)$ is zero when the electric field of the light encloses an angle of $\arccos(1/\sqrt{3}) \approx 54.7°$ with the quantization axis. This solely means that the energies of all $|J, m_J\rangle$ states that are defined with respect to this tricky choice of the quantization axis are degenerate. However as they cease to be energy eigenstates, rates between those states will appear; this is analogous to the Larmor precession caused by a magnetic field that encloses a non-zero angle with the quantization axis. Therefore, the vanishing of the tensor term must in this case not be confused with vanishing differential light shifts between the actual energy eigenstates.

The dynamic polarizabilities $\alpha^{(s)}, \alpha^{(v)}$, and $\alpha^{(t)}$ can be calculated by summing the contributions of the couplings to different states. For state $|n\,J\rangle$ they are found to be

$$\alpha_{nJ}^{(s)} = \frac{1}{\sqrt{3(2J+1)}}\alpha_{nJ}^{(0)} \tag{3.2}$$

$$\alpha_{nJ}^{(v)} = -\sqrt{\frac{2J}{(J+1)(2J+1)}}\alpha_{nJ}^{(1)} \tag{3.3}$$

$$\alpha_{nJ}^{(t)} = -\sqrt{\frac{2J(2J-1)}{3(J+1)(2J+1)(2J+3)}}\alpha_{nJ}^{(2)} \tag{3.4}$$

where $\alpha_{nJ}^{(K)}$ is defined as:

$$\alpha_{nJ}^{(K)}(\omega) = (-1)^{K+J+1}\sqrt{2K+1}\sum_{n',J'}(-1)^{J'}\left\{\begin{array}{ccc} 1 & K & 1 \\ J & J' & J \end{array}\right\}$$
$$\times(2J+1)|\langle nJ||er||n'J'\rangle|^2\frac{1}{\hbar}\left(\frac{1}{\omega_{n'J'nJ}-\omega} + \frac{(-1)^K}{\omega_{n'J'nJ}+\omega}\right) \tag{3.5}$$

Here, $\omega_{n'J'nJ} = (E_{n'J'} - E_{nJ})/\hbar$ is the angular transition frequency between states $|n\,J\rangle$ and $|n'\,J'\rangle$, $\langle n'J'||d||nJ\rangle$ denotes the reduced matrix element of the transition between these two states, and the curly brackets denote the Wigner-6j-symbol. The formula is approximated assuming $\omega - \omega_{n'J'nJ} \gg \gamma$, where

[1]This is a consequence of time-reversal invariance [93]

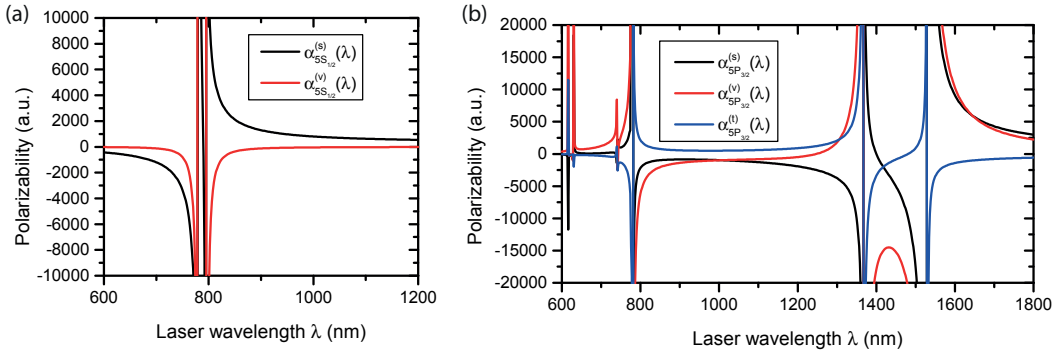

Figure 3.1.: Dynamical polarizabilities for ^{87}Rb (a) Scalar and vector polarizability of the $5S_{1/2}$ ground state. The polarizability is dominated by the D-line resonances. Towards greater wavelengths, the polarizabilities approach the static limit. (b) Scalar, vector and tensor polarizability of the excited $5P_{3/2}$ state. Besides the two D-line resonances at 780 nm and 795 nm, additional optical resonances appear at even greater wavelengths.

γ is the atomic polarization decay rate of any transition involved. As dipole traps typically work far detuned from any transition to avoid scattering, this assumption introduces a negligible error.

Looking up reduced matrix elements requires focus, as two different conventions are typically found. The convention used here relates the reduced matrix element of a given transition to the Einstein A coefficient as

$$|\langle nJ||d||n'J'\rangle|^2 = \frac{3\pi\epsilon_0\hbar c^3}{\omega^3_{n'J'nJ}}\frac{2J'+1}{2J+1}A_{n'J'nJ} \tag{3.6}$$

Thus far, the discussion has only covered effects that stem from the valence electron. As the remaining hull is tightly bound, its contribution to the atomic polarizability in the considered wavelength range is small and to a good approximation independent of the wavelength. The polarizability of the ionic core can be found in the literature [94] and is 9.1 a.u.[2].

3.2.1. Dynamic Polarizability

The result of calculations of the dynamic valence polarizabilities over a broad range of wavelengths is shown in Fig. 3.1. The line data that entered this calculation is summarized in appendix A. Panel (a) shows the scalar and vector polarizability of the $5S_{1/2}$ ground state. The tensor polarizability of this $J{=}1/2$ finestructure state is zero. The polarizability within the shown range of wavelengths is governed by two optical resonances, namely to the $5P_{1/2}$ state (D_1-line)

[2]The atomic unit for polarizability is 1 a.u. $= a_0^2e^2/E_h = 1.64878\cdot10^{-41}$ J(m/V)^2, where a_0 is the Bohr radius, e is the elementary charge, and E_h is the Hartree energy

	$\lambda = 1064\,\mathrm{nm}$	$\lambda = 772.37\,\mathrm{nm}$
$\alpha^{(s)}_{5S_{1/2}}$	686.8 a.u. (687.3 a.u. [96])	-11989 a.u.
$\alpha^{(v)}_{5S_{1/2}}$	-28.7 a.u.	-6689 a.u.
$\alpha^{(s)}_{5P_{1/2}}$	-1274 a.u. (-1226(18) a.u. [97])	1500 a.u.
$\alpha^{(v)}_{5P_{1/2}}$	-659.5 a.u.	3388 a.u.
$\alpha^{(s)}_{5P_{3/2}}$	-1129 a.u. (-1114 a.u. [97])	3460 a.u.
$\alpha^{(v)}_{5P_{3/2}}$	-874 a.u.	12756 a.u.
$\alpha^{(t)}_{5P_{3/2}}$	555 a.u. (551 a.u. [97])	-4840 a.u.

Table 3.1.: Calculated dynamical polarizabilities for the states and wavelengths relevant for the experiments presented in this thesis. The values in parentheses are theoretical calculations from other sources.

at 795 nm and to the $5P_{3/2}$ state (D_2-line) at 780 nm. The next higher dipole-allowed transition is at 422 nm ($6P_{1/2}$). As the D-lines are energetically the lowest transitions, the polarizabilities converge towards their static limit with increasing wavelength. The static limit is calculated as $\alpha^{(s)}(\lambda \to \infty) = 318$ a.u. in agreement with a published value [95] of 329(23) a.u.

The polarizabilities calculated for the $5P_{3/2}$ state shown in panel (b) strongly deviate from the ground state polarizability, owing to additional optical resonances to even higher excited states. In particular, coupling to the $4D_{3/2}$, $4D_{5/2}$ and $6S_{1/2}$ states at wavelengths around 1.5 μm dominates the polarizabilities for larger wavelengths.

The wavelengths that are relevant to all of the experiments documented in this thesis are those of the two dipole traps at 1064 nm and 772.37 nm. Table 3.1 summarizes the calculated scalar, vector, and tensor polarizabilities. At a wavelength of 1064 nm, which is red detuned with respect to the dominant D-line transitions, the ground state has positive polarizability. Thus, intensity maxima correspond to minima in the generated mechanical potential. The opposite holds for the 772.37 nm trapping light, which is blue detuned to the D-lines and creates a repulsive trap in which intensity maxima coincide with maxima of the generated mechanical potential. In this case, atoms will be confined to nodes of a standing-wave light field.

3.2.2. Decoupling of the Hyperfine Spin

The discussion has thus far focused on finestructure states $|J, m_J\rangle$. In general, AC Stark shifts will lift the degeneracy of m_J states within a given J manifold. In an alkali atom, hyperfine interaction of the valence electron with the nuclear magnetic dipole and electric quadrupole moment will occur. In the absence of magnetic fields and AC Stark shifts, eigenstates of a coupled hyperfine spin

$|F, m_F\rangle$ will be energy eigenstates instead of the $|J, m_J\rangle$ states of the electronic hull and $|I, m_I\rangle$ states of the nucleus. The application of an AC Stark-shifting light field in the presence of hyperfine interaction then leads to a situation that is similar to the Paschen-Back effect in the case of a magnetic field.

The total Hamiltonian, including AC Stark shifts and hyperfine interaction, will not be diagonal in the fine-structure or the hyperfine-structure basis. In case of AC Stark shifts that are small compared to the hyperfine interaction, the hyperfine states $|F, m_F\rangle$ remain energy eigenstates to a good approximation and can be assigned polarizabilities. Their AC Stark shift can then be calculated with equation 3.1 by replacing J with F, m_J with m_F and using the following approximate polarizabilities [92]:

$$\alpha^{(s)}_{nJF} = \frac{1}{\sqrt{3(2J+1)}}\alpha^{(0)}_{nJ} \tag{3.7}$$

$$\alpha^{(v)}_{nJF} = (-1)^{J+I+F}\sqrt{\frac{2F(2F+1)}{F+1}}\begin{Bmatrix} F & 1 & F \\ J & I & J \end{Bmatrix}\alpha^{(1)}_{nJ} \tag{3.8}$$

$$\alpha^{(t)}_{nJF} = (-1)^{J+I+F}\sqrt{\frac{2F(2F-1)(2F+1)}{3(F+1)(2F+3)}}\begin{Bmatrix} F & 2 & F \\ J & I & J \end{Bmatrix}\alpha^{(2)}_{nJ} \tag{3.9}$$

where $\alpha^{(K)}_{nJ}$ is given by equation 3.5. Note that the approximate tensor polarizability of the hyperfine states can be related to the finestructure tensor polarizability by $\alpha^{(v)}_{nJF} = \frac{3X(X-1)-4F(F+1)J(J+1)}{(2F+3)(2F+2)J(2J-1)}$ with $X = F(F+1)+J(J+1)-I(I+1)$, a relation that is known from the case of static electric fields [98]. Table 3.2 summarizes the calculated small-field approximations for the relevant wavelengths. The scalar polarizabilities are not shown as they are identical to the finestructure states' scalar polarizability, which can be found in Table 3.1. The excited $F = 0$ state is omitted as well, as its vector and tensor polarizabilities are zero. Where applicable, literature values (values in parentheses in Table 3.1) that are typically calculated with more elaborate methods [99] have been used instead of the calculated values.

For AC Stark shifts that are comparable to the hyperfine-interaction energy, neither the $|F, m_F\rangle$ state nor the $|J, m_J\rangle$ states will be energy eigenstates. In order to find the new energy eigenstates of the perturbed atom, the total Hamiltonian $\mathcal{H}$ that contains AC Stark shifts $\mathcal{H}^{\mathrm{ACS}}$ and hyperfine interaction $\mathcal{H}^{\mathrm{HFI}}$ must be diagonalized. The diagonal elements of $\mathcal{H}^{\mathrm{ACS}}$ are given by equation 3.1 and are transformed into the hyperfine basis:

$$\mathcal{H}^{\mathrm{ACS}} = \sum_{\substack{F,m_F \\ F',m'_F}} \left(\sum_{m_J,m_I} E^{\mathrm{ACS}}_{J,m_J}\, C^{F,m_F}_{J,m_J,I,m_I}\, C^{F',m'^{*}_F}_{J,m_J,I,m_I} \right) |F, m_F\rangle\langle F', m'_F|, \tag{3.10}$$

where $C^{J_3,m_3}_{J_1,m_1,J_2,m_2}$ are Clebsch-Gordan coefficients. The hyperfine interaction

	$\lambda = 1064\,\mathrm{nm}$	$\lambda = 772.37\,\mathrm{nm}$
$\alpha^{(v)}_{5S_{1/2},F=1}$	14.3 a.u.	3344 a.u.
$\alpha^{(v)}_{5S_{1/2},F=2}$	-28.7 a.u.	-6688 a.u.
$\alpha^{(v)}_{5P_{1/2},F=1}$	329.5 a.u.	-1695 a.u.
$\alpha^{(v)}_{5P_{1/2},F=2}$	-659.1 a.u.	3389 a.u.
$\alpha^{(v)}_{5P_{3/2},F=1}$	-291 a.u.	4252 a.u.
$\alpha^{(t)}_{5P_{3/2},F=1}$	-222 a.u.	1935 a.u.
$\alpha^{(v)}_{5P_{3/2},F=2}$	-583 a.u.	8504 a.u.
$\alpha^{(t)}_{5P_{3/2},F=2}$	0 a.u.	0 a.u.
$\alpha^{(v)}_{5P_{3/2},F=3}$	-874 a.u.	12756 a.u.
$\alpha^{(t)}_{5P_{3/2},F=3}$	555 a.u.	-4840 a.u.

Table 3.2.: Approximate dynamical polarizabilities of hyperfine states. Scalar polarizabilities are not given as those are identical to the finestructure state's scalar polarizability which can be found in table 3.1.

energy is diagonal in the hyperfine basis $\mathcal{H}^{\mathrm{HFI}} = \sum_{F,m_F} E^{\mathrm{HFI}}_{F,m_F} |F,m_F\rangle\langle F,m_F|$ and the corresponding diagonal elements E^{HFI}_{F,m_F} are given by

$$E^{\mathrm{HFI}}_{F,m_F} = A_{\mathrm{HFI}}\frac{K}{2} + B_{\mathrm{HFI}}\frac{3/2K(K+1) - 2I(I+1)J(J+1)}{4I(2I-1)J(2J-1)}, \tag{3.11}$$

where $K = F(F+1) - I(I+1) - J(J+1)$. The values of the magnetic dipole constants A_{HFI} and electric quadrupole constants B_{HFI} of the relevant states are taken from [100] (and references therein). Because the projection of the coupled hyperfine spin onto the quantization axis $m_F = m_I + m_J$ is a good quantum number in both bases, the Hamiltonian will be block-diagonal. Off-diagonal elements will appear only between states that have a different hyperfine spin F but identical m_F.

Figure 3.2 shows the results of a numerical calculation of the energy eigenstates in the $5P_{3/2}$-manifold that are perturbed by off-resonant, linearly polarized light at wavelengths of (a) 1064 nm and (b) 772.37 nm. These energy eigenvalues are shown as a function of the intensity $I = \frac{1}{2}c\epsilon_0 E^2$ of a plane traveling light wave.

- For vanishing intensity, the unperturbed hyperfine structure of the $5P_{3/2}$ state is found with values of the hyperfine spin F ranging from 0 to 3. For small intensities, the numerically calculated values agree with the small-field approximation (dotted lines).

- In the case of high intensities, the hyperfine structure breaks down and m_I

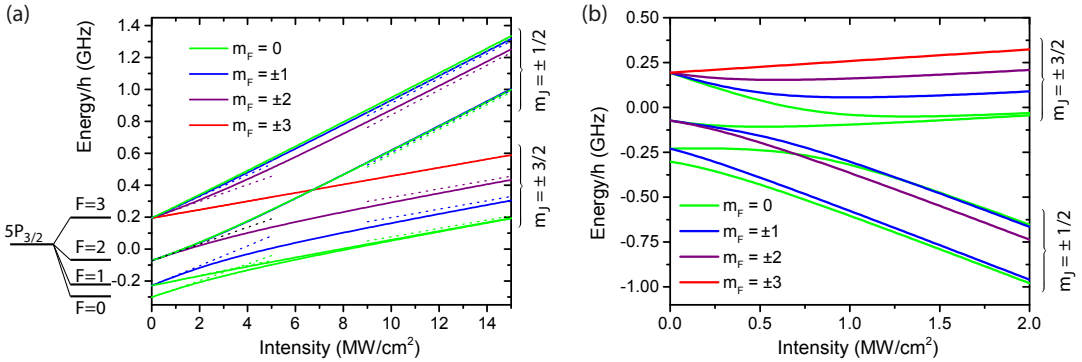

Figure 3.2.: Energy eigenstates in the $5P_{3/2}$ manifold perturbed by a strong off-resonant light field (a) Calculated for $\lambda = 1064\,\mathrm{nm}$. The dotted lines on the left side of the graph indicate the approximate small-field solution. The dotted lines on the right side show the high-field results. These are valid for differential light shifts within the finestructure manifold in excess of the typical hyperfine interaction energy. (b) Calculated energy eigenstates for $\lambda = 772\,\mathrm{nm}$.

and m_J are good quantum numbers. The energy eigenvalues will depend linearly on the intensity with a slope that is given by the polarizabilities $\alpha_{|m_J|=1/2} = (\alpha^{(s)} - \alpha^{(t)})$, and $\alpha_{|m_J|=3/2} = (\alpha^{(s)} + \alpha^{(t)})$, respectively. The residual offsets of the states that are caused by the hyperfine interaction can be calculated in first order perturbation theory as the expectation value of the $\mathcal{H}^{\mathrm{HFI}}$ in the finestructure basis and are shown as dotted lines.

- For intermediate intensities, the energy eigenstates are not eigenstates of the finestructure or hyperfine structure spin and appear as complex superposition states when expressed in either of the two bases.

For both wavelengths, the absolute value of the polarizability of the $|m_J| = 1/2$ states is greater than that of the $|m_J| = 3/2$ states, due to coupling to the $J = 1/2$ ground state (which is the dominant contribution to the polarizability in both cases). With a choice of the quantization axis along the light's electric field, only π-polarized transitions will be driven. This leaves the excited $|m_J| = 3/2$ states uncoupled and only their coupling to even higher excited states $J \geq 3/2$ contribute to the polarizability of these two Zeeman states.

The red line that corresponds to the $|m_F| = |m_I + m_J| = 3$ states is a straight line for all wavelengths, as it is an eigenstate of both the finestructure and hyperfine structure spins J, I, and F. This holds not only for the considered case of linearly polarized light, and is also true for the $|5S_{1/2}, F = 2, m_F = \pm 2\rangle$ ground states. The cycling transitions will thus not be affected by effects of hyperfine breakdown.

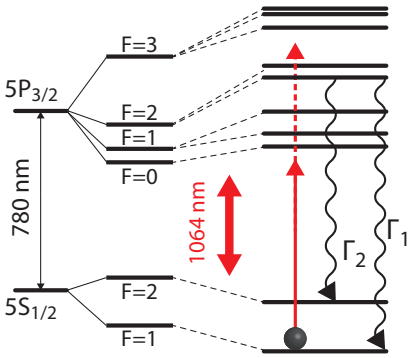

Figure 3.3.: Spectroscopy of exited energy eigenstates perturbed by the dipole trap Initialization of the atom in $|5S_{1/2}, F = 1\rangle$ is followed by impinging probe light (red) with a frequency that is changed between repetitions of the experiment. When the probe light happens to be resonant with the transition to an excited state, population in this state will lead to decay rates back to the F=1 ground state (with rate Γ_1) and to the F=2 ground state (with rate Γ_2). Population of F=2 is detected and serves as a spectroscopic signal.

3.3. Experimental Results

Many of the experiments that are discussed in this thesis contain resonant optical excitation. Precise knowledge about the structure of excited energy eigenstates that are perturbed by the dipole trap is therefore essential. The intensity of the light used to create the optical dipole traps is difficult to estimate from first principles, as many involved geometric parameters (e.g. overlap of two counter-propagating running waves) are not known with sufficient accuracy. Spectroscopy of the trapped atoms is therefore used as a tool to measure the intensity at the position of an atom by using that atom itself as a probe.

Despite the broad spectrum of applications of optical dipole traps, experimental characterization of electronically excited states that are perturbed by the trapping light is a largely unexplored topic. Few studies on magic wavelengths [101] and two measurements of a tensor light shift on excited hyperfine states [102, 103] are published.

3.3.1. Experimental Technique and Line Shapes

Spectroscopy of the perturbed excited energy eigenstates of a single trapped atom is performed by detecting changes in the ground state's hyperfine spin that are caused by the inelastic resonant scattering of a probe beam. To this end, the atom is initially prepared in the $5S_{1/2}, F = 1$ ground state by optical pumping (see Chapter 2.3). A weak probe beam is then shone onto the atom for a duration $T = 2\,\mu\text{s} \gg 1/\Gamma$ that is longer than the lifetime of the excited state. The probe pulse propagates along the $-45°$-axis (see Chapter 2.1) and

its linear polarization lies in the xy-plane. The electric field is thus oriented perpendicular to the cavity axis and the 1064 nm trap polarization. In the atomic coordinate frame with the quantization axis chosen along the electric field of the trap light, the probe pulse drives σ^+ and σ^- transitions with equal strength. If the frequency of the probe pulse happens to be resonant with the transition from the F=1 ground state to an excited state, the excited state can be populated and will decay by spontaneous emission.

In contrast to observing the light emitted during the transfer, the change in ground-state population that results from a decay into F=2 can be detected with unity efficiency by employing cavity-assisted hyperfine-state detection (see Chapter 2.5.1). The described technique is sketched in Fig. 3.3.

The observable transition lines are expected to deviate from a radiatively broadened Lorentzian profile due to residual thermal excitation of the atom's motion. In the following paragraphs, the expected line shapes are derived in a general manner. Intermediate results of the derivation are used in later chapters (e.g., Chapter 6.4.1).

The polarizability of the ground state, which creates the mechanically confining potential, generally differs from the excited state's polarizabilities and mechanical excursions of the atom will therefore lead to a shift of the transition frequency. The confining potential of the ground state $U_g(\boldsymbol{x})$ can be approximated quadratically in all three spatial directions (see Chapter 4.2) $U_g(\boldsymbol{x}) \approx \sum_{i=1}^{3} m\omega_i^2 x_i^2/2$. Here, m is the atomic mass and $\omega_i = \sqrt{(\partial^2 U(\boldsymbol{x})/\partial x_i^2)/m}$ are the angular trap frequencies along the different spatial directions. In a simple model, a semiclassical approximation is made for the position distribution $n(\boldsymbol{x})$ of the atom

$$n(\boldsymbol{x}) = n_0 e^{-\beta U_g(\boldsymbol{x})} \tag{3.12}$$

with $\beta = 1/k_B T$, k_B the Boltzmann constant and T the temperature of the atom. By requiring that the distribution is normalized to 1, the peak density is found to be $n_0 = (m\bar{\omega}^2/2\pi k_B T)^{3/2}$, where $\bar{\omega} = (\omega_x\omega_y\omega_z)^{1/3}$ is the harmonic mean of the angular trapping frequencies. The detuning of the atom as a function of the position is expressed as $\Delta(\boldsymbol{x}) = \Delta_0 + \frac{\alpha_e - \alpha_g}{\hbar\alpha_g} U_g(\boldsymbol{x})$. Here $\alpha_{e/g}$ indicate the dynamical polarizability of the ground and excited state respectively. Δ_0 denotes the detuning of an atom at the bottom of the trap ($\boldsymbol{x} = 0$). The expectation value of a function $f(\Delta)$ that depends on the atomic detuning is then identified as:

$$\langle f(\Delta(\boldsymbol{x}))\rangle_{\boldsymbol{x}} = \bar{\omega}^3 \left(\frac{m}{2\pi k_B T}\right)^{3/2} \int d^3\boldsymbol{x} f\left(\Delta_0 + \frac{\alpha_e - \alpha_g}{\hbar\alpha_g} U_g(\boldsymbol{x})\right) \tag{3.13}$$

The coordinates x_i are rescaled by the respective trap frequency in order to yield rotational symmetry $x_i \to \omega_i x_i/\bar{\omega}$. The Jacobian determinant of this transformation is 1. The integral in transformed coordinates depends only on $r = |\boldsymbol{x}|$ and the azimuthal and polar angle of $\boldsymbol{x}$ in spherical coordinates can be

integrated, yielding:

$$\langle f(\Delta(\boldsymbol{x}))\rangle_{\boldsymbol{x}} = \bar{\omega}^3 \left(\frac{m}{2\pi k_B T}\right)^{3/2} 4\pi \int_0^\infty dr\, f\left(\Delta_0 + \frac{\alpha_e - \alpha_g}{\hbar\alpha_g}\frac{m}{2}\bar{\omega}^2 r^2\right) r^2 e^{-\beta\frac{m}{2}\omega^2 r^2} \tag{3.14}$$

Another coordinate transformation $\beta m\bar{\omega}^2 r^2/2 \to r^2$ yields the following general result that does not make assumptions about $f(\Delta)$

$$\langle f(\Delta(\boldsymbol{x}))\rangle_{\boldsymbol{x}} = \frac{4}{\sqrt{\pi}} \int_0^\infty dr\, f(\Delta_0 + \tau r^2) r^2 e^{-r^2} \tag{3.15}$$

with $\tau = \frac{\alpha_e - \alpha_g}{\hbar\alpha_g} k_B T$ as a temperature parameter that scales with the relative difference of ground- and excited state polarizability. At a magic wavelength ($\alpha_g = \alpha_e$), τ will be independent of the actual temperature T.

For the AC Stark shift spectroscopy, the function $f(\Delta)$, which depends on the atomic detuning will be the population that was transferred into F=2. As the probe pulse is long in comparison to the time scale on which coherences decay, its action on the atom can be described with a rate equation model. The steady state population ρ_{ee} of an excited state $|e\rangle$, which is coupled to the F=1 ground state $|g\rangle$ by the probe laser of intensity I that is detuned by Δ from the $|g\rangle \leftrightarrow |e\rangle$ transition, is:

$$\rho_{ee} = \frac{I_p}{2I_s} \frac{1}{1 + [2\Delta/\Gamma]^2}, \tag{3.16}$$

where I_s is the transition's saturation intensity, $I_p \ll I_s$ is the intensity of the probe light, and $\Delta = \omega_{\text{probe}} - \omega_{ge}$ is the detuning of the laser from the potentially AC-Stark-shifted atomic transition at ω_{ge}. Population of the excited state will lead to a partial decay rate $\Gamma_2\rho_{ee}$ into the F=2 ground state, such that after a probing duration d an atomic population $P_2 = \Gamma_2\rho_{ee}d$ will have been transferred to the F=2 state. This simplified model assumes that $\Gamma_2\rho_{ee}d \ll 1$, such that effects of depletion of the $F = 1$ state can be neglected. The saturation intensity I_s will be different for every observed transition and change with different settings of the trap power as the excited energy eigenstates change. Furthermore, the initial population of the Zeeman states in the F=1 manifold after optical pumping is unknown. Making quantitative predictions about the amplitude of the observed transfer lines is therefore unrealistic. All prefactors are thus subsumed in a general scaling factor and application of equation 3.15 yields the following dimensionless spectrum

$$\langle P_2(\Delta)\rangle_{\boldsymbol{x}} \propto \int_0^\infty dr\, \frac{r^2 e^{-r^2}}{1 + 4(\delta + \tau' r^2)^2}, \tag{3.17}$$

where $\tau' = \tau/\Gamma$ is a dimensionless temperature parameter and $\delta = \Delta/\Gamma$ is a dimensionless detuning. For $\delta, \tau \in \mathbb{R}$, and $\tau \neq 0$, the following analytical

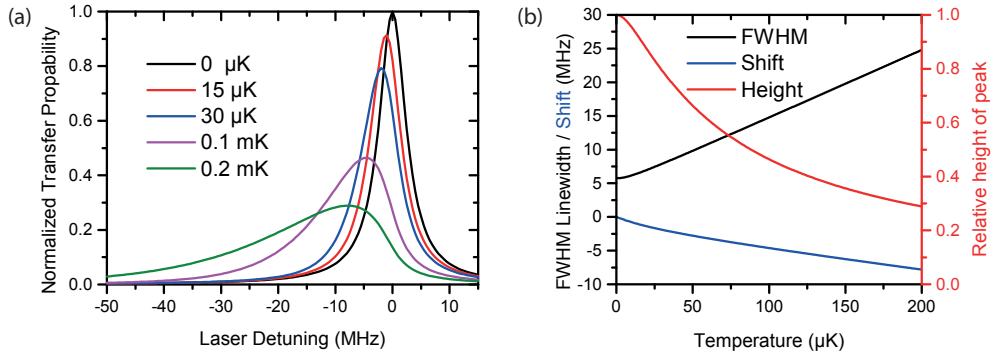

Figure 3.4.: Inhomogeneously broadened lineshapes (a) Simulated lineshapes including inhomogeneous broadening due to residual atomic temperature. The curves are calculated using parameters valid for the D_1 line. (b) Overview of the different effects onto the observed transitions due to inhomogeneous thermal broadening.

solution is available [104]:

$$\langle P_2(\Delta)\rangle_{\boldsymbol{x}} \propto \frac{\pi}{4\tau}\Re(z\,w(z)),\quad z=\sqrt{\frac{i-2\delta}{2\tau'}} \tag{3.18}$$

where $w(z) = e^{-z^2}\mathrm{erfc}(-i\,z)$ is the Fadeeva function [104] and $\mathrm{erfc}(z) = 1 - \mathrm{erf}(z) = 1 - \frac{2}{\sqrt{\pi}}\int_0^z e^{-t^2}dt$ is the complementary error function.

Figure 3.4(a) shows the results of this model (i.e., thermally broadened transition lines for different temperatures). The curves were calculated with equation 3.18 using the polarizability values $\alpha^{(s)}_{5S_{1/2}} = 686\,\mathrm{a.u.}$ and $\alpha^{(s)}_{5P_{1/2}} = -1274\,\mathrm{a.u.}$ and the decay rate $\Gamma = 2\pi\cdot 5.75\,\mathrm{MHz}$ of the D_1 line. The inhomogeneous broadening caused by thermal fluctuations is asymmetric. This stems from the fact that the atomic transition frequency is reduced (in the case of a red-detuned trap) regardless of which direction the atom is displaced with respect to the trap center. For low temperatures, the asymmetry is barely noticeable and deviations from a Lorentzian will only become prominent for temperatures in excess of $50\,\mu\mathrm{K}$ for this particular set of parameters. Moreover, the inhomogeneous broadening causes the line to shift towards smaller frequencies. The three major effects of thermal excitation, namely broadening and shift of the line, and decrease of the maximum amplitude, are plotted in Fig. 3.4(b) as a function of the temperature.

The theory presented here makes several simplifying assumptions. The ratio $(\alpha_e - \alpha_g)/\alpha_g$ was applied to the motion along all three spatial directions. In the experiment, the confinement along the x- and y-axis was provided by a red-detuned trap at 1064 nm, while a blue-detuned trap at 772 nm provides strong confinement along the z-axis[3]. The values of τ calculated for the two

[3] An extended discussion of this topic can be found in the appendix of reference [105]

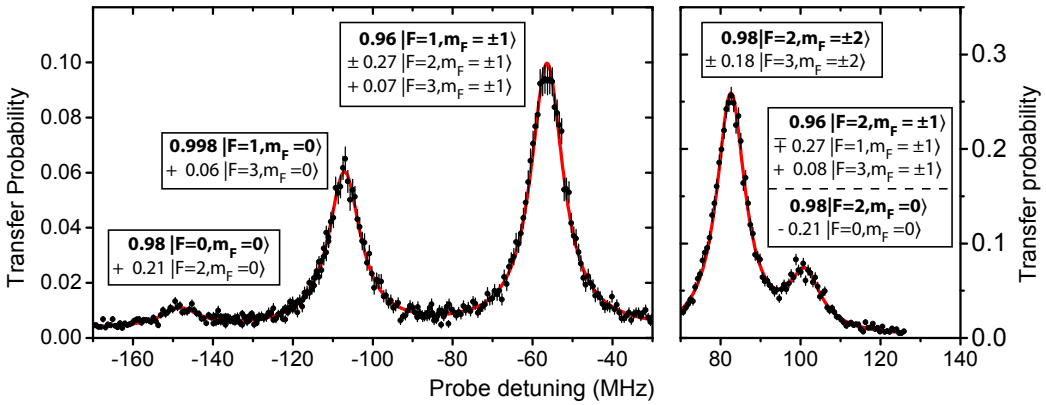

Figure 3.5.: Spectroscopy of excited states perturbed by the trap light Single spectrum recorded at $P_{1064} = 2.25\,\mathrm{W}$. Five resonances are clearly visible. The peaks are labeled with the energy eigenstates expressed in the hyperfine basis (see text). Splitting of the F=2 state (double peak in the very right part of the spectrum), which is not predicted in the weak-field approximation, is an unambiguous indication of hyperfine-breakdown. The leftmost peak indicates a state which for weak power coincides with the unperturbed F=0 state. The F=0 state does not decay to the F=2 ground state. The fact that population transfer is observable here stems from the admixture of the $F = 2, m_F = 0$ excited state to the energy eigenstate.

wavelengths differs for some states by a maximum factor of three. Furthermore, this theory assumes that all three axes are thermalized and described by a classical Boltzmann distribution. However, there is experimental evidence (see Chapter 4.4.3) that this is not the case. Temperatures that are extracted by application of this model to AC Stark shift spectra like the one in Fig. 3.5 are typically $\geq 30\,\mu\mathrm{K}$, which corresponds to a thermal energy of $k_B T \approx h \times 600\,\mathrm{kHz}$. This value does not exceed trap frequencies that were used in the experiment (which were typically between 300 and 600 kHz) by far, as would be required for the application of the semi-classical approximation. While these problems cast doubt onto the quantitative validity of the extracted temperatures, the model successfully describes the influence of thermal broadening in several different experiments including cavity-reflection spectroscopy (see Chapter 6.4.1) and scattering experiments with a single atom and two atoms (see Chapters 6.4.2 and 6.6).

3.3.2. Spectroscopic Results

After loading a single atom (see Chapter 2.3), the experimental sequence, interleaved with molasses cooling intervals was repeated at 2 kHz until fluorescence images indicated the loss of the atom. The frequency of the probe laser was swept once per second over a frequency interval that typically covers 60 MHz. Spectra of the transitions to the excited $5P_{1/2}$ and $5P_{3/2}$ states were recorded

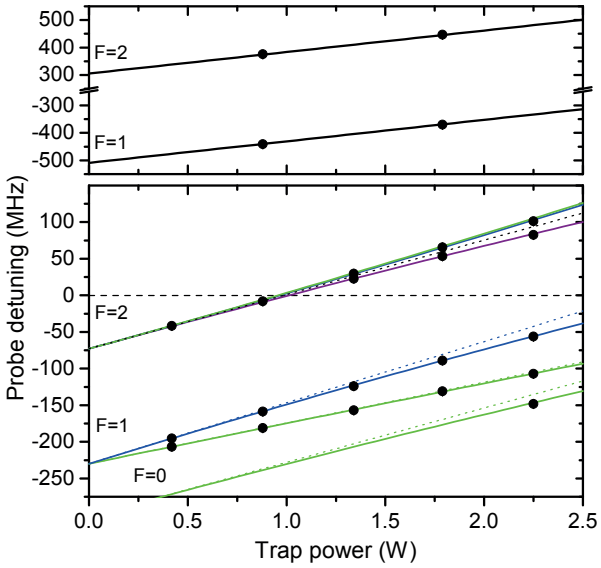

Figure 3.6.: Line positions vs. trap power Frequencies of the observed transfer lines as a function of the applied trap power P_{1064}. The upper panel shows data recorded on the D_1 line. Due to the absence of tensor polarizability, the two hyperfine components shift linearly with the applied power. The black lines are fitted to the data. The lower panel shows data recorded on the D_2 line. The solid lines are calculated with theoretical model described in the text. The color encode the $m_F = m_I + m_J$ quantum number of the particular state (green=0, blue=$\pm$1, purple=$\pm$2). The dotted lines show the small-field approximation that neglects hyperfine breakdown.

for different settings of the 1064 nm dipole trap power P_{1064}. Since the 1064 nm trap is red detuned, atoms are trapped at maxima of $|E|^2$, whereas the opposite holds for the blue-detuned intracavity trap. Residual shifts of the blue-detuned trap are on the order of the trapping frequency, which is far below the linewidth of the observed electronic transitions. This was verified experimentally by repeating spectroscopy of a single transition line for two different potential heights of the blue trap that were a factor of two apart; a negligible shift of 79(91) kHz was found.

Figure 3.6 shows a single spectrum that was recorded at $P_{1064} = 2.25\,\mathrm{W}$ on the D_2 line. Five resonances are clearly distinguishable and fitted with a multiple Lorentzian fit (red line). The fitted widths of the resonance lines are larger than the free space value $\Gamma/2\pi = 6.1\,\mathrm{MHz}$ by a factor of approximately 1.5. Applying the previously discussed model, this corresponds to a temperature of 30 μK, which is consistent with the hardly observable deviation from a Lorentzian profile (see Fig. 3.3) and yields an expected lineshift towards smaller frequencies of 2 MHz. The fitted line centers found for different trap powers are shown in Fig. 3.6. The y-axis is scaled such that zero corresponds to the transition frequency from the $|5S_{1/2}, \mathrm{F}{=}1\rangle$ ground state to the unperturbed excited

finestructure state.

In order to fit the theory described in the previous section, the electric field strength of the trap light must be modeled as a function of the applied power. The waist of the incident dipole-trap beam was measured $w_i = 3.17\,\mathrm{mm}$. This beam is focused into the cavity region with a lens that has a focal length of $f = 150\,\mathrm{mm}$, which yields a focal waist of $w_0 = \frac{1064\,\mathrm{nm}\cdot 0.15\,\mathrm{m}}{\pi w_i} = 16\,\mu\mathrm{m}$. The focal intensity of a running wave beam with power P_{1064} is $I = \frac{2P_{1064}}{\pi w_0^2}$ and the squared electric field in a retroreflected beam of the same geometry is $|E|^2 = \eta\frac{16P_{1064}}{\pi c\epsilon_0 w_0^2}$. Here, $\eta \leq 1$ is a factor that describes experimental imperfections such as imperfect overlap of the two beams that change the power calibration.

The upper panel of Fig. 3.6 shows transitions on the D_1 line ($5S_{1/2} \leftrightarrow 5P_{1/2}$) at 795 nm. As the excited state is a $J = 1/2$ state, no breakdown of hyperfine coupling is expected from the linearly polarized light and the resonance positions are expected to shift linearly with the applied power. The slope is given by $-\frac{1}{4}\eta\Delta\alpha_{1/2}$, where $\Delta\alpha_{1/2} = (\alpha^{(s)}_{5S_{1/2}} - \alpha^{(s)}_{5P_{1/2}})$ is the difference in polarizability of the ground and excited states. A fit to the data (black lines in the figure) yields $\eta\Delta\alpha_{1/2} = -1675(3)$ a.u. and a hyperfine interval of $(E_{F=2} - E_{F=1})/h = 816.6(2)\,\mathrm{MHz}$; the uncertainties are purely statistical. As the polarizabilities of both states and the power calibration do not enter in the determination of the hyperfine interval, this value can be measured with small systematic error. In the literature, only two measurements of $5P_{1/2}$ state hyperfine interval are found. The value obtained in the experiment described here is in agreement with $(E_{F=2} - E_{F=1})/h = 816.66(3)\,\mathrm{MHz}$ as reported in [106]. The second published value of 812.29(3) MHz [107] deviates by 20 standard deviations from the value reported in [106] and the value measured here.

The lower panel of Fig. 3.6 shows data from the D_2 line ($5S_{1/2} \leftrightarrow 5P_{3/2}$) at 780 nm. A fit yields $\eta\Delta\alpha_{3/2} = -1590(3)$ a.u. for the difference in scalar excited- and ground-state polarizability and $\alpha^{(t)}_{5P_{3/2}}/\Delta\alpha_{3/2} = -0.312(4)$. The second quantity is an atomic property that can be measured independently of η. Another such quantity is found in the ratio $\Delta\alpha_{1/2}/\Delta\alpha_{3/2} = 1.054(2)$. From the values found in the literature (see Table 3.1), the following predictions can be calculated: $\Delta\alpha_{1/2}/\Delta\alpha_{3/2} = 1.062(14)$ and $\alpha^{(t)}_{5P_{3/2}}/\Delta\alpha_{3/2} = -0.306(4)$ in agreement with the values that were measured in the experiments described here.

Another approach to data evaluation is to determine η using the theoretical values for $\alpha^{(s)}_{5S_{1/2}}$ and $\alpha^{(s)}_{5P_{1/2}}$ to yield $\eta = 0.876(8)$, $\alpha^{(s)}_{5P_{3/2}} = -1128(18)$ a.u. and $\alpha^{(t)}_{5P_{3/2}} = 568(9)$ a.u.. The power calibration can easily deviate from one as it is difficult to ensure that the focal points of both counter-propagating beams are positioned precisely in the center of the cavity and are well-aligned with each other. The measured scalar polarizability of the $5P_{3/2}$ state is congruent with the theory value, while the tensor polarizability deviates by 2σ.

The fitted model permits the calculation of the energy eigenstates that correspond to the peaks in Fig. 3.5. At low trap powers, the leftmost peak is not

visible as it converges to the excited F=0 hyperfine state that cannot decay to the F=2 ground state. The fact that this peak is visible is due to a coupling caused by the 4 % admixture of the excited F=2 state. This is a clear consequence of hyperfine breakdown in an optical dipole trap. The violation of a free-space dipole selection rule has experimental consequences. As an example, when attempting hyperfine state detection on the $|5S_{1/2}, \mathrm{F}{=}1\rangle \leftrightarrow |5P_{3/2}, \mathrm{F}{=}0\rangle$ transition, it was always found that the achievable discrimination thresholds of the light and dark states were limited by unintended optical pumping to the dark F=2 ground state (see chapter 2.5.1). Hyperfine breakdown of the excited F=0 state contributes to this detrimental effect.

Another clear signature of the hyperfine breakdown is the appearance of two separable peaks in the very right part of Fig. 3.5, which converge to the F=2 excited state for low powers. In the low field approximation that ignores hyperfine breakdown, all Zeeman states of $5P_{3/2}, F = 2$ are expected to remain degenerate.

4. Trap Geometry and Cooling Dynamics

4.1. Introduction

In earlier experiments that were conducted on the apparatus [77,108–112], atoms were trapped in a one-dimensional optical lattice. The lattice was generated with a retroreflected beam that traverses the cavity along the x-axis. While the atoms were tightly confined along the x-axis owing to the standing-wave structure of the light, confinement along the cavity axis was only provided by the Gaussian envelope of the trapping beam[1]. This typically allows mechanical excursions of the trapped atom over a full wavelength of the standing-wave cavity mode structure. As a consequence, the coupling strength g fluctuated between its theoretical maximum and an uncoupled system $g = 0$ whenever the atom was traversing a node of the cavity mode. While many earlier experiments could tolerate this fluctuation, the envisioned two-atom experiment relies on the atoms being continuously coupled to the cavity with a well-known coupling strength, and, just as important, a well-known and constant spatial distance between the atoms. Therefore, a two-dimensional trap was implemented that is comprised of an one-dimensional lattice along the x-axis and an additional, repulsive lattice along the cavity axis. The geometry of the trapping potential and the resulting energy spectrum of a single trapping site is discussed in the first section of this chapter.

In experiments with ultracold quantum gases [114, 115], atoms are typically cooled to ultracold temperatures before they are transferred into the final trapping potential. Besides evaporative cooling that does not maintain the atom number, no further cooling is performed and heating of the trapped ensemble cannot be counteracted. In contrast to this, many experiments with single atoms [83, 84, 113, 116–119], including those reported in this thesis, are carried out by cooling the atoms while they are trapped in the final configuration. As a result, many repetitions of an experiment can be performed without the need to repeat a potentially lengthy loading procedure. Raman sideband cooling to

[1] In fact, the light used for length stabilization of the cavity by a Pound-Drever-Hall technique created a mechanical potential in earlier experiments. But, with exception of the cavity-cooling experiments by Stefan Nußmann [113], no effect of this potential was observed and it is unlikely that low enough atomic temperatures were achieved in subsequent experiments.

the motional ground state of the atom is described in Chapter 4.3.

The geometry of the two-dimensional optical lattice deviates slightly from perfect orthogonality. This leads to motional coupling of each individual trapping site's eigenmotions [120]. Raman sideband spectroscopy was used to quantify this effect and a deviation of 1.26(57)° from orthogonality was; this value is consistent with the value of 1.55(2)° that was found by evaluating fluorescence images of the lattice (see Chapter 2.4). The data and the theoretical evaluation are presented in Chapter 4.4.

4.2. Energy Spectrum of a Single Trapping Site

The two-dimensional optical lattice is generated in the intersection region of the TEM_{00} cavity mode and a one-dimensional optical lattice along the x-axis. Both traps are created by standing-wave light beams with Gaussian envelopes. As the intracavity trap along the z-axis is blue-detuned, it confines atoms to nodes of the light field and does not provide any confinement along the x- and y-axis. The standing-wave structure of the red-detuned beam along the x-axis generates strong confinement along the x-axis. Along the y-axis, the atoms are confined solely due to the envelope of the 1064 nm beam.

In this section, the energy spectrum of the two individual traps is discussed and Chapter 4.4 focuses on mechanical effects that arise from the combination of the two beams.

The mechanical potential generated by the 1064 nm beam with an incident power of P_{1064} for a ground-state atom is given by:

$$U_{g,1064}(\vec{r}) = -\frac{1}{4}\left(\frac{16\,P_{1064}\,\eta}{\pi\,c\,\epsilon_0 w_{1064}^2}\right)\alpha_{1064}^{(s)}\cos\left(\frac{2\pi\,x}{1064\,\mathrm{nm}}\right)^2 e^{-\frac{2(y^2+z^2)}{w(x)^2}}, \tag{4.1}$$

where $w(x) = w_{1064}\sqrt{1+(z/z_0)^2}$ describes the divergence of the beam waist with $w_{1064} = 16\,\mu$m as the focal waist, $z_0 = \pi\,w_{1064}^2/\lambda = 0.8\,$mm as the Rayleigh range and $\eta = 0.876(8)$ is a measured power calibration factor that summarizes alignment-related effects (see Chapter 3.3.2). The potential has a minimum at $x = 0$ and a Taylor series expansion along the x-axis that neglects the beam divergence (which changes the intensity on a length scale that is large compared to the wavelength of the light) yields:

$$U_{g,1064}(x, y=z=0) = \frac{4\,P_{1064}\,\eta\,\alpha_{1064}^{(s)}}{\pi\,\epsilon_0\,c\,w^2}\left[-1+\frac{1}{4}\left(\frac{4\pi}{1064\,\mathrm{nm}}\right)^2 x^2\right]+\mathcal{O}(x^4). \tag{4.2}$$

The constant offset contributes to line shifts (see Chapter 3.2) but is irrelevant to the motional dynamics of the atom. Setting the constant offset to zero, the mechanical Hamiltonian $\mathrm{H}_{\mathrm{mech}}$ can be written as a harmonic oscillator $\mathrm{H}_{\mathrm{mech}} =$

$\frac{p^2}{2m} + \frac{m\omega_x^2 x^2}{2}$, where $m = 1.443 \cdot 10^{-25}\,\mathrm{kg}$ is the mass of a single ^{87}Rb atom and

$$\omega_x = \sqrt{\frac{2P\,\eta\,\alpha^{(s)}_{1064}}{\pi\,\epsilon_0\,c\,w^2_{1064}\,m}\left(\frac{4\pi}{1064\,nm}\right)^2} \tag{4.3}$$

is the angular frequency of the oscillator. The majority of the experiments that are described in the following chapters were conducted with $P_{1064} = 1.25\,\mathrm{W}$. Based upon the intensity calibration that was performed through spectroscopy of AC Stark shifted transitions (see Chapter 3.3.2), this value leads to a potential depth of $U_{g,1064} = -h \cdot 35\,\mathrm{MHz} = k_B \cdot 1.7\,\mathrm{mK}$ and a trap frequency along the x-axis of $\omega_x = 2\pi \cdot 535\,\mathrm{kHz}$. This result agrees[2] with a measured value of $\omega_x = 2\pi \cdot 531(2)\,\mathrm{kHz}$ (see Chapter 4.4).

The potential along the z-axis can be treated analogously. For the majority of experiments that are described in the subsequent chapters, the intracavity trap (with a waist of $w_{772} = 29.6\,\mu\mathrm{m}$) was operated at a power of $P_{772} = 6.5\,\mu\mathrm{W}$ measured behind the outcoupling mirror[3] that has a transmission of $T_{\mathrm{OC}} = 101\,\mathrm{ppm}$. With the calculated ground state polarizability $\alpha^{(s)}_{772} = -11989\,\mathrm{a.u.}$, the expected potential height was $U_{g,772} = h \cdot 10.6\,\mathrm{MHz} = k_B \cdot 0.51\,\mathrm{mK}$ with a trap frequency of $\omega_z = 2\pi \cdot 404\,\mathrm{kHz}$. This value is inconsistent with the measured value (see Chapter 4.3) of $\omega_z = 429\,\mathrm{kHz}$. The source of the discrepancy can probably be found in the power calibration that was performed with a power meter of unknown accuracy and which relies on precise knowledge of T_{OC} (see chapter 2.2).

Along the y-axis, the mechanical potential is given by the Gaussian envelope of the 1064 nm standing-wave beam

$$U_{g,1064}(y, x = z = 0) = -\frac{1}{4}\left(\frac{16\,P_{1064}\,\eta}{\pi\,c\epsilon_0\,w^2_{1064}}\right)\alpha^{(s)}_{1064} e^{-2y^2/w^2_{1064}}. \tag{4.4}$$

Harmonic approximation yields a trap frequency of

$$\omega_y = \sqrt{\frac{16 P_{1064}\eta\alpha^{(s)}_{1064}}{\pi\epsilon_0 w^4_{1064} m}}. \tag{4.5}$$

[2]The crucial value η was measured in situ through spectroscopy of the AC Stark shifts. As the AC Stark shifts are not sensitive to the beam geometry, deviations in the experimentally found trap-frequency from the theoretical prediction can be expected when the standing-wave is not fully modulated.

[3]Although terms like cavity enhanced power or circulating power are widely used, the power going through the cavity differs from the power measured behind the cavity due to scattering losses alone. This apparent paradox is resolved by the fact that the electric and magnetic field of a standing-wave light field are out of phase, whereas they are in phase for a propagating light field. Thus, the Poynting vector reverses its sign during one optical period in the case of a standing wave. A fully modulated standing wave has exactly zero intensity which does not contradict the maintenance of large electric field.

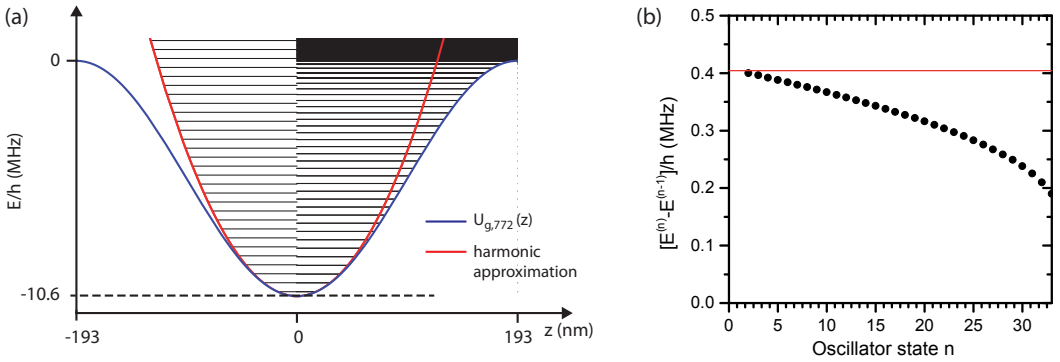

Figure 4.1.: Energy eigenstates of the sinusoidal trapping potential (a) The potential (blue line) generated by the intracavity trap at a power of $P_{772} = 6.5\,\mu\mathrm{W}$ and its harmonic approximation (red line). The black lines on the left side indicate the energy eigenstates $E^{(n)} = (n + 1/2)\omega_z$, $\omega_z = 2\pi \cdot 404\,\mathrm{kHz}$ found in harmonic approximation. The black lines on the right side indicate the energy bands found with an exact one-dimensional band-structure calculation. (b) Spacing $E^{(n)} - E^{(n-1)}$ between consecutive energy eigenstates. The black dots are calculated using the center of mass energy of the (very flat) energy bands and the red line indicates the constant spacing that is found in harmonic approximation.

For $P_{1064} = 1.25\,\mathrm{W}$, this results in $\omega_y = 2\pi \cdot 8\,\mathrm{kHz} \ll \omega_x, \omega_z$.

The actual mechanical energy eigenvalues of the sinusoidal trapping potential can be determined by performing a 1D lattice calculation (see Appendix B). The results will generally be energy bands that are parametrized by a continuous quasi-momentum q and an integer band index n. For deep lattices $U(\mathbf{0})/\hbar \gg \omega$, the bands become flat in the sense that the energy eigenvalues within one band are degenerate in q. Energy eigenstates will be spatially delocalized over the entire lattice. In the case of deep lattices, tunneling rates between neighbouring sites will be low, such that long-lived spatially localized superposition states can be generated within the flat energy bands. These approximate the oscillator eigenstates. Figure 4.1(a) shows the trapping potential along the z-axis, generated by the intracavity trap for $P_{772} = 6.5\,\mu\mathrm{W}$ (blue line) together with the harmonic approximation (red line). On the left side of the graph, the discrete oscillator eigenstates of the harmonic approximation are shown and form a ladder of states with uniform spacing $E_n - E_{n-1} = \hbar\omega = h \cdot 404\,\mathrm{kHz}$. On the right side, the exactly calculated energy band are indicated by black regions that span vertically from the lower to the upper band edge. The bands are almost flat until close to the edge of the potential barrier. Panel (b) shows the spacing of adjacent energy eigenstates for all 33 trapped states. The red line indicates the constant spacing of 404 kHz, which is valid for harmonic approximation. The values are well described by $\Delta E = h \cdot (404 - 4\,n)\,\mathrm{kHz}$ for $n \leq 20$. This anharmonicity of the trapping potential results in a state-dependent transition frequency for two-photon Raman transitions and microwave transitions between

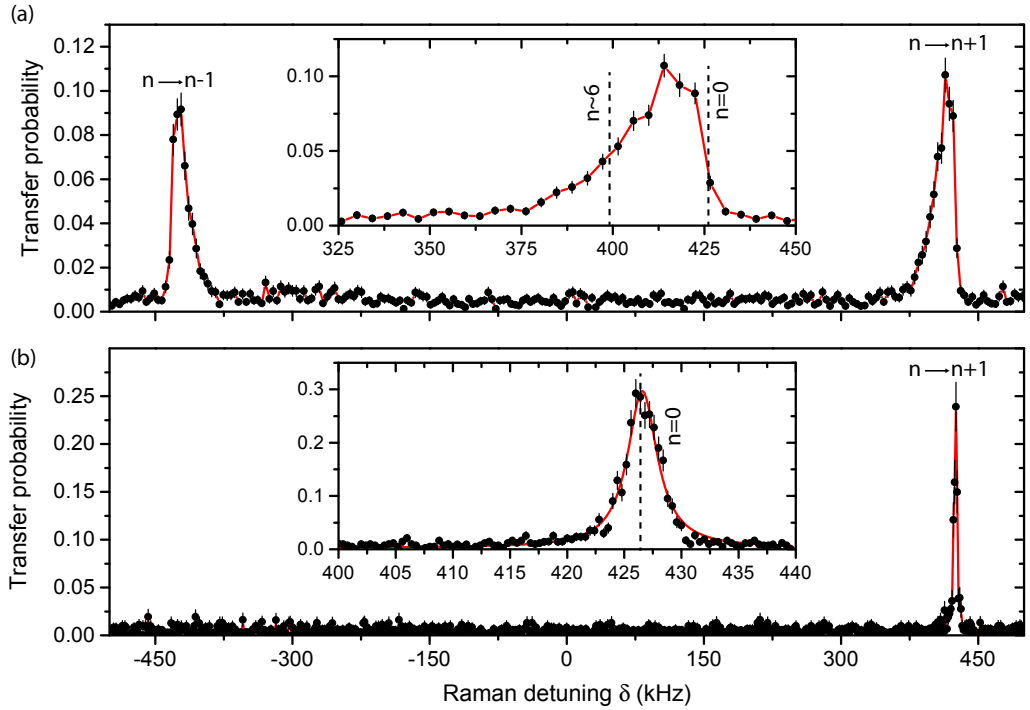

Figure 4.2.: Raman sideband spectroscopy (a) Raman spectrum recorded after Sisyphus cooling. The inset shows a close-up of the asymmetrically broadened blue sideband. The red line serves as a guide to the eye. (b) Raman spectrum recorded after sideband cooling. The inset shows the results of an additional high-resolution scan of the blue sideband. The red line is a single Lorentzian fit to the data. Note the different scales of the x-axis of the two insets.

the hyperfine ground states. As an experimental consequence, an asymmetric line broadening is observed (see the following chapter).

4.3. Raman Spectroscopy and Ground-State Cooling

As discussed in Chapter 2.6, stimulated Raman transitions driven by the trapping light in combination with a running-wave beam can be used to drive transitions between mechanical states. Figure 4.2(a) shows the result of a spectroscopical measurement that was performed by preparing the atom in the $|F = 1, m_F = 0\rangle$ internal spin state, attempting Raman transfer for a duration of $T = 300\,\mu$s, and finally checking for population in the F=2 ground state. The intracavity trap was set to a power of $P_{772} = 6.5\,\mu$W measured behind the output-coupling mirror, and the running-wave Raman beam propagating along the x-axis (see Chapter 2.6) was set to a power of $1\,\mu$W. Two transfer reso-

nances are visible that correspond to the ascending ($\Delta n = +1$) and descending ($\Delta n = -1$) motional sideband. The carrier that corresponds to $\Delta n = 0$ is completely suppressed, as expected from theory (see Chapter 2.6). Both peaks have widths that by far outnumber the minimum possible width of 3 kHz given by the probing duration. The broadening of both lines is asymmetric with a moderate slope towards zero detuning and a steep edge at a well-defined maximum (positive and negative) detuning. This broadening is a consequence of the anharmonicity of the trapping potential as discussed in Chapter 4.2. For the parameters of the experiment, the spacing between neighbouring mechanical energy eigenstates decreases by 4 kHz per energy eigenstate. The Raman transfer lines to the next lower and higher states correspondingly appear shifted inwards. The inset in Fig. 4.2(a) shows a close-up of the blue detuned Raman line. The line is broadened by approximately 25 kHz, which corresponds to significant atomic population up to the 6^{th} mechanically excited state.

Numerical evaluation of such asymmetrically broadened transition lines (see Chapter 3.3 and reference [121]) can in principle serve as a thermometry technique. A more elaborate technique that enables the measurement of atomic population in individual mechanical states is discussed in Chapter 5; a numerical evaluation of the Raman line shapes will therefore not be discussed here.

Unitary manipulations are reversible, and as such they can never remove entropy from an initial mixed thermal state. If prior knowledge about the state exists, for example if the atom is prepared in the $|F = 2, m_F = 0, n = 2\rangle$ mechanical Fock state, a π-pulse on the $|F = 2, m_F = 0, n = 2\rangle \leftrightarrow |F = 1, m_F = 0, n = 1\rangle$ transition at a two-photon detuning $\delta f > E_{21}/h$ below the bare hyperfine-transition frequency, followed by a π-pulse on the $|F = 1, m_F = 0, n = 1\rangle \leftrightarrow |F = 2, m_F = 0, n = 0\rangle$ transition at a two-photon detuning $\delta f < E_{21}/h$ above the hyperfine-transition can bring the atom to the motional ground state. However, if this same sequence is applied to an atom that is already in the ground state $|F = 2, m_F = 0, n = 0\rangle$ initially, the atom will be brought to $|F = 1, m_F = 0, n = 1\rangle$, an excited motional state. This problem can be counteracted by introducing an incoherent process that carries entropy into the environment. In the discussed scheme, this is achieved by optically repumping the spin-degree of freedom after performing a π-pulse on the Raman sideband, descending a motional quantum on a given transition.

To perform ground-state cooling, transfer on the descending motional sideband $|F = 1, m_F = 0, n\rangle \leftrightarrow |F = 2, m_F = 0, n - 1\rangle$ is alternated with optical pumping of the atom back to $|F = 1, m_F = 0\rangle$ [81,83,85,122]. In the Lamb-Dicke regime, where the mechanical extent of the atomic wave function is small compared to the wavelength of the radiated light, the optical pumping is expected to leave the mechanical state unperturbed, such that per cycle one motional quantum can be removed from the system. Once, the state $|F = 1, m_F = 0, n = 0\rangle$ is reached, the atom is rendered dark with respect to excitation by this sequence. Figure 4.2(b) shows a Raman spectrum that was taken with the same parameters as the spectrum in panel (a), but after 21 periods of Raman side-

band cooling. During these 21 periods, the Raman coupling was permanently switched on and optical pumping sequences to $|F = 1, m_F = 0\rangle$ were generated with a periodicity that was approximately equal to the duration of a π-pulse of the Raman coupling.

In contrast to the spectrum recorded in the thermal case, only a single transition line corresponding to the ascending motional (blue detuned) sideband is visible. Consistent with theoretical expectation, the asymmetry of the single transfer line vanished as well. The inset shows a separate dataset with higher resolution. The red line is a Lorentzian fit with a full width at a half maximum of 3(2) kHz, which is compatible with the theoretical expectation of a single Fourier-limited transition line. The line center is found at 425.58(3) kHz. Independent measurements (see Chapter 5.2) indicated that the differential AC Stark shift of the two hyperfine ground states shifts their splitting $\Delta_{\mathrm{HF}}/\hbar$ by 3 kHz towards smaller frequencies. In fact, the two well-defined, high-frequency edges of the lines in Fig. 4.2(a) are symmetric around -3 kHz. The actual detuning of the motional sideband from the carrier frequency and therefore the trap frequency is $\omega_z = 428.58(3)$ kHz. The quoted error is purely statistical.

4.4. Eigenmotions in Non-Orthogonal Lattices

4.4.1. Theory

The two standing-wave beams that form the optical lattice in the cavity do not intersect in a perfect orthogonal manner. A deviation of $\beta = 27.0(3) \cdot 10^{-3}$ rad was identified by evaluating fluorescence images of trapped atom pairs (see Chapter 2.4). Thus, the pattern of the possible trapping sites in the skewed lattice will deviate from a rectangular checkerboard pattern. Besides this influence on the geometry of the whole lattice, a second, non-trivial consequence of the non-orthogonality appears in the geometry of each individual trapping site. In this chapter, only two-dimensional effects that occur in the xz-plane are discussed. The weak confinement along the y-axis is neglected and is not expected to influence the motional dynamics in the xz-plane.

A sketch of the trapping geometry is shown in Fig. 4.3. The blue-detuned intracavity trap at a wavelength of 772 nm is aligned with the z-axis and generates a sinusoidal optical potential with maximum height of $U_z = {}^1\!/_4 \alpha_{772} E_{772}^2$, where α_{772} is the dynamic polarizability of the ground state at the trap wavelength and E_{772} is the amplitude of the standing wave's electric field. The transversal, red-detuned trap generates an attractive potential with a maximum height $|U_x| = {}^1\!/_4 \alpha_{1064} E_{1064}^2$. In this discussion, the non-constant beam-envelopes are ignored as their typical length scale $z_0 \gg \lambda$ is large compared to the modulation of the potential due to the standing-wave structure. While they are thus unimportant for the consideration of a single trapping site, they will be important in

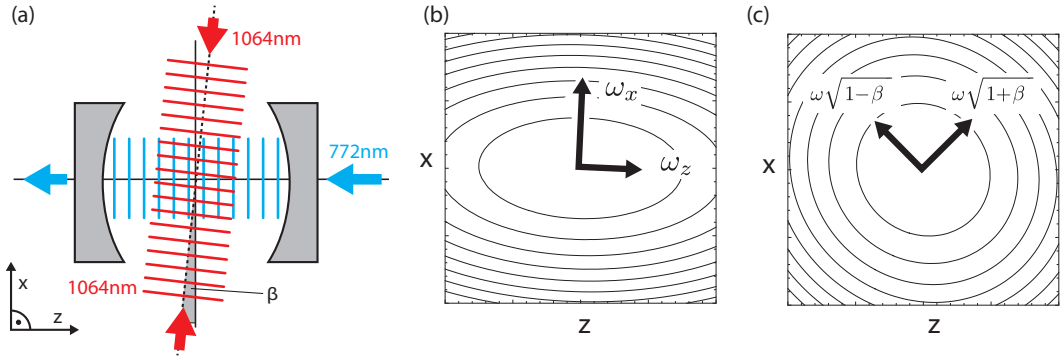

Figure 4.3.: Eigenmotions in a non-orthogonal lattice (a) Sketch of the trapping geometry. The intersection angle of the two standing-wave beams deviates by $\beta = 27.0(3) \cdot 10^{-3}$ rad from orthogonality. (b) Lines of constant potential $U(\vec{r})$ in the case of non-degenerate trap frequencies $\omega_x \gg \omega_z$. The arrows mark the orientation of the eigenmotions, which are well aligned with the coordinate axes. (c) The equipotential lines in the case of degenerate trap frequencies $\omega_x = \omega_z = \omega$. Owing to $\beta \neq 0$, the equipotential lines deviate from circular symmetry and two distinct eigenmotions are formed along the diagonal directions with non-degenerate trap frequencies.

the next chapter. The total trapping potential can be denoted by:

$$U(\vec{r}) = U_z \sin(\vec{k_z} \cdot \vec{r})^2 + U_x \sin(\vec{k_x} \cdot \vec{r})^2 \tag{4.6}$$

The two lattice axes are given by $\vec{k_z} = 2\pi/772\,\mathrm{nm} \cdot \hat{e}_z$, and $\vec{k_x} = 2\pi/1064\,\mathrm{nm} \cdot (\sin(\beta)\hat{e}_z + \cos(\beta)\hat{e}_x)$. With this definition, the potential vanishes at the origin and a two-dimensional Taylor expansion consists of only four quadratic terms:

$$U(\vec{r}) = \frac{1}{2} \sum_{(i,j)\in\{x,z\}} r_i r_j H_{i,j} + \mathcal{O}(|r|^3), \tag{4.7}$$

where $H_{i,j} = \partial^2 U(\vec{r})/\partial r_i r_j$ is the Hessian matrix of the potential evaluated at the origin. With m being the mass of the trapped atom, the trap frequencies of the harmonically approximated individual one-dimensional lattices are $\omega_i = \sqrt{2U_i/m}\,|k_i|$. In terms of these trap frequencies the Hessian matrix can be expressed as:

$$H = m \begin{pmatrix} \omega_z^2 + \omega_x^2 \sin(\beta)^2 & \omega_x^2 \sin(\beta)\cos(\beta) \\ \omega_x^2 \sin(\beta)\cos(\beta) & \omega_x^2 \cos(\beta)^2 \end{pmatrix}. \tag{4.8}$$

Independent of the angle β, the quadratically approximated potential factorizes into two one-dimensional harmonic oscillators along directions that are eigenaxes of the Hessian matrix with oscillator frequencies given by the corresponding eigenvalues. Diagonalisation of equation 4.8 yields the following trap

frequencies:

$$\omega_{\pm}^2 = \frac{1}{2}\left((\omega_x^2 + \omega_z^2 \pm \sqrt{\omega_x^4 + \omega_z^4 - 2\omega_x^2\omega_z^2(2\cos(\beta) - 1)}\right) \tag{4.9}$$

Several cases can be distinguished:

- $\boldsymbol{\beta = 0, \omega_x \neq \omega_z}$: The eigenaxes coincide with the coordinate axes and the trap frequencies along the x- and the z-axis are identical to the individual 1D-lattices' trap frequencies, ω_x and ω_z respectively.

- $\boldsymbol{\beta = 0, \omega_x = \omega_z}$: The Hessian matrix is proportional to the identity matrix and the potential has cylindrical symmetry. The eigenvalues are degenerate and no preferred directions can be identified. The trajectory of a classical particle that is launched from the coordinate origin into an arbitrary direction will not leave the one-dimensional space spanned by this direction.

- $\boldsymbol{\beta \neq 0, \omega_x \gg \omega_z}$: For a large mismatch of the trap frequencies, the eigenaxes will remain almost perfectly aligned with the coordinate axes. The potential landscape of a single trapping site in this case is sketched in Fig. 4.3(b). The trap frequencies also remain almost unperturbed.

- $\boldsymbol{\beta \neq 0, \omega_x = \omega_z = \omega}$: For a small angle β, the Hessian matrix can be approximated as the sum of a diagonal matrix $\omega^2 \cdot \mathbb{1}$ and a symmetric, purely off-diagonal matrix $\omega^2\beta\sigma_x$ (with the Pauli matrix σ_x). The eigenaxes are consequently found along the diagonal directions $(\hat{e_x} \pm \hat{e_z})/\sqrt{2}$, independent of the size of β. The trap frequencies can be approximated to $\omega_{\pm} \approx \omega(1 \pm \beta)$. The potential landscape is shown in Fig. 4.3(c). While the equipotential lines form circles for $\beta = 0$, they deviate from cylindrical symmetry for $\beta \neq 0$ and preferred directions[4] along the diagonals are found.

By tuning the depth of the two traps, the ratio of their trap frequencies can be influenced. Figure 4.4(a) shows simulated eigenenergies $E_{n_+,n_-}(P_z) = (n_+ + 1/2)\omega_+(P_z) + (n_- + 1/2)\omega_-(P_z)$ as a function of depth of the lattice along the z-axis, which is parametrized by the optical power P_z in the standing wave. The units of P_z are chosen such that the two traps' frequencies are degenerate for $P_z = 1$ and therefore absorb all of the effects of geometry and the atomic properties. An avoided-crossing structure is found in the simulated values for $\beta = 0.1$ (red solid lines), which is not present in the uncoupled case $\beta = 0$ (black dotted lines).

[4] "Preferred directions" in the sense that an atom launched into these directions will never deviate from a line spanned out of the origin along these directions. Into all other directions, complex motional patterns will be formed that reflect the slow exchange of kinetic energy from one eigenmotion into the other and back.

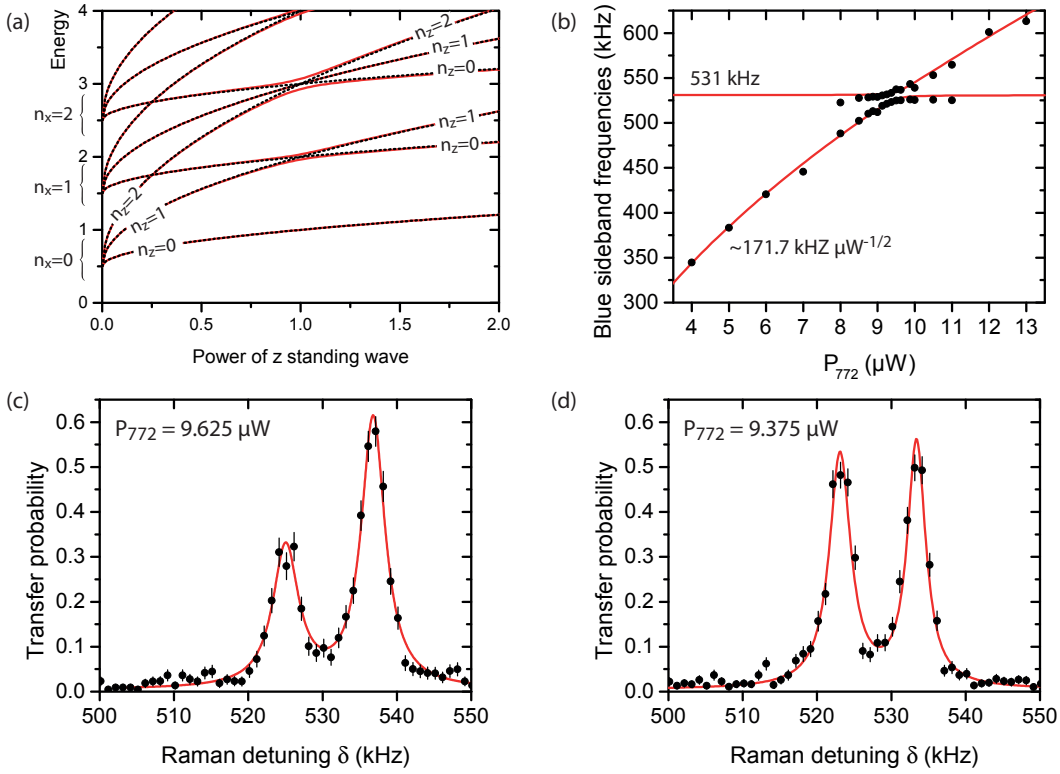

Figure 4.4.: Mechanical energy eigenstates in a non-orthogonal lattice (a) Energies $E = (n_+ + 1/2)\hbar\omega_+ + (n_- + 1/2)\hbar\omega_-$ as a function of the power P_z applied to the trap along the z-axis calculated for $\beta = 0.1$ (red lines) and $\beta = 0$ (black dotted lines). The units of power are chosen such that $P_z = 1$ leads to a trap frequency in the bare standing wave along z, which is identical to the one along x ($\omega_x = \omega_z = 1$). (b) Position of the transfer resonances on the blue sideband as a function of the power of the intracavity trap (observed behind the outcoupling mirror). The red line was a calculated using equation 4.9 with parameters $\omega_x = 531(2)\,\mathrm{kHz}$, $\omega_z/\sqrt{P_z} = 2\pi \cdot 171.0(5)\,\mathrm{kHz}(\mu\mathrm{W})^{-1/2}$, and $\beta = 22(10) \cdot 10^{-3}\,\mathrm{rad}$ that were found by fitting to the data. (c) Single spectrum of the blue sideband region recorded at $P_{x,1064} = 1.4\,\mathrm{W}$ and $P_{z,772} = 9.625\,\mu\mathrm{W}$. (d) Single spectrum recorded for $P_{x,1064} = 1.4\,\mathrm{W}$ and $P_{z,772} = 9.375\,\mu\mathrm{W}$. The red line in both spectra are double Lorentzian fits to the data.

4.4.2. Raman Spectroscopy of Motional Coupling

The avoided crossing of the trap frequencies can be measured through Raman sideband spectroscopy of the blue sideband for different settings of P_{772}, the blue intracavity trap's power, which changes the ratio of the trap frequencies. To avoid the asymmetric broadening of transition lines that was discussed in the previous chapter, spectroscopical interrogation with a weak probe pulse was preceded by 21 periods of Raman sideband cooling, as described in Chapter 4.3. The frequency of the red-sideband pulses that were used for cooling was

determined for each setting of P_{772} from an initial spectrum that was recorded for a thermal state. Raman cooling followed by an optical pumping sequence prepared the atom in $|5S_{1/2}, F = 1, m_F = 0\rangle$. Raman interrogation (see Chapter 2.6) was then performed for 300 μs followed by hyperfine-state detection (see Chapter 2.5.1).

Figure 4.4(b) shows the positions of the transfer lines that were found by fitting double Lorentzians to the individually recorded spectra (see Panels (c) and (d) for example spectra). The power of the 1064 nm trap was held constant at $P_{1064} = 1.4\,\mathrm{W}$. The red line is a fit of equation 4.9 to the data. An x-trap frequency of $\omega_x = 2\pi \cdot 531(2)\,\mathrm{kHz}$ was found, that is consistent with the theoretical value $\omega_x = 535\,\mathrm{kHz}$ (see Chapter 4.2).

For trap powers $P_z < 8\,\mu\mathrm{W}$ and $P_z > 11\,\mu\mathrm{W}$, the position of the single observed transfer resonance is well described by the square-root dependency $\omega_z(P_z) = 2\pi \cdot 171.0(5)\,\mathrm{kHz}/\sqrt{\mu\mathrm{W}}\,\sqrt{P_z}$. In this regime, the eigenmotions are aligned with the x- and z-axis and only the eigenmotion along the z-axis can be driven with the used Raman geometry (see chapter 2.6). As P_z approaches the value 9.375 μW, the eigenmotions start to bend away from the coordinate axis. Both eigenmotions now have a non-zero projection onto the z-axis and thus can be addressed by the Raman fields. For $8\,\mu\mathrm{W} < P_z < 11\,\mu\mathrm{W}$, two transfer resonances are observable, and their positions form an avoided crossing.

Figure 4.4(c) shows the blue-sideband part of a single spectrum recorded for $P_{772} = 9.375\,\mu\mathrm{W}$ intracavity-trap power. Two well-separated transfer resonances of approximately equal strength are clearly discriminable. These correspond to the diagonally aligned eigenmotions with equal projections onto the z-axis. Figure 4.4(d) shows another spectrum recorded for a greater intracavity power of $P_{772} = 9.625\,\mu\mathrm{W}$. Again, two transfer resonances can clearly be discriminated. But in contrast to the data shown in panel (c), the two lines are not equally strong. The line with the greater frequency corresponds to an eigenmotion that has a greater projection onto the z-axis and correspondingly a greater matrix element and Rabi frequency. The weaker line corresponds to the orthogonal eigenmotion, which for even greater P_{772} will align with the x-axis and correspondingly not be visible in the spectrum any longer.

This effect has been mentioned in the literature before only in the context of ultracold quantum gases [120] where it was observed by adiabatically tuning through the avoided crossing and observing the corresponding transfer of excitation in time-of-flight imaging. The data presented here constitute the first spectroscopic observation of a motional coupling in an optical lattice that is caused by lattice non-orthogonality.

4.4.3. Observation of Stable Trapping Regions

In the previous chapter, the consequences of the deviation of the lattice geometry from perfect orthogonality for the orientation of a single trapping site's eigenmotions were discussed. When tuning the system to degenerate trap fre-

quencies, the new eigenmotions will be diagonally oriented and will both have non-zero projections onto the z-axis, along which the Raman beams can couple to motional states. In this situation, two-dimensional Raman cooling is possible in a geometry that would otherwise permit only one-directional cooling.

Experimental results have demonstrated that this is also true for optical molasses cooling. The cooling beam is impinged at 45° within the xy-plane (see Chapter 2.1) in a lin-⊥-lin polarization configuration. Optical molasses cooling relies on a Sisyphus effect that is generated in the polarization lattice of the cooling light [123]. Thus, this method can only cool motion that occurs along the direction of the polarization gradient. In the experimental apparatus these are the x- and y- directions. For a setting of the trap frequencies' ratio $\omega_x/\omega_z \neq 1$, one of the potential's eigenmotions will be aligned with the z-axis and will therefore remain uncooled.

Owing to the Gaussian envelope of the beams that generate the two-dimensional lattice, the ratio of trap frequencies ω_x/ω_z along the x- and z- direction in one trapping site depends on where the particular lattice site is located within the intersection region. Figure 4.5(a) shows the relevant geometry. The intensities of both intersecting standing-wave beams have a Gaussian envelope transversally to the respective beam axis. Correspondingly, the trap frequency along a particular beam for a given site will be smaller the further away the site is from the beam axis. Trapping sites with identical trap frequencies along both individual standing-wave beams are generally located on hyperbolas. These merge into a cross when the trap parameters are chosen such that the two trap frequencies ω_x and ω_z for motion along each beam found at a site centered within this beam are degenerate. The eigenmotions within the xz-plane are oriented along the diagonal directions for these sites. The Sisyphus cooling scheme is expected to be more effective for these sites, as all three motional eigenaxes (including the weakly confined motion along y) have a finite projection onto the direction of the optical molasses' polarization gradient.

The cooling performance influences the steady-state temperature of an atom at a given site. For atoms that are not trapped at sites located on the described hyperbolas, the optical molasses cools only the motion along the x- and y-axis and consequently high temperatures of the motion along the z-axis are expected. Atomic temperatures that are comparable with the lattice depth of typically 1 mK along the z-axis will quickly lead to loss of an atom from the trapping site. The discussed patterns should therefore be observable by recording the position-resolved lifetime of the atoms in the trap.

Panels (b)-(d) show superimposed images of loaded atoms for different settings of the intracavity trap power $P_{772} = 7.6,\ 5.7,\ 10\,\mu$W respectively. After loading a random number of atoms from the MOT, ten images were taken; each image typically showed up to five well localized atoms (similar to the images in Chapter 2.4). Several thousand of these images were then added, such that a great pixel value in the resulting images corresponds to having seen a single atom at this particular location in many images compared to not having seen atoms very

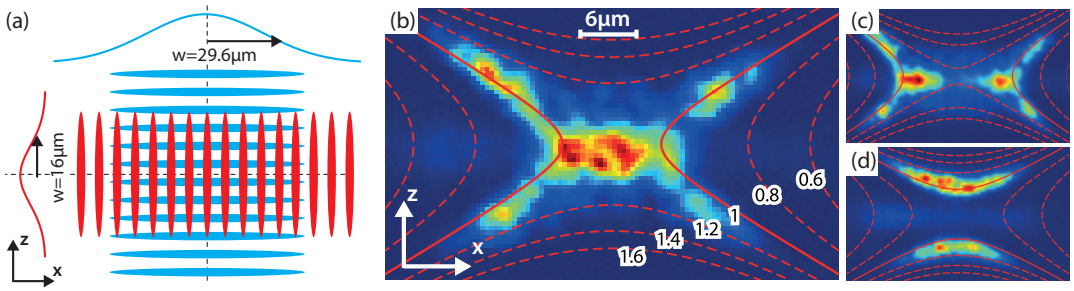

Figure 4.5.: Formation of stable trapping regions (a) The two intersecting standing-wave beams that create the two-dimensional lattice have Gaussian envelopes. The ratio of an individual trapping site's trap frequencies ω_x and ω_z therefore depends on the location of the site in the intersection region. (b) Atom distribution averaged over many experimental repetitions for $P_{772} = 7.6\,\mu$W and $P_{1064} = 0.88\,$W. The red lines indicate spatial regions of identical ratio ω_z/ω_x. The solid line indicates $\omega_z/\omega_x = 1$. (c) The same experiment for $P_{772} = 5.68\,\mu$W (d) The same experiment for $P_{772} = 10\,\mu$W.

often in the dark regions. The power of the 1064 nm trap was held constant at $P_{1064} = 0.88\,$W. Based on the spectroscopy presented in Chapter 4.4.2, identical trap frequencies along the two beams individually should thus be reached for a intracavity trap power of $P_{772} = 6.7\,\mu$W. The red lines indicate regions of identical ratio of the two trap frequencies ω_z/ω_x with the solid line denoting $\omega_x = \omega_z$.

- The trap frequencies in the center of the intersection region are almost identical in panel (a) and the long-lived atoms form a star-like pattern that is slightly elongated along the x-axis.
- Panel (c) shows a situation where $\omega_z \gg \omega_x$. The atoms are predominantly found to the left and the right of the center where the intracavity trap has decayed from its maximum value and the trap frequency along the cavity direction has become identical to the trap frequency along the 1064 nm standing-wave beam.
- The opposite situation $\omega_z \ll \omega_x$ is observed in panel (d) where the atoms are arranged along two hyperbolas above and below the trap center.

In all three images, the atoms are aligned along the independently calculated regions of degenerate trap frequencies. During data collection, one could observe how atoms that were initially trapped in an unstable region appeared at different trapping sites in consecutive images until they were transferred by chance to a site with degenerate trap frequencies. Once they had reached such a site, they seldom changed their position.

The data presented in this chapter was collected with both traps linearly polarized. It was later observed that elliptical polarization components of the

intracavity light drastically enhances performance of the optical molasses cooling. The patterns shown in Fig. 4.5 vanish and the atoms are homogeneously distributed over a region that appears to be limited by the envelope of cooling beams. This effect remains largely unexplained and offers an interesting future research possibility.

5. Detection and Manipulation of Discrete Mechanical States

5.1. Introduction

Since the first demonstration of optical dipole traps [88], the degree of control over trapped atoms has tremendously grown. To a great extent, this progress has been driven by the development of new cooling techniques. Residual thermal excitation of the motion of trapped atoms is a common source of experimental uncertainty (see Chapter 3.3.1) and cooling to the ground state of motion appears as a canonical goal. For a single trapped atom, this has recently been achieved by different groups along one spatial direction [83, 85, 124] and three-dimensionally [81, 84, 125]. In all of these cases, vanishing of the descending[1] motional sideband of either a Raman (see Chapter 2.6) or a microwave transition was used as an unambiguous signal of having reached the lowest energy state.

To date, only few publications exist, which focus on the mechanical degree of freedom of trapped neutral atoms, but do not report solely on cooling or trapping. Among these, the transient dynamics of trapped ensembles of neutral atoms in reaction to a modulation of the trapping potential was investigated [126, 127], an ensemble of atoms was prepared in the first excited motional state [128] and a scheme to manipulate the motional state through microwave transitions was reported [124, 125]. Different techniques were published to characterize motion of trapped neutral atoms. For large ensembles, ballistic expansion followed by absorption imaging [128] is a well-established technique, especially in ultracold quantum gas experiments. While this technique enables the measurement of the full momentum distribution of an ensemble, it intrinsically leads to loss of the atoms and is not applicable to small ensembles. Release and recapture techniques [129] provide an indirect measure of the momentum distribution of trapped atom, but they also inevitably lead to atom loss. Evaluating the line-strength ratio of motional sidebands in Raman spectroscopy allows to measure the temperature of a trapped atoms [81, 84, 122, 130]. This technique is applicable to single particles, but makes a-priori assumptions about

[1] For a transition to an excited state, the descending sideband is red detuned from the transition frequency. For stimulated transitions to energetically lower states, the descending sideband appears at a higher frequency and therefore may appear as the blue detuned sideband.

the population distribution over motional states that cannot be verified. It thus subsumes the complex mechanical degree of freedom in a single number, namely the temperature, describing a statistical ensemble quantity. Recently, a thermometry technique was reported that is based on evaluating asymmetrically broadened transition lines in state-dependent potentials [121]. While this technique is, in principle, applicable to single particles, it also makes assumptions about an energy distribution that are difficult to verify.

This is in striking contrast to trapped-ion systems, in which extensive use is made of the motional degrees of freedom [122]. Here, the applications span from fundamental topics like the generation of Schrödinger cat states [131] to applied topics in quantum simulation [132] and quantum information processing [133].

Applications for neutral atoms do exist. Theoretical papers have proposed the use of the huge Hilbert space of harmonic oscillators for applications in quantum information processing [134–136] and optomechanics [137, 138].

In addition to ground-state cooling (see Chapter 4.3) as the initialization of a well-defined motional state, the coherent manipulation and readout of the motional state are important prerequisites for the realization of these protocols. This chapter reports an experimental technique for measuring the population of individual mechanical energy eigenstates of optically trapped atoms. An outstanding property of this technique is that it does not lead to atom loss or alteration of the detected motional state, aside from the unavoidable quantum projection, and is applicable to single atoms. As a measurement tool it transcends established thermometry techniques in that it does not make a-priori assumptions about an energy distribution and does not require calibration. The theoretical background is discussed in Chapter 5.2. Experimental results on the characterization of motional states are presented in Chapter 5.3.1. To this end, the technique was applied to the motional state found after Sisyphus cooling, and states found after Sisyphus cooling followed by additional Raman sideband cooling. Chapter 5.3.2 discusses the preparation of a singly excited motional Fock state, using coherent Raman sideband manipulation of the motional state. Further, modulation of the trapping potential's depth is used as a method to directly manipulate the motional state. Results are presented in Chapter 5.3.3. Parametric excitation of the motional ground state results in a state that is well described by the phonon distribution of a squeezed motional vacuum state.

An overview over future research opportunities that are enabled by this technique concludes this chapter.

5.2. Theory

The discussed technique relies on generating elliptical polarization components of the intracavity trap[2]. The polarization of the trapping light is described by

[2]This is only possible because the cavity is non-birefringent and therefore provides two degenerate, orthogonally polarized modes.

the complex polarization vector $\hat{\epsilon}$ with $\epsilon_z = 0$. When the light is elliptical, $\Im(\epsilon_x^* \epsilon_y) \neq 0$, a vector light shift is generated (see Chapter 3.2) and the energy shift of the hyperfine ground states $|5S_{1/2}, F, m_F\rangle$ caused by the AC Stark shift will be given by

$$\Delta E^{\mathrm{ACS}}_{F,m_F} = \frac{-|E|^2}{4}\left[\alpha^{(s)} - \alpha^{(v)}\Im(\epsilon_x^*\epsilon_y)\frac{m_F}{F}\right], \tag{5.1}$$

where $\alpha^{(s)}$ and $\alpha^{(v)}$ are the scalar and vector polarizabilities (see Chapter 3.2). The relative AC Stark shifts between different m_F states will be small compared to the hyperfine splitting $\Delta_{\mathrm{HF}} = 6.835\,\mathrm{GHz}$ of the two ground states. It can therefore be assumed that hyperfine breakdown does not play a significant role, and the hyperfine states thus remain valid energy eigenstates. The scalar $\alpha^{(s)}_{772.37\,\mathrm{nm}} = -11989\,\mathrm{a.u.}$ and vector $\alpha^{(v)}_{772.37\,\mathrm{nm}} = -6689\,\mathrm{a.u.}$ polarizabilities for the relevant wavelength $\lambda = 772.37\,\mathrm{nm}$ were previously calculated.

As long as the light is not completely circularly polarized, it causes a $\Delta m_F = \pm 2$ coupling between Zeeman states of one hyperfine-spin manifold. The actual energy eigenstates will therefore deviate from the $|F, m_F\rangle$ states (that are defined with the quantization axis chosen along the z-axis). To prevent this from occuring, a magnetic field $\vec{B} = B\hat{e}_z$ is applied along the z-axis that lifts degeneracy of the $|F, m_F\rangle$ states. The shift of Zeeman states caused by the magnetic field is $\Delta E^B_{F,m_F} = \mu_B\, g_F\, m_F\, B$, where μ_B is the Bohr magneton and g_F is the Landé factor of the particular hyperfine spin. If the Zeeman splitting, $\Delta E^B_{F,m_F} \gg \frac{1}{4}\alpha^{(v)}|E|^2\Im(\epsilon_x^*\epsilon_y)/F$, dominates the scale of the vector light shifts, the effects of off-diagonal elements in the AC Stark shifting Hamiltonian can be ignored.

The elliptical trapping light and the resulting m_F-dependent AC Stark shifts lead to state-dependent trap frequencies (see Chapter 4.2):

$$\omega_{F,m_F} = \sqrt{\frac{2P_{772}}{\pi\,\epsilon_0\,c\,w_{772}^2 T_{\mathrm{OC}}\,m}\left(\alpha^{(s)}_{772} + \Im(\epsilon_x^*\epsilon_y)\alpha^{(v)}_{772}\frac{m_F}{F}\right)\left(\frac{4\pi}{772.37\,\mathrm{nm}}\right)^2} \tag{5.2}$$

where m is the mass of a single ^{87}Rb atom, $w_{772} = 29.6\,\mu\mathrm{m}$ is the $1/e^2$-intensity radius of the cavity mode, $T_{\mathrm{OC}} = 101\,\mathrm{ppm}$ is the transmission of the outcoupling mirror and P_{772} is the power of the intracavity trapping light measured in transmission behind the outcoupling mirror.

Figure 5.1 shows how this situation can be exploited to detect the motional state that is occupied by the single atom in a non-destructive manner. The state of the atom is denoted by $|F, m_F, n\rangle$, where F, m_F describes the internal hyperfine state and n is the mechanical state ($n = 0$ is the ground state of motion). The atom is initially optically pumped to the $|1, 0, n\rangle$ internal hyperfine state. In the next step, a microwave field is impinged that drives magnetic dipole transitions between the ground states. The wavelength of the microwave field is orders of magnitude greater than the extent of the atom's spatial wave

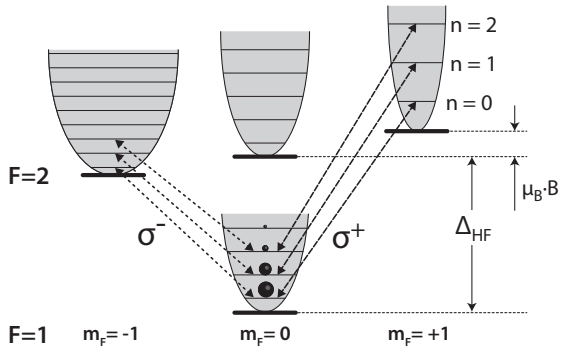

Figure 5.1.: Working principle Elliptical components of the dipole-trapping light in combination with a non-zero vector polarizability generate state-dependent trap frequencies. In this situation, the transition frequency of a magnetic dipole transtion between the two hyperfine ground states depends on the mechanical state $|n\rangle$ even for $\Delta n = 0$ transitions that can be driven with microwave radiation.

function. Therefore, the coupling between the hyperfine states can be regarded as independent of the atom's position. From the orthogonality of the mechanical wave functions then directly follows that the microwave does not couple to the atom's motional degree of freedom and that it can only drive $\Delta n = 0$ transitions[3].

The AC Stark shift of an m_F=0 state does not depend on the hyperfine spin F, even in the presence of trap ellipticity, and the mechanical states in the $|2, 0, n\rangle$ and $|1, 0, n\rangle$ manifolds are equally spaced. Microwave transitions between the F=1 and F=2 ground states with a π-polarized microwave can thus be driven resonantly at $\Delta_{\mathrm{HF}} = 6.834683\,\mathrm{GHz}$ regardless of the mechanical state. The situation changes for $\sigma^{\pm}$ polarized microwave field components. For example, σ^+-polarized fields will drive transitions $|1, 0, n\rangle \leftrightarrow |2, 1, n\rangle$. Since the trap frequency of the two states differs, the same mechanical state $|n\rangle$ will have different energy depending on the atom's internal state $|F, m_F\rangle$. The spin transitions can thus be driven at frequencies

$$f_n = \Delta_{\mathrm{HF}} + (n + 1/2) \cdot (\omega_{2,1} - \omega_{1,0})/2\pi + \mu_B\, g_{F=2}\, B/h \tag{5.3}$$

that depend on the mechanical state n. In combination with cavity-assisted hyperfine-state detection (see Chapter 2.5.1), population of a certain mechanical state can be tested in a non-destructive manner.

Figure 5.2 shows a microwave spectrum that was recorded by initializing the atom in the $|\mathrm{F}{=}1, m_F{=}0\rangle$ ground state, attempting microwave transfer for $300\,\mu$s at a given frequency and testing for atomic population in F=2. This

[3]This can be circumvented using state-dependent lattices, as was shown in a joint publication by the groups of Dieter Meschede and Poul Jessen [124]

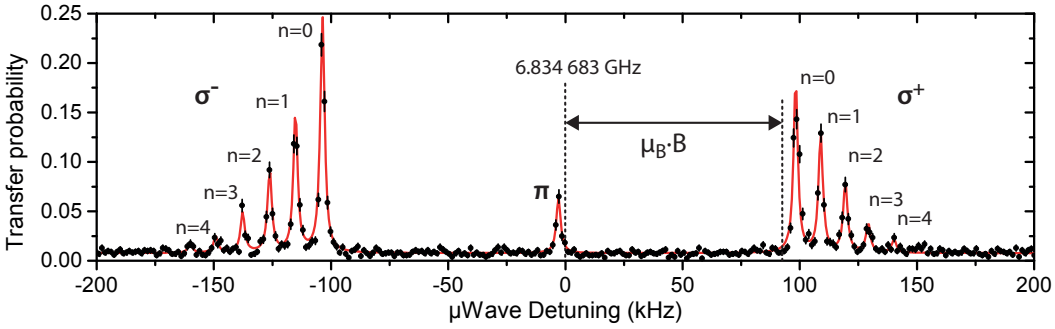

Figure 5.2.: Microwave spectroscopy in a spin-dependent lattice Microwave spectrum covering all transitions from $|\mathrm{F}{=}1,m_F{=}0\rangle$ to the F=2 ground state. The π-polarized transition appears as a single line, because the trap frequencies of the $m_F = 0$ states are identical. The σ^+ and σ^- polarized field components that lead to $\Delta m_F = \pm 1$ transitions generate well-resolved line tuples. Each of the individual lines corresponds to a single mechanical state and the line height indicates population of this state.

experiment is repeated at a rate of 1 kHz with interleaved optical molasses cooling until simultaneously exposed images indicate loss of the single atom. While repeating the experiment, the microwave frequency is repeatedly swept over the full range of the spectrum during 1 second.

The spectrum clearly separates into three parts. A single line close to zero detuning from Δ_{HF} stems from π-polarized components of the microwave. As discussed above, the frequency of the π-polarized $|1,0\rangle \leftrightarrow |2,0\rangle$ clock transfer is not influenced by the mechanical state or the presence of the magnetic field[4]. The fact that the line is slightly shifted stems from a differential AC Stark shift of the hyperfine states. In the derivation of the AC Stark shift, starting from the finestructure states as described in Chapter 3.2, this effect appears only in higher-order perturbation theory [91]. The line will always shift towards smaller transition frequencies, unless the trap wavelength falls within the 6.8 GHz in-between transitions from F=1 and F=2 to some excited states. In this case, the trap is red-detuned with respect to one state and blue-detuned and will consequently repel the two hyperfine ground states from one another.

Transitions driven by the σ^+ and σ^- polarized magnetic-field components of the microwave appear as two tuples to the left and right of the central π-polarized peak. Both tuples consist of well separated lines that correspond to individual mechanical states. The trap frequencies $\omega_{2,0} = \omega_{1,0} = 2\pi \cdot 429\,\mathrm{kHz}$ for the intracavity trap power $P_{772} = 6.5\,\mu\mathrm{W}$ were determined by Raman spectroscopy. The spacing between the mechanical lines within one tupel is 11 kHz, such that the trap frequencies of the $m_F = \pm 1$ states in the F=2 manifold are found to be $\omega_{2,1} = 2\pi \cdot 440\,\mathrm{kHz}$ and $\omega_{2,-1} = 2\pi \cdot 418\,\mathrm{kHz}$. Using equation 5.2, the ellipticity of the trap can be calculated as $\Im(\epsilon_x^* \epsilon_y) = 0.19$, which corresponds to

[4]For small magnetic fields that do not uncouple the hyperfine spin.

a polar angle of $\theta = \arcsin[2\Im(u_x^* u_y)] = 22.3°$ on the Poincaré sphere.

While the relative height of the two tuples is given by the microwave field's polarization, the relative height of individual lines within one tuple is proportional to the population in the given state. This height decreases with distance of the particular line from zero detuning in both tuples. This is consistent with the expectation of Boltzmann distributed atomic population in the energy eigenstates for an atom in a thermal state. However, as transition properties may be different for lines associated with different mechanical states, the maximum line height found for unity population probability of the corresponding mechanical state may not be identical for all lines. A numerical evaluation of the data therefore requires a model of the involved transitions to calculate state-dependent gauging factors.

During microwave interrogation, the microwave field is impinged with a constant Rabi frequency ω_R and detuning Δ from the transition frequency of the $|0\rangle \leftrightarrow |1\rangle$ transition, where $|0\rangle = |\mathrm{F}{=}1, m_F{=}0, n\rangle$ and $|1\rangle$ is one of the coupled states in the F=2 manifold. The Bloch equations, including a (phenomenological) dephasing rate γ, are

$$\frac{d}{dt}\vec{R} = \begin{pmatrix} -\gamma & \Delta & 0 \\ -\Delta & -\gamma & -\omega_R \\ 0 & \omega_R & 0 \end{pmatrix} \vec{R} \tag{5.4}$$

for the Bloch vector $\vec{R} = (\rho_{01} + \rho_{10})\hat{e}_x + i(\rho_{10} - \rho_{01})\hat{e}_y + (\rho_{11} - \rho_{00})\hat{e}_z$. In the case of vanishing dephasing $\gamma = 0$ and when initializing the system in state $|0\rangle$ ($\vec{R}(t=0) = -1\hat{e}_z$), the population of state $|1\rangle$ after driving for a duration T can be calculated analytically:

$$\rho_{11}(T) = \frac{\omega_R^2}{\omega_R^2 + \Delta^2} \sin^2\left(\frac{1}{2} T \sqrt{\Delta^2 + \omega^2}\right) \tag{5.5}$$

As the trap frequencies of the atom depend on its spin state, the mechanical wave functions of the two coupled states will not be the same, even for identical quantum number n. This will affect the Rabi frequency ω_R and thereby the population of the state $|1\rangle$. As the microwave coupling is assumed to be constant over the spatial extent of trapped atomic wave functions, the transition matrix element is proportional to the overlap integral $\langle \Psi_\omega^n | \Psi_{\omega'}^n \rangle$ of oscillator eigenstates with the same quantum number n but different frequencies.

This is a special case of a Frank-Condon factor $\langle \Psi_\omega^m | \Psi_{\omega'}^n \rangle$ of two oscillator eigenstates n and m of oscillators with different frequencies ω and ω', but identical origin. A general analytical solution is found in the literature [139, 140]. Owing to symmetry, the overlap integral will vanish unless n and m are both

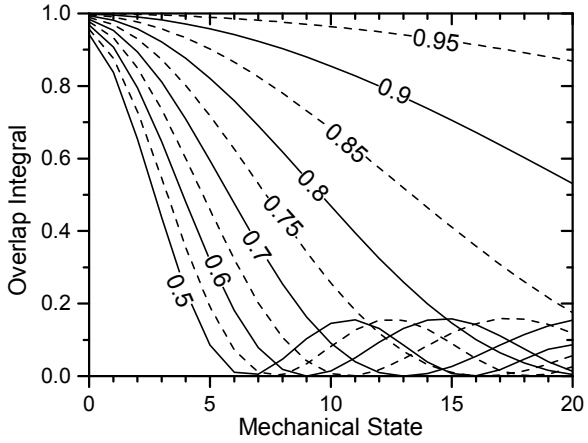

Figure 5.3.: Squared overlap integral $\langle\Psi^n_\omega|\Psi^n_{\omega'}\rangle^2$ between the same energy eigenstates of two harmonic oscillators that have different frequencies ω and ω' but identical origin. The numbers on the curves indicate the ratio of the trap frequencies ω'/ω

even or both odd. In these cases, the overlap integral is determined by:

$$\langle\Psi^m_\omega|\Psi^n_{\omega'}\rangle = \sqrt{\frac{q\,m!\,n!}{2^{m+n}}}\sum_{r=0,1}^{\min(m,n)}\frac{(2q)^r}{r!}\frac{x^{(m+n-2r)/2}(-1)^{(m-r)/2}}{[1/2(n-r)]!\,[1/2(m-r)]!}, \tag{5.6}$$

where $x = (\alpha-1)/(\alpha+1)$, $q = 2\sqrt{\alpha}/(\alpha+1)$ and $\alpha = \omega'/\omega$. The sum is calculated in increments of two from $r = 0(1)$ for even(odd) m and n. In the case of $m = n$ this equation simplifies to:

$$\langle\Psi^n_\omega|\Psi^n_{\omega'}\rangle = \sqrt{\frac{q}{4^n}}\,n!\sum_{r=0,1}^{n}\frac{(2q)^r}{r!}\frac{x^{n-r}(-1)^{(n-r)/2}}{[1/2(n-r)]!^2} \tag{5.7}$$

Figure 5.3 shows numerically calculated values of $\langle\Psi^n_\omega|\Psi^n_{\omega'}\rangle^2$ for different values of $\alpha = \omega'/\omega$. For the values extracted from the spectrum shown in Fig. 5.1(b), $\alpha = 0.975$ and the squared matrix element will deviate from 1 by less than 1 % up to 10^{th} excited state, and by less than 4 % up to $n = 20$. In this spectrum, already the fifth line is barely visible indicating almost no atomic population in higher excited state. The dependency of the ω_R on n is therefore neglected in the data evaluation.

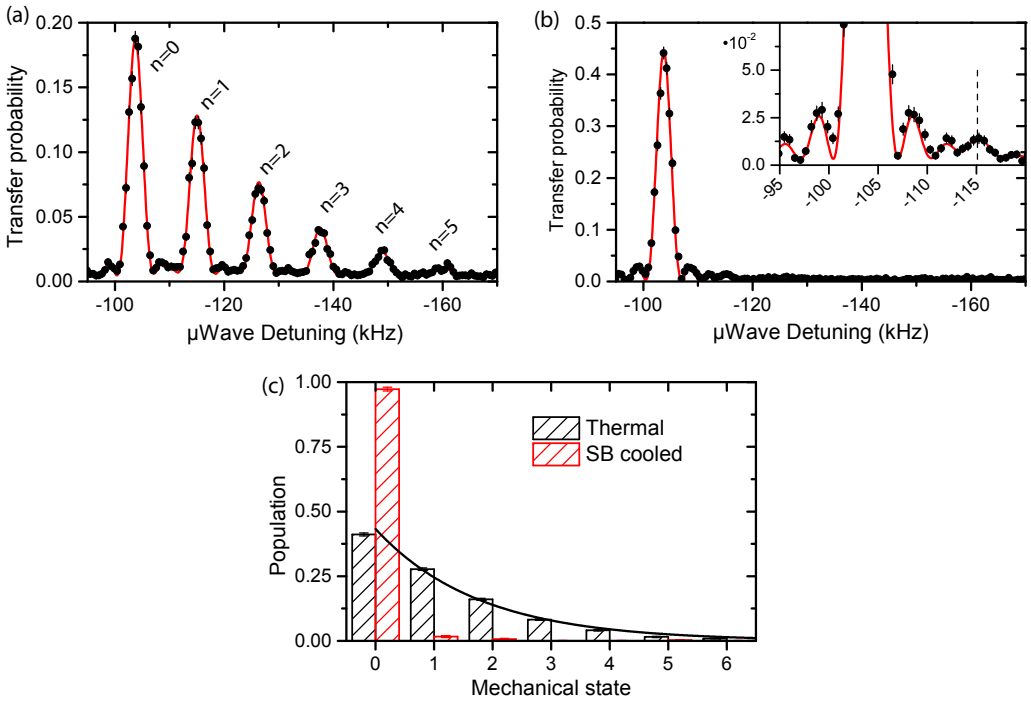

Figure 5.4.: Thermometry spectra for different mechanical states (a) Zoom onto the σ^+-polarized part of the microwave spectrum after Sisyphus cooling. The indicated errors are statistical and the red line is a fit to the data of the purely interaction-time broadened Rabi model. (b) The same part of the spectrum after cooling the single atom to its ground state of motion along the z-axis. The inset shows a zoom onto the pedestal of the single peak and the dashed line marks the transition frequency for an atom in the first mechanically excited state. (c) Population of the six lowest oscillator states found from curves fitted to the data in (a) and (b). The thermal case shown in red is well described by a Boltzmann distribution with an average number of $\langle n \rangle = 1.4$ phonons. This corresponds to a temperature of 29 μK

5.3. Experimental Results

5.3.1. Resolving Individual Oscillator States

Figure 5.4(a) shows the σ^+ part of the microwave spectrum with a higher resolution. The error bars are purely statistical and the red line is calculated by adding multiple instances of equation 5.5 with relative weighting factors and line centers found by fitting to the data. By normalizing the individual lines' height P_n to the total transfer probability, $P = \sum_n P_n$, the atomic population $\rho_{nn} = P_n/P$ of a given motional state n is found[5]. This result is intrinsically post-selected on the atom initially being in the internal $|F = 1, m_F = 0\rangle$ state,

[5]The sum is carried out only over the states shown in the graph, i.e. up to n=5.

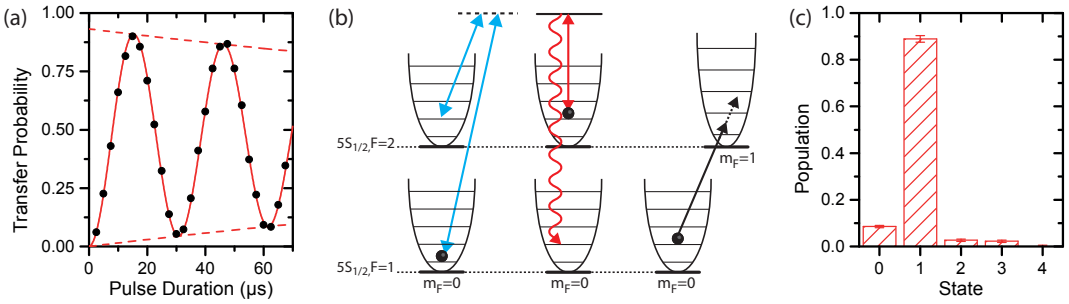

Figure 5.5.: Preparation of mechanically excited states (a) Population of the F=2 ground state as a function of the length of a Raman pulse on the blue sideband. (b) Optical pumping to $|\mathrm{F}{=}1, m_F{=}0, \mathrm{n}{=}0\rangle$ is followed by a π-pulse on the blue sideband of the $\Delta m_F{=}0$ transition. The internal state is then optically repumped to the initial state. Microwave interrogation on the σ^+-part of the spectrum and hyperfine-state detection are then used to characterize the mechanical state. (c) Population of mechanical states after the full sequence.

as otherwise no transfer can occur due to the detuning introduced by the magnetic field. The populations that are derived from the spectrum in panel (a) are displayed as red bars in panel (c). The uncertainties were calculated by Gaussian error propagation. The red line shows a Boltzmann distribution parametrized only by the average number of phonons in the system. Fitting to the data finds this value to be $\langle n \rangle = 1.4$ corresponding to a residual temperature of 29 μK.

While the data in panel (a) was recorded after Sisyphus cooling of the atom, panel (b) shows the results of an experiment that included cooling of the atom to the motional ground state (see Chapter 4.3) prior to microwave interrogation. As expected, only a single peak is found in the spectrum at the spectral position of the peak that has the highest population in the thermal case. The inset shows a close-up of the pedestal of the peak. The side lobes of the peak are reproduced by the simple Rabi model, which justifies the assumption of $\gamma = 0$ (i.e., a purely interaction-time broadened spectroscopy). Numerical evaluation of this spectrum reproduces the sum of all peak heights to within 1 % of the value found for the thermal spectrum, indicating that the atomic population in $|\mathrm{F}{=}1, m_F{=}0\rangle$ was identical in both experiments. The dashed line in the inset marks the frequency at which the n=1 line appears in the thermal spectrum. The first mechanically excited state is the only state with a significant mechanical population, asides from the ground state. Its population was 1.3(5) %.

5.3.2. Preparation of a Mechanical Fock State

Coherent Raman manipulation of the spin-mechanical state (see Chapter 2.6) in combination with optical pumping (see Chapter 2.5.2) can be used to prepare excited mechanical states. To this end, ground-state cooling of the atom is

followed by a Raman pulse on the $|F = 1, m_F = 0, n = 0\rangle \leftrightarrow |F = 2, m_F = 0, n = 1\rangle$ transition. Figure 5.5(a) shows the population in the F=2 state as a function of the duration of a Raman pulse on the blue sideband that was applied after ground-state cooling. The red line is a fit to the data of a sinusoidal oscillation that decays exponentially to half of its initial modulation depth.[6] An effective Rabi frequency of $\Omega_{\text{eff}} = 2\pi \cdot 32.4\,\text{kHz}$ and a decoherence rate of $(304\,\mu\text{s})^{-1}$ were found. The microwave spectrum in Fig. 5.4 did not show any sign of decoherence on this timescale although the driven transition is susceptible to magnetic field fluctuations. The $m_F = 0 \leftrightarrow m_F = 0$ spin-transition that is driven here is independent of the magnetic field to first order. The observed decoherence must therefore origin from the Raman lasers themselves, or from the mechanical part of the transition. The latter could be caused by intensity fluctuations of the trap. For the given decoherence rate, the achieved effective Rabi frequency is still sufficient to transfer almost 90 % of the initial atomic population into the F=2 ground state after a duration of $15.4\,\mu\text{s}$.

The Raman pulse causes a simultaneous transfer of spin and mechanical state. In order to prepare the $|5S_{1/2}, \text{F}{=}1, m_F{=}1, \text{n}{=}1\rangle$-state, a π-pulse on the ascending Raman sideband is followed by optical pumping of the spin degree back to the initial state. Ideally, the optical pumping does not affect the mechanical state. The entire sequence, including a microwave pulse for final characterization of the state is sketched in Fig. 5.5(b). Figure 5.5(c) shows the measured population of mechanical states. The first mechanically excited state is populated with a probability of $\rho_{11} = 0.89(1)$. The remaining population was found predominantly in the ground state and to a small extent in the second and third excited states. The residual ground-state population likely stems from insufficient transfer, due to decoherence during the Raman pulse. Population in higher excited states must be a consequence of heating during optical pumping of the spin, following the Raman pulse.

5.3.3. Parametric Modulation

While Raman manipulations simultaneously drive coupled spin-mechanical transitions, direct modulation of the trapping potential can be used to solely manipulate the motional degree of freedom. The measurement technique described above characterizes the one-dimensional motion of the atom along the z-axis. The corresponding trapping potential is generated by the blue-detuned intracavity trap. The geometry of this trap, including the spatial position of light nodes, is defined by the position of the cavity mirrors, which are mounted in a rigid metal structure. To translate the trapping potential, the entire cavity must be mechanically moved, which is impossible due to the lack of mechanical

[6] An exponential decay is expected for coherences that decay with a constant rate. The case of a Gaussian distributed detuning, which remains constant for the duration of one experiment but changes in between experiments, yields coherences that decay with a Gaussian envelope as a function of time.

actuators and the physical mass involved. However, it is easy to modulate the depth of the potential by modulating the intensity of the intracavity lattice.

Parametric modulation of the trap potential, in a periodic manner [126] or by performing diabatic jumps [127, 141], excites breathing modes of motion in trapped ensembles. Observing the loss of atoms from a trap as a function of the frequency of a modulation applied to the depth of the trap is a well-established technique for determining trap frequencies and forcing evaporative cooling [142]. If the ensemble is replaced by a single atom in its ground state of motion, the excited breathing mode will be identical to a mechanical squeezed vacuum state [143].

The expectation value of the position and momentum coordinate $\langle x \rangle = \langle p \rangle = 0$ will be zero in the ground state of motion and in any parametrically excited state, as modulating the trap depth must preserve the state's spatial symmetry. The variances $\sigma_x^2 = \langle x^2 \rangle - \langle x \rangle^2$ and $\sigma_p^2 = \langle p^2 \rangle - \langle p \rangle^2$, however, will behave differently. In the ground state of motion, the variances are independent of time and their product is the lowest possible value allowed by the uncertainty relation $\sigma_x \, \sigma_p \geq \hbar/2$. A higher trap frequency will decrease the spatial variance σ_x but simultaneously the momentum uncertainty will increase by the inverse factor such that their product is always constant. This latter property holds for a squeezed state as well, but the two variances oscillate as a function of time.

This can easily be understood by considering the case of a diabatic jump in trap frequency. If the trap frequency is abruptly reduced ($\partial_t \omega \gg \omega^2$), the atomic wave function will be better localized around the origin than the ground state of the new potential. The atom would then possess excess kinetic energy at the expense of decreased potential energy compared to the ground state. The result is an oscillatory exchange of kinetic and potential energy similar to a harmonic oscillator except that the oscillation occurs in the width of the wave packet rather than its center-of-mass coordinate. In a classical picture, all of the initially displaced atoms will transit through the origin after a quarter period of the trap frequency. After another quarter period, they will appear at their mirrored starting positions, leading to the same positive initial value of the distribution's width. Thus, the oscillation of the variance occurs at twice the trap frequency.

In terms of energy eigenstates, the explanation can be phrased as follows: The spatial wave function that was left unaffected by the diabatic jump corresponds to a superposition of energy eigenstates in the lower trap potential. The phases of the energy eigenstates that appear in the superposition will evolve, leading to the breathing dynamics of the wave packet's width. As only even states contribute to the superposition, the periodicity of the evolution will be twice the trap frequency.

The populations of the energy eigenstates in a squeezed state can be calculated following the lines of the discussion above and using equation 5.6 for the overlap integral $\langle \Psi_\omega^m | \Psi_{\omega'}^n \rangle$ of two energy eigenstates (that are characterized by quantum numbers n and m) of harmonic oscillators with identical origin but different

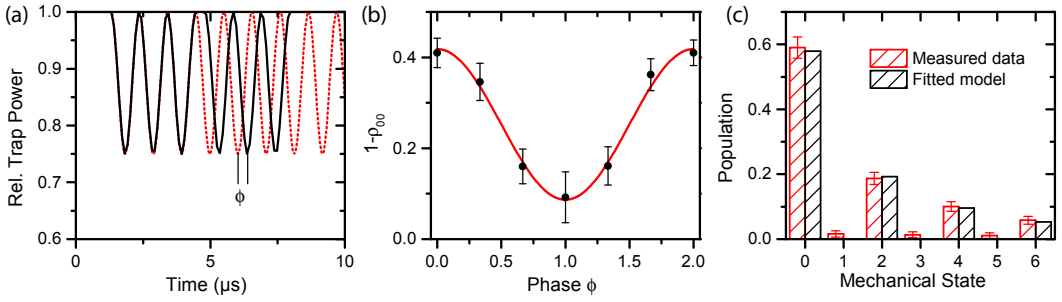

Figure 5.6.: Squeezing by parametric modulation (a) Modulation of the trap power. Two bursts of three periods each are generated with a variable delay between them that is equivalent to a phase shift ϕ (b) Summed population of all mechanically excited states $(1 - \rho_{00})$ as a function of the phase ϕ between two consecutively applied modulation bursts. (c) Measured population of the mechanical states $|n\rangle$ after six periods of trap modulation without an intermediate delay ($\phi = 0$). The black bars are calculated assuming a vacuum squeezed state with $\alpha = 9.8(1.2)$.

frequencies $\omega \neq \omega' = \alpha\omega$

$$|\langle \Psi_{\omega}^{0} | \Psi_{\alpha\omega}^{2n} \rangle|^2 = \frac{2\sqrt{\alpha}}{1+\alpha} \left(\frac{\alpha - 1}{2(\alpha + 1)} \right)^{2n} \frac{(2n)!}{(n!)^2} \tag{5.8}$$

A series of experiments studying the dynamics of the motional ground state perturbed by parametric modulation of the trap depth was performed. The power of the 772 nm intracavity trap was set to $P_{772} = 8\,\mu$W and the trap frequency of the $|F = 1, m_F = 0\rangle$ state was measured: $\omega_{1,0} = 2\pi \cdot 477\,$kHz. Figure 5.6(a) shows the modulation pattern that was applied for the first experiment. Two bursts of three periods were generated where the periodicity equaled twice the trap frequency. Between the two bursts, a short delay was introduced that corresponds to a phase shift of the second burst $\phi \in [0, 2\pi]$ with respect to the first burst. This modulation pattern was applied after cooling the atom to the ground state of motion and the population of mechanical states was recorded directly after application of the modulation. This experimental setting is reminiscent of a mechanical Ramsey interferometry experiment.

Figure 5.6(b) shows the summed population of mechanically excited states $1 - \rho_{00}$ as a function of the phase ϕ between the two bursts. For $\phi = 0$, the two bursts were generated one directly after the other resulting in six uninterrupted modulation periods. A maximum of 41(3) % of the atomic population were transferred to mechanically excited states. This value was reduced to 9(5) % when the second burst was applied out of phase with respect to the first burst ($\phi = \pi$). For longer delays ($\phi > \pi$), the observed ground-state population was reduced again.

The demonstrated phase-dependence of the second burst's effect on the atom

demonstrates coherent and potentially reversible excitation of motion by the first burst; this would correspond to parametric cooling of the atom [116] back to the ground state enabled by the knowledge of the exact phase and amplitude of the motion generated by the first burst. Unfortunately, an independent measurement with only the first three modulation periods was not carried out.

Figure 5.6(c) shows the phonon distribution of the mechanically excited state created with $\phi = 0$. The red bars are measured data and the black bars are a fit to the data of the distribution given by equation 5.8. The single parameter that characterizes the distribution is $\alpha = 9.8(1.2)$.

While the population distribution of a squeezed state with almost 10 dB squeezing in the spatial variance was well reproduced, the described technique does not permit measuring coherences in a straightforward manner. As mechanical states up to $n = 6$ were significantly populated, deviations in the energy eigenvalues from the harmonic approximation of almost one half trapping frequency are expected for the higher excited states (see Chapter 4.2). Thus, the coherences will evolve at rates that differ from the harmonic approximation and the dynamics of the spatial wave function will deviate from a breathing mode.

Still, these findings nicely demonstrate the power of the developed technique in studying motional dynamics of single trapped atoms.

5.4. Outlook

The demonstrated technique allows to drive spin transitions conditioned onto the motional eigenstate of the trap that is occupied by the atom. In combination with cavity-assisted hyperfine-state detection, this technique allows measuring the diagonal elements of the motional state's density matrix. The described calibration-free single-atom thermometry is a trivial, first application of this.

An intriguing future direction for research might be the implementation of a cavity-mediated interface between photonic and phononic states, as proposed by Parkins and Kimble [137, 138]. The aim of these proposals is to reach a regime where a single atom's trapping frequency is larger than the linewidth of the cavity in which the atom is embedded. In this case, the cavity interacts selectively with only one motional sideband and absorption of a photon of the coupled atom-cavity system is accompanied by generation or annihilation of a motional excitation (phonon). Excitation of an atom-cavity system in this resolved-sideband regime of cavity QED with squeezed light (e.g., from an optical parametric amplifier) would thus lead to pairwise excitation of phonons, analogous to the case of parametric excitation through modulation of the trap that was discussed above. Generation of phonon-pairs caused by the illumination with squeezed light can be proven using the method described here.

A cavity-mediated photon-phonon interface could also be used in the opposite direction. The non-destructive detection of motional states allows to probabilistically generate non-classical states. To this end, population of a certain

oscillator state in a classical motional state (e.g., a coherent state) is tested and experiments are then conditioned onto the result that this state is not populated. The remaining, partially projected state can have non-classical properties. With the techniques described in [137], these states could be mapped from the atom's motion onto the light field in the cavity.

6. Resonance Fluorescence of an Atom Pair

6.1. Introduction

Young's double-slit experiment in 1802 marked a milestone in the development of optics, and physics in general. For the first time, wave-like properties of light were unambiguously demonstrated [15]. Einstein's description of the photoelectric effect [2] then attributed obviously particle-like properties to light, and new questions about the double-slit experiment were raised. A corpuscular theory of light allowed one to ask which slit a single photon took and whether photons from independent sources could be made to interfere. The latter question addresses whether it was necessary for the original experiment to display interference that both slits were illuminated by the same source. In 1930, Paul Dirac stated that *"Each photon then interferes only with itself. Interference between two different photons never occurs."* [144] and was proven wrong in 1963 by Magyar and Mandel [145] who demonstrated that pulses from independent lasers could be brought to interference. Magyar and Mandel thus eliminated the single source that was common to both slits in Young's original experiment by truly independent sources.

Following the appearance of the laser [3], resonance fluorescence became an intensely studied subject and the non-classical properties of the light emitted by individual fluorescing atoms were discovered. Mollow predicted that the coherence properties of the light emitted by a driven atom would depend on the strength with which the atom is driven [4]. For weak driving, atoms behave like classical scatterers and the spectrum consists of a single peak at the frequency of the driving laser. For strong driving, the non-linear character of the atoms becomes noticeable and incoherent scattering, i.e. emission of light with no well-defined phase relation to the driving laser appears. While a weakly-excited atom thus can resemble a classical emitter at least in the correlation properties of the emitted electric field, Carmichael and Walls predicted in 1976 that the second-order coherence properties (i.e., correlations of the intensity rather than the field) would deviate from those of classical light [5] even for weak driving. The second-order intensity correlation function $g^{(2)}$, as introduced by Glauber [146], assumes the classically forbidden value of $g^{(2)}(\tau = 0) = 0$ for light emitted by a single atom.

Following earlier work e.g. by Mandel [16], Richter in 1991 studied interfer-

ence and $g^{(2)}$ correlation functions for light scattered from an ordered ensemble of individual atoms [18]. The spatial ordering of the atoms assures well-defined optical phases between the excitation laser, the atoms, and the detector in the far field. For weak excitation, the atoms behave as classical scatterers and a stable interference pattern appears in the intensity. For strong driving, the atoms do not maintain a constant phase relation and the intensity pattern vanishes. The interference pattern will still be visible though in a two-point $g^{(2)}(x_1, x_2)$ correlation function. Richter concluded that the full visibility of the modulation pattern expected in such a $g^{(2)}$ measurement could not be explained classically. While this effect was never observed, it was rediscovered and extended in theory several times [21, 22].

At the same time, the influence of an optical resonator on the properties of resonance fluorescence was theoretically studied. Meyer and Yeoman predicted in 1997 that surrounding two incoherently pumped atoms with a resonator along their axis can lead to phase synchronization of the atomic dipoles [30]. The surprising result was that a dark spot was expected on the symmetry axis in the interference pattern of the two atoms' emissions, transversal to the cavity axis. Thus, the system's symmetry is broken as the atomic dipoles would align opposite to each other. This result was extended one year later to the case of coherent driving by Rudolph and Ficek [20], where antisymmetric alignment of the atomic dipoles was expected for certain parameters as well. In modern terms, these were the first ideas towards steady-state entanglement in a tailored electromagnetic environment [41, 42].

Despite the large body of theoretical work, few experiments have been reported thus far. In a seminal experiment in 1993, David Wineland's group trapped two ions simultaneously in the same Paul trap and observed interference fringes in the collective fluorescence [27]. The polarization of the emitted light was correlated with different decay channels of the two ions. Polarization-sensitive detection thus allowed for generating which-way information and the resulting vanishing of the interference pattern appeared as the main result of this paper. Several groups reported Bragg scattering of light at regular atomic structure in optical lattices [126, 147, 148]. In these publications, the classical interference effects of light emitted from weakly excited atoms were used as a measurement tool rather than an object of research.

Two experiments looked at collective scattering from a cloud of ultracold atoms embedded in a resonator [149, 150]. The focus in these experiments was on mechanical back-action due to the recoil imprinted on the atoms during scattering instead of properties of the emitted light. Recently, two groups have worked towards realizing the described theoretical paradigm of an ordered structure of few atoms embedded in an optical resonator. In the group of Rainer Blatt, two ions were successfully trapped within the field of a Fabry-Perot type cavity. Owing to the problems that appear when bringing dielectric surfaces close to a Paul trap, the cavity is very long and therefore has a large mode volume. Significant coupling of the atom to the cavity can then only be achieved

by making the mirror extremely high reflective. The residual transmission that yields usable signal then typically becomes comparable to unavoidable scattering losses. Yet, in two proof-of-principle experiments, heralded entanglement of two ions [151] and an enhancement of photon generation efficiency by making use of collective effects could be shown [44]. Simultaneously in 2015, Dieter Meschede's group trapped two neutral atoms within a high-finesse optical cavity and observed cavity-modified Rayleigh scattering [45]. A fluctuating rate of photons emitted from the cavity was observed and interpreted as different optical phases being realized while the atoms were jumping between different sites of the two-dimensional intracavity lattice. The distribution of observed intensities was bimodal. The authors attributed the lower value to destructive interference and the higher value to constructive interference of the partial fields emitted by the atoms. Due to the lack of and independent means to measure the optical phases in this experiment, this appears as an a-priori assumption.

The two-atom experiment described in this chapter aimed to realize Young's double slit experiment with atoms instead of slits embedded in a high-finesse optical resonator. As such it incorporates many of the topics discussed earlier in this thesis. The ability to image pairs of atoms with single-site resolution in a two-dimensional optical lattice (see Chapter 2.4) permits the determination of the optical phases that are relevant to the scattering process. The ability to optically cool the atoms and keep them stationary (see Chapter 4) guarantees that a once realized value of the optical phases is not altered by jumping of the atoms between lattice sites. Strong tensor light shifts that are generated by the trapping light (see Chapter 3) are used to tailor the structure of the electronically excited energy eigenstates of the atoms, such that a clean two-level system can be isolated. In combination with a series of characterization measurements, this allows for quantitative predictions.

The theoretical description of the two-atom-cavity system in terms of coupled eigenstates is presented in Chapter 6.2 with and without an external drive. The numerical model applied to quantitatively describe the system, including incoherent damping processes is described in Chapter 6.3; the extreme cases of perfect constructive and destructive emission of the two atoms into the resonator are discussed. Characterization measurement on a single-atom cavity system were performed to quantify experimental imperfections. Chapter 6.4 discusses the mathematical treatment of these imperfections and the measurement results. Chapter 6.5 explains how the single-site resolved images are evaluated in order to calculate the difference in the optical phases that is relevant to the two-atom experiments. Experimental data on the two-atom case are presented in chapter 6.6.

6.2. Tavis-Cummings Model

6.2.1. Unperturbed System

In this section, the energy spectrum of the unperturbed (two)-atom-cavity system and some general properties are derived. A quantized cavity is considered, described by its Fock states $|n\rangle$ and annihilation (creation) operators $a(a^\dagger)$ and two-level atoms with ground state $|g\rangle$ and excited state $|e\rangle$ that are described by the ladder operators $\sigma^+ = |e\rangle\langle g|$ and $\sigma^- = |g\rangle\langle e|$. The atomic transition $|e\rangle \leftrightarrow |g\rangle$ is on resonance with the frequency ω_{cav} of the cavity mode. Interaction of the j^{th} atom with the intracavity field is parametrized by the coupling strength g_j. In the rotating-wave approximation, the unitary part of the systems evolution is described by the Tavis-Cummings Hamiltonian [152]

$$H_{\mathrm{TC}} = \sum_j |g_j|(\sigma_j^+ e^{i\phi_j} a + \sigma_j^- e^{-i\phi_j} a^\dagger) \tag{6.1}$$

Here, the coupling strength $g_i = |g_i|e^{i\phi_i}$ is expressed in terms of its modulus and phase ϕ_i.

In the standing-wave mode of the Fabry-Perot type cavity under consideration, the light's phase will be constant inbetween two nodes of the light field while the field amplitude varies. Since the blue intracavity trap at 772 nm (see chapter 4) confines the atoms to antinodes of the resonant standing-wave field at 780 nm, the modulus $|g_i|$ can be assumed constant and ϕ_i will be discretized to the two values 0 and π. It is important to consider the physical reality of this phase and its impact on experiments. For a single atom, the phase is a global phase not relevant here; for two atoms, the distance between the atoms measured along the cavity axis and the resulting phase difference between the two atoms are introduced as new parameters. An even (odd) number of trapping sites between the atoms introduces a 0 (π) phase difference between the atoms in their coupling to the cavity. While the two situations are seemingly distinguishable to an external observer, they are not distinguishable when the system is only probed through interaction with the cavity mode[1] (e.g. via transmission or reflection of a probe field).

Figuratively speaking, the atoms in this case lack a common clock, against which they could measure the phase of the local electric field. Atoms at a distance that is equal to an odd number of trapping sites will consequently build up dipole moments that are mutually anti-aligned. However, with respect to the local electric field they are aligned in the same manner as in the case two atoms that incorporate a distance that is equal to an even number of trapping sites. Mathematically, the phase terms $e^{i\phi_i}$ can be removed by a gauge transformation of the atomic operators $\sigma^+ e^{i\phi_i} \rightarrow \tilde{\sigma}^+$, which are not observable. The phases

[1] And the atoms are well separated by a distance $d \gg \lambda$ that renders direct dipole interactions (DDI) unimportant [153, 154]

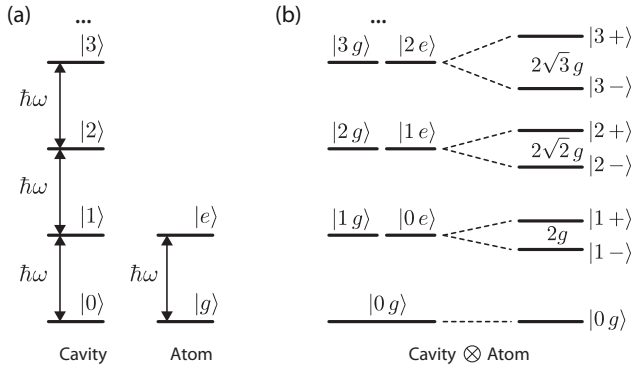

Figure 6.1.: Energy eigenstates of a single-atom-cavity system (a) Ladder of Fock states $|n\rangle$ of the empty cavity and ground- ($|g\rangle$) and excited ($|e\rangle$) states of the atom. The cavity mode is assumed to be on resonance with the bare atom's transition frequency. (b) Energy eigenstates of the composite atom-cavity system without (left) and with (right) light-matter interaction that couples states $|(n-1)\,e\rangle$ and $|n\,g\rangle$ at a rate g leading to the anharmonic Jaynes-Cummings ladder.

become relevant in the case where the atoms are driven instead of the cavity, as a transversally propagating driving laser provides the mentioned common clock against which the atoms can compare the phase of the cavity field at their respective positions.

The Tavis-Cummings Hamiltonian in the rotating-wave approximation commutes with the operator $N = a^\dagger a + \sum_j \sigma_j^+ \sigma_j^-$ that counts the total number of excitations in the system. Figure 6.1(a) shows the energy eigenstates of the individual systems, namely the harmonic ladder of Fock states $|n\rangle$ in the cavity and the two states of the atom(s), $|e\rangle$ and $|g\rangle$. On the left side of panel (b), these states are rearranged in terms of eigenstates of the composite but uncoupled single-atom system forming a ladder with a well-defined number of total excitations $\langle N\rangle$ on each rung. Apart from the ground state, every rung of the ladder is two-fold degenerate as the states $|(n-1)\,e\rangle$ and $|n\,g\rangle$ have the same energy $\langle N\rangle$, but no two rungs have the same energy. For a non-zero coupling strength $g > 0$, the Hamiltonian will couple only states of one rung and in the case of one atom, diagonalization yields the eigenstates and eigenenergies:

$$|n\pm\rangle = \sqrt{1/2}(|n\,g\rangle \pm |(n-1)\,e\rangle) \tag{6.2}$$

$$E_{n,\pm} = n\hbar\omega \pm \sqrt{n}g \tag{6.3}$$

The anharmonic splitting $E_{n,+} - E_{n,-} \propto \sqrt{n}$ of the normal modes is at the heart of many fundamental single-atom cavity QED effects. Among them are the collapse and revival of Rabi oscillations [155], photon-blockade in optical cavity QED [156, 157], and non-linear two-photon transitions [158]. The observation of these effects marked milestones in the development of the field.

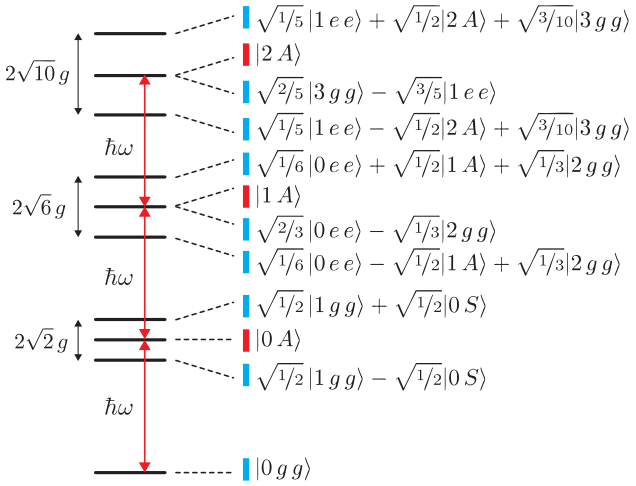

Figure 6.2.: Energy eigenstate of the two-atom-cavity system Both atoms are resonant with the single cavity mode. The blue (red) bars indicate states that are symmetric (antisymmetric) with respect to exchange of the atoms.

The energy eigenstructure of a system that consists of $m > 1$ atoms coupled to a single mode becomes complicated with increasing m. The degeneracy of the N^{th} rung in the uncoupled system is $\sum_{k=0}^{N} \left(\begin{array}{c} m \\ k \end{array} \right)$. Note that as $\left(\begin{array}{c} m \\ k \end{array} \right) = 0$ for $k > m$, the degeneracy is 2^m for all rungs $N \geq m$. The photon number n of states on a given rung with the total excitation number N can vary between $0 \leq n \leq N$. This leads to a complex structure of the matrix elements of H_{TC} and consequently to a complex structure of the diagonalized excited states. Yet, some general properties can be identified:

For a single excitation in the system, the Hamiltonian couples each atomic excited state solely to the state $|1\,g\,\ldots\,g\rangle$, with a single photon in the cavity and all atoms in their ground state. Likewise, $|1\,g\ldots g\rangle$ is coupled to a symmetric superposition of all states, in which a single atom is excited $|D_1\rangle = 1/\sqrt{m}\sum_{k=0}^{m}|0\,g\ldots e_k\ldots g\rangle$. This state is a Dicke state that appears in the theory of superradiance [159, 160]. Diagonalization of this Hamiltonian yields the collective normal modes $|1\,\pm\rangle = \sqrt{1/2}(|1\,g\ldots g\rangle \pm |0\,D_1\rangle)$ in which - in analogy to the single-atom case - a single excitation is shared between the cavity mode and a collective excitation of the atoms. The energy of the collective normal modes of the first rung is $\hbar\omega \pm \sqrt{m}g$. The remaining $m+1$ states will stay energetically unshifted at $\hbar\omega$ and can be denoted as $\sqrt{1/2}(|0\,g\ldots e_a\ldots g_b\ldots g\rangle - |0\,g\ldots g_a\ldots e_b\ldots g\rangle)$. These are states in which a single excitation is shared antisymmetrically between an atom pair without excitation of the cavity. The $\sqrt{m}$ scaling of the normal mode splitting that can be observed through transmission spectroscopy [51, 161], has led to the terms *collectively enhanced coupling* and even *superatom*, which suggest that m atoms can be thought of as a single atom

with $\sqrt{m}$ enhanced coupling strength. This notion holds for weak excitation, but breaks down as soon as atomic saturation and excitation to the second rung of the Tavis-Cummings ladder begin to play a role.

For two atoms, it is worthwhile to note that $\mathcal{H}_{\mathrm{TC}}$ commutes with exchange of the atoms. The atomic Hilbert space can be divided into a part that is symmetric with respect to atomic exchange $|g\,g\rangle$, $|e\,e\rangle$, $|S\rangle = \sqrt{1/2}(|e\,g\rangle + |g\,e\rangle)$ and the state $|A\rangle = \sqrt{1/2}(|e\,g\rangle - |g\,e\rangle)$. Compound systems that are comprised of identical two-level systems are often treated in terms of their coupled pseudo-spin. In this context, the set of symmetric states corresponds to the triplet system $|S = 1, m_S = -1, 1, 0\rangle$ and the asymmetric state $|A\rangle$ corresponds to the singlet state.

The energy eigenstates of the coupled two-atom-cavity system are shown in Fig. 6.2 when both atoms are on resonance with the cavity mode and coupled with identical g_j. The colored bars indicate that the atoms are in symmetric (blue) or antisymmetric states (red).

6.2.2. Driven System

An excitation laser that drives the atomic part of the two-atom cavity system with Rabi frequency Ω is described by the Hamiltonian:

$$\mathcal{H}_{\mathrm{drive}} = \frac{\Omega}{2}(e^{i\phi_3}\sigma_1^+ + e^{-i\phi_3}\sigma_1^- + e^{i\phi_4}\sigma_2^+ + e^{-i\phi_4}\sigma_2^-) \tag{6.4}$$

Adding this to the Hamiltonian of the unperturbed system that is described by equation 6.1 yields a total of four phases ϕ_j. Similar to the treatment of the unperturbed system, the following transformations are applied:

$$\sigma_1^+ \rightarrow +e^{-i\phi_3}\tilde{\sigma}_1 \tag{6.5}$$
$$a \rightarrow e^{-i(\phi_1-\phi_3)}\tilde{a} \tag{6.6}$$
$$\sigma_2^+ \rightarrow e^{i(\phi_2-\phi_1+\phi_3)}\tilde{\sigma}_2^+ \tag{6.7}$$

These transformations collect all of the four phases in the phase difference $\phi = (\phi_1 - \phi_2) - (\phi_3 - \phi_4)$ that remains in front of one atomic operator and its Hermitian conjugate, and the driving term then reads:

$$\mathcal{H}_{\mathrm{drive}} = \Omega/2(\sigma_1^+ + \sigma_1^- + e^{i\phi}\sigma_2^+ + e^{-i\phi}\sigma_2^-). \tag{6.8}$$

While these transformations appear complicated, they bare only few physical meaning. The same four phases are found in a classical Young's double slit experiment in which they describe the optical pathways from the source to the two slits and from the slits to the detector. As long as intensities are the only quantities of concern, and the phase relation of the light in the detector plane with respect to the light source is not considered, the whole physics can as well be captured by a single phase. This argument is reflected in the described case

by the fact that intensity expectation values $a^\dagger a$ (or higher orders thereof) are left unaffected by the transformation.

This means that every spatial configuration of atoms can be mapped onto an equivalent pattern, in which the atoms are aligned along one phase front with respect to the cavity field (i.e., along a single line along the x-axis), and differ only in the phase with which they couple to the driving laser. Furthermore, the observed physics is invariant under translations of the whole atomic pattern. This would not remain true, if the electric field of the light emitted from the cavity was measured in a homodyne setup with the excitation light as a local oscillator.

The phase difference ϕ with which the atoms couple to the cavity mode and to the driving laser defines the matrix element between atomic symmetric and antisymmetric states. For $\phi = 0$, which is referred to as the in-phase situation, the driving term only couples states with identical symmetry with respect to atom exchange. Conversely, for $\phi = \pi$, each photon absorbed by the atoms leads to an inversion of the atomic symmetry. The possible excitation pathways from the atomic ground state $|g\,g\rangle$ are:

$$\begin{aligned} \phi = 0 \quad &\Rightarrow \quad |g\,g\rangle \leftrightarrow |S\rangle \leftrightarrow |e\,e\rangle \\ \phi = \pi \quad &\Rightarrow \quad |g\,g\rangle \leftrightarrow |A\rangle \leftrightarrow |e\,e\rangle \end{aligned}$$

Comparing these atomic excitation pathways to the energy eigenstates of the coupled system in Fig. 6.1(c) reveals a property that is at the heart of the different radiation dynamics for the in-phase and out-of-phase situation. Via the in-phase excitation path, the ladder of states can be climbed rung by rung with unity increments in the photon number in the cavity. For out-of-phase coupling, odd rungs of the ladder may resonantly be excited only by coupling to atomic asymmetric states, which do not couple to the cavity. As a consequence, only energy eigenstates with an even number of photons in the cavity are found in the excitation pathway.

6.3. Light-Matter Dynamics

6.3.1. Numerical Model

In order to make quantitative predictions about the systems, dissipative processes must be considered together with the unitary evolution described by the Hamiltonian in equations 6.1 and 6.4. The relevant processes are loss of photons from the cavity field and spontaneous decay of atomic excitation due to emission of photons into free-space modes. The former is described by the field decay rate $\kappa = \kappa_{\mathrm{OC}} + \kappa_{\mathrm{loss}} = 2\pi \cdot 2.75\,\mathrm{MHz}$, which is the sum of the emission through the outcoupling mirror and κ_{loss} that subsumes scattering and absorption losses in the cavity and transmission through the high reflector (see Chapter 2.2).

Dissipation from the system due to the atom's coupling to free-space modes is described by the rate $\gamma = 2\pi \cdot 3.03\,\mathrm{MHz}$ at which atomic polarization decays. To account for the effect of these decohereing processes, a density matrix approach is chosen and the loss mechanisms are described as Lindblad super-operators.

The evolution of the system's density matrix ρ is given by the Liouville-von Neumann equation:

$$\begin{aligned} \partial_t \rho &= -\frac{i}{\hbar}[\mathcal{H}, \rho] && (6.9)\\ &+ \kappa(2\, a\rho a^\dagger - a^\dagger a\rho - \rho a^\dagger a) && (6.10)\\ &+ \gamma \sum_j (2\, \sigma_j^- \rho \sigma_j^+ - \sigma_j^+ \sigma_j^- \rho - \rho \sigma_j^+ \sigma_j^-), && (6.11) \end{aligned}$$

where the sum runs across all atoms. The unitary part of the evolution is described by the driven Tavis-Cummings Hamiltonian $\mathcal{H}$. The resonant Tavis-Cummings Hamiltonian, as discussed in Chapter 6.2.2, did not account for differences in the frequencies of atomic transition ω_{eg}, cavity resonance ω_c and excitation laser ω. To include these, terms for a cavity detuning $\Delta_c = \omega - \omega_c$ and atomic $\Delta_{a,j} = \omega - \omega_{\mathrm{eg,j}}$ detuning for each atom are added. All detunings are defined with respect to the excitation laser[2]. The complete Hamiltonian with the phase convention described in Chapter 6.2.2 then reads:

$$\begin{aligned} \mathcal{H} &= |g| \sum_j (\sigma_j^+ a + \sigma_j^- a^\dagger) + \frac{\Omega}{2}(\sigma_1^+ + \sigma_1^- + e^{i\phi}\sigma_2^+ + e^{-i\phi}\sigma_2^-) && (6.12)\\ &- \sum_j (\Delta_{a,j} \sigma_j^+ \sigma_j^-) - \Delta_c a^\dagger a. && (6.13) \end{aligned}$$

All of the experimental observables A that are relevant to the described experiment can be found by solving for the system's steady-state density matrix $\partial_t \rho_{\mathrm{ss}} = 0$ and calculating the expectation value $\langle A \rangle = \mathrm{Tr}(A\, \rho_{ss})$.

Figure 6.3 shows the result of simulations of an ideal two-atom cavity system that is transversally driven. The cavity parameters that were used are identical with those of the experimental setup $(g, \kappa, \gamma) = 2\pi \cdot (7.62, 2.75, 3.03)\,\mathrm{MHz}$. Panel (a) shows the intracavity population $\langle a^\dagger a \rangle$ as a function of the phase difference ϕ with which the atoms couple to the cavity and the external driving laser. The atoms are resonant with the cavity mode and driven at the same frequency. For a small Rabi frequency ($\Omega = 2\pi \cdot 100\,\mathrm{kHz}$) an interference fringe is predicted that drops almost to $\langle a^\dagger a \rangle = 0$ for destructive interference of the individual atoms' emission ($\phi = \pi$). The dotted black line is calculated for a ten-fold increased Rabi frequency $\Omega = 1\,\mathrm{MHz}$ and scaled by a factor of 100 corresponding to the squared ratio of the two Rabi frequencies.

[2]While the experiments described in this chapter were conducted with the atoms being on resonance with the cavity, these terms must be taken into account to model the residual thermal excitation of the atoms.

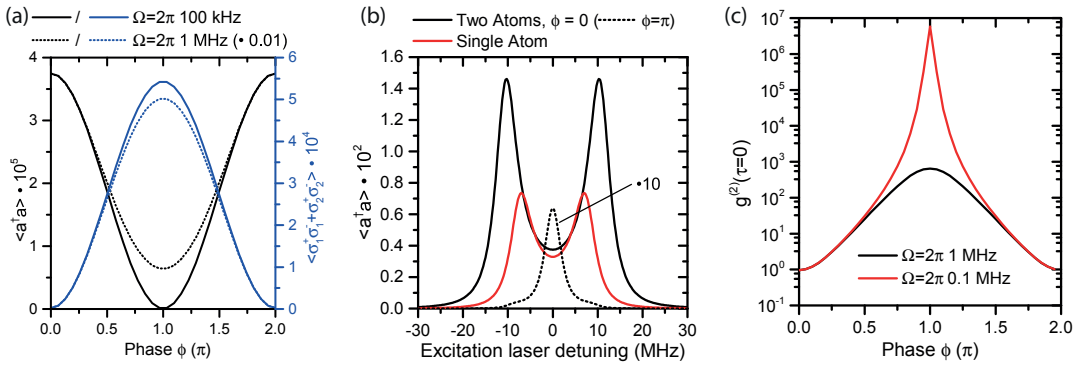

Figure 6.3.: Numerical simulation of the driven two-atom cavity system (a) Expectation value of cavity population $\langle a^\dagger a\rangle$ (black) and atomic excitation $\langle \sum_i \sigma_i^+ \sigma_i^-\rangle$ (blue) for resonant driving with two different Rabi frequencies $\Omega = 2\pi \cdot 100\,\mathrm{kHz}$ (straight line) and $\Omega = 2\pi \cdot 1\,\mathrm{MHz}$ (dotted line). The curves for the tenfold greater Rabi frequency are scaled by a factor of $1/100$. (b) Cavity population as a function of the excitation laser's detuning from the two atoms and the cavity for two different values of the scattering phase $\phi = 0$ (straight line) and $\phi = \pi$ (dotted line). The Rabi frequency of the driving field is $\Omega = 1\,\mathrm{MHz}$. The red line is calculated for a single atom. (c) Value of the second-order correlation-function $g^{(2)}(\tau = 0)$ as a function of the scattering phase ϕ between the atoms for resonant driving at two different Rabi frequencies.

The two curves agree for in-phase emission from the two atoms into the cavity ($\phi = 0$); thus, the cavity population grew proportional to the intensity of the driving field. A discrepancy appears for destructive interference, as the predicted interference fringe no longer drops to zero, indicating a light-scattering mechanism that involves absorption of several photons at once and therefore scales at least quadratically with the intensity.

The blue lines in panel (a) show the expected total atomic excitation $\langle \sum_i \sigma_i^+ \sigma_i^-\rangle$ for the same choice of parameters as the corresponding black lines. An interference fringe is predicted that is inverted with respect to the cavity population in the sense that the atoms have a maximum excitation probability for destructive interference of their individual emission into the resonator, whereas they are likely to stay in their ground state when they emit in-phase.

Panel (b) shows the intracavity population $\langle a^\dagger a\rangle$ when driving the atoms with a Rabi frequency of $\Omega = 2\pi \cdot 1\,\mathrm{MHz}$ as a function of the driving laser's detuning. The straight black line shows the calculated values for in-phase scattering and the black dotted line for out-of-phase scattering. The red line is calculated for a single atom in the cavity under the same conditions. For resonant driving, correspondence with the data in panel (a) is found in that the expected cavity population drops to a residual non-zero value when changing the scattering phase from $\phi = 0$ to $\phi = \pi$. Comparison with other values of the driving laser's detuning shows that the two situations behave very differently. The

in-phase situation is qualitatively very similar to the single-atom case with a double peaked structure that attains the highest values when the two normal modes $(|1\,g\rangle\rangle \pm |0\,e\rangle)/\sqrt{2}$ are driven resonantly at a detuning of $\pm g$ from the bare atom's resonance. The transition from a single atom to two atoms further separates the two maxima, which are now found at $\pm\sqrt{2}g$ and correspond to the excitation of the collective normal modes $(|1\,g\,g\rangle \pm |0\,S\rangle)/\sqrt{2}$. Remarkably, the cavity population remained almost unchanged when driving the system on the bare atomic resonance and adding a second atom in phase to an already present atom. This contradicts the free-space intuition of a fourfold increase in intensity when a second field of identical amplitude is added in-phase to an already existing field. This effect is discussed in Chapter 6.3.2. For out-of-phase scattering, a singly-peaked curve is found that, in contrast to $\phi = 0$, attains its maximum value when driving the system on the bare atomic resonance.

In addition to the expectation value of the intracavity population, qualitatively different behaviour of the system for different values of ϕ was found as well in the fluctuations of the cavity population. Panel (c) shows the value of the second order correlation function $g^{(2)}(\tau = 0) = \langle a^\dagger a^\dagger a\, a\rangle / \langle a^\dagger a\rangle^2$ at $\tau = 0$. This value measures the likelihood of observing a coincident detection of a photon pair normalized to the expected rate of coincident detections for a coherent field of the same intensity. For in-phase emission ($\phi = 0$), a value of $g^{(2)}(0)$ that is very close to 1 was found for both Rabi frequencies that were simulated. From the definition of the second-order correlation function follows:

$$\frac{\langle a^\dagger a^\dagger a a\rangle}{\langle a^\dagger a\rangle^2} = \frac{\langle a^\dagger (a a^\dagger - 1) a\rangle}{\langle a^\dagger a\rangle^2} = 1 \Rightarrow \langle n^2\rangle - \langle n\rangle^2 = \mathrm{Var}(n) = \langle n\rangle, \tag{6.14}$$

where $n = a^\dagger a$, indicating that the variance of the photon number distribution is identical to its expectation value. For phases $\phi \neq 0$, $g^{(2)}(0)$ assumes large values that indicate strong super-Poissonian photon statistics[3]. The correlation function assumes a maximum for $\phi = \pi$. The effects occuring for out-of-phase driving are discussed in Chapter 6.3.3.

6.3.2. In-Phase Emission

Three remarkable observations were made in the numerical simulation of constructive interference. In the case of resonant driving, the average cavity population changed slightly when adding a second atom emitting in-phase to an already present atom. This appears to contradict the free-space intuition of a fourfold increase in intensity. Furthermore, the atom excitation probability was predicted to drop to almost zero although the cavity field was populated. This is

[3]Super-Poissonian in the sense that the variance of the photon number distribution exceeds the expectation value. A value of $g^{(2)}(0) = 1$ does not necessarily indicate Poissonian photon statistics. It only makes a statement about the variance of the statistics being equal to a Poisson distribution.

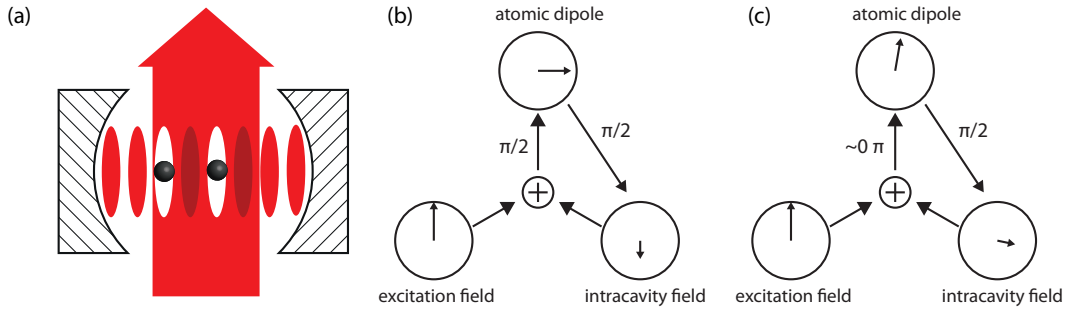

Figure 6.4.: System excitation in the in-phase regime (a) In steady state, the intracavity field and the excitation field act on the atoms. As the intracavity field is of opposite phase, it counteracts the driving of the excitation field. For a lossless cavity, spatial regions of perfect destructive interference between the intracavity field and the excitation field form and the steady state does not depend on the atom number at all. (b) Relative strength, phase-relations and mutual dependencies of excitation field, induced atomic dipole, and intracavity field when the frequencies of the atomic transition, the excitation laser, and the cavity resonance are identical. The arrows mark the amplitude and phase with the excitation field used as a reference shortly. (c) The same quantities as in panel (b) shown for the case of a detuned atom. See text for a detailed explanation. Both panels illustrate the transient situation shortly after switching on the driving field.

in contrast to the out-of-phase situation in which the atoms are excited but the cavity excitation probability was low. Finally, the intensity-correlation function also deviates strongly from a free-space intuition. The value of $g^{(2)}(\tau = 0)$ is zero for a single atom in free space, regardless of the driving strength. In other words, a single observed photon that defines $\tau = 0$ in a correlation measurement heralds the atom's decay to its ground state. With N independently emitting atoms, detection of a first photon heralds the decay of only one of the atoms and from the remaining atoms stems a finite chance to see a second photon simultaneously. One can thus predict a value of $g^{(2)}(\tau = 0) = 1 - 1/N$ for a free-space situation, which evaluates to $g^{(2)} = 0.5$ in the two-atom case considered here.

The numerically predicted effects for in-phase emission have been analyzed and explained by Alsing and Carmichael [162]. They turned out to be a classical effect that does not require quantization of the light mode or of the atoms in order to be explained. While Alsing and Carmichael focused on the effect of suppressed atomic excitation for a single atom, Ritsch and colleagues later generalized the treatment to multiple atoms [31].

The effect can easily be understood by considering the case of a perfect, lossless resonator ($\kappa = 0$) that holds a single atom. The atom's resonance frequency is identical with the cavity's resonance and the atom is driven with a laser at even this frequency. The following argumentation is outlined in Fig. 6.4(a). The resonant driving laser will excite an atomic dipole moment that is $\pi/2$ phase-

shifted compared to the excitation laser. This atomic dipole couples resonantly to the cavity field, which will have another $\pi/2$ phase difference compared to the exciting atomic dipole; it will therefore be out of phase with the excitation laser. As both, the driving and the intracavity field act upon the atom, the growing intracavity field will reduce the total field strength at the position of the atom. In the system's steady state, the intracavity field will have grown to exactly the strength of the driving field and will perfectly counteract this field, such that the atom will sit in a dark spot within the interference pattern of the intracavity field and the driving field. In this case, an arbitrary number of atoms can be placed into the dark spots of the interference pattern without altering the steady state.

This argument can be extended to detuned systems that were experimentally investigated in [45]. In this case, the atom was detuned from the cavity by many linewidths, but was driven at the resonance frequency of the surrounding cavity. This situation - again during the transient dynamics into the steady state - is depicted in Fig. 6.4(b). The only difference to the resonant case is that the induced atomic dipole has only a small phase-difference with respect to the excitation laser. However, since it nevertheless oscillates with the excitation field's frequency, it can resonantly excite the cavity. The intracavity field will therefore be slightly more than $\pi/2$ out-of phase with respect to the excitation laser. The transient dynamics into the steady state thus differs from the resonant case, as the intracavity field does not directly counteract the excitation field from the beginning. A more complex evolution of the sum of the intracavity and the driving field is the consequence, but the steady state remains the same. Also in the detuned case, the steady state intracavity population does not depend on the number of atoms.

The argument presented above, extended by cavity loss, was put into mathematical terms in [45] using the classical treatment of cavity QED from [163]. The ratio of the field strength of the intracavity (standing-wave) field E_{cav} and the driving field E_{drive} at the position of the N atoms can be identified as:

$$\frac{E_{\mathrm{cav}}}{E_{\mathrm{drive}}} = -\frac{1}{\frac{1}{2NC}+1}, \tag{6.15}$$

with the single-atom cooperativity $C = g^2/(2\kappa\gamma)$. This ratio will be arbitrary close to -1 for large cooperativities, indicating the perfect, destructive interference of the cavity and the driving field. The ratio's dependency onto the number of atoms N will also be suppressed for large C.

Alsing and Carmichael [162] stated that the classical treatment remains valid even for strong atom driving that leads to atomic saturation in free-space and their quantized treatment of the problem showed that the intracavity field is an identical copy of the coherent excitation field, explaining the value of $g^{(2)}(\tau) = 1$.

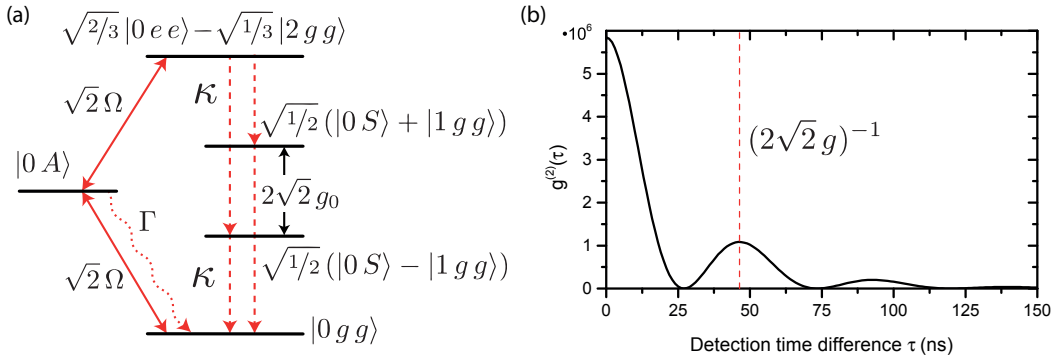

Figure 6.5.: System excitation in the out-of-phase regime (a) Excitation pathway of the two-atom cavity system when the two atoms couple with opposite phase to the driving laser and the intracavity mode. A two-step excitation to the second rung of the Tavis-Cummings ladder can lead to population of the cavity with two photons simultaneously. (b) The $g^{(2)}(\tau)$ correlation function calculated as a function of the detection time difference τ allows observation of the emission dynamics of the second photon of this pair. Collective Rabi oscillations of the second emitted photon between the resonator and the atoms are predicted with a revival of cavity population after $\tau = 46.4\,\mathrm{ns} = (2\sqrt{2}\,g)^{-1}$.

6.3.3. Out-Of-Phase Emission

While the in-phase regime could be explained in classical terms, this is not the case for out-of-phase excitation of the system. Two classical emitters that are embedded in a cavity and excited with opposite phases will always emit destructively into the cavity, regardless of the driving strength; no excitation of the cavity mode is thus expected. To explain the numerical findings of non-zero excitation of the resonator and strong super-Poissonian photon emission, the atoms have to be treated as two-level systems rather than classical oscillators. Figure 6.5(a) shows the excitation pathway of Tavis-Cummings energy eigenstates when the system is driven in the out-of-phase case. With each transition from one rung to the next, atomic symmetry is inverted. The system's ground state $|0\,g\,g\rangle$ is coupled to the atomic antisymmetric state $|0\,A\rangle = (|0\,g\,e\rangle - |0\,e\,g\rangle)/\sqrt{2}$ in the first rung. This state decays predominantly via emission of a photo from the atom into free space and the resonator is left in its ground state. When the driving strength is not negligible with comparison to the excited state's lifetime, excitation to the second rung can happen before $|0\,A\rangle$ decays and the energy eigenstate $\sqrt{2/3}|0\,e\,e\rangle - \sqrt{1/3}|2\,g\,g\rangle$ can be resonantly excited through the coupling of $|0\,A\rangle$ to the fully atomic saturated state $|0\,e\,e\rangle$.

In this state of the doubly excited manifold, the cavity is either in its vacuum state or populated with two photons simultaneously. But it will never be excited with a single photon only. This explains the large value of the $g^{(2)}(\tau)$ correlation function for $\tau = 0$. The detection of a first photon heralds the decay of the

system from $\sqrt{2/3}|0\,e\,e\rangle - \sqrt{1/3}|2\,g\,g\rangle$ to the state $|1\,g\,g\rangle$. In this state, the cavity remains excited and can immediately emit a second photon.

In terms of the Tavis-Cummings energy eigenfunctions, the state $|1\,g\,g\rangle$ is a symmetric superposition of the two collective normal modes. Emission of a second photon brings both of these energy eigenstates back to the ground state $|0\,g\,g\rangle$ and interference of the two emission paths is expected. Figure 6.5(b) shows a numerical evaluation of the $g^{(2)}(\tau)$ correlation function for the parameters $(g, \kappa, \gamma, \Omega) = 2\pi(7.62, 2.75, 3.03, 0.1)\,\mathrm{MHz}$ (red line in Fig. 6.3(c)). The discussed interference of the second photon's two possible decay paths results in a beating in the emission at a frequency of $(2\sqrt{2}\,g)^{-1}$, which is identical to the splitting between the two collective normal modes.

This oscillation can also be understood in a corpuscular way. The single photon left in the cavity after emission of a first photon either decays directly by emission out of the cavity or is collectively absorbed by the two atoms and then reemitted into the cavity. The system's excitation is thus purely photonic for $\tau = 0$, purely atomic for $\tau = 1/2(2\sqrt{2}\,g)^{-1}$, and again purely photonic after a full cycle of the collective vacuum Rabi oscillations.

6.4. Preparatory Measurements

In all of the experiments described in preceding chapters, the optical resonator surrounding the atoms was only used for cavity-assisted hyperfine state detection. Parameters of the atom interrogation, such as light polarization, intensity and detunings, were experimentally chosen aiming for an emitted signal that enables faithful discrimination of the two hyperfine states. A quantitative understanding of the light-matter interaction occuring in the resonator was therefore not necessary. This is different for the two-atom interference experiments. Achieving quantitative agreement between theory and experiment requires a thorough understanding of these parameters and detrimental experimental imperfections.

This section discusses preparatory measurements that were conducted with a single atom and were used to gain quantitative understanding of residual thermal excitation and imperfect optical pumping.

6.4.1. Cavity Reflection Spectroscopy

Cavity reflection spectroscopy was used to quantify the efficiency of optical pumping and the strength g of coherent light-matter interaction. This technique was previously introduced in Chapter 2.2 and it was found that quantitative agreement between measurement and theory in reflection spectroscopy requires that interference effects are taken into account. These effects stem from imperfect mode matching of the incident light to the cavity mode in combination with the collection of the reflected light with a single-mode fibre (see

Fig. 6.6(a)). Equation 2.2 provides a theoretical model for the observed reflectivity of an empty cavity. The values of the two parameters that characterize the interference effects were $\eta = 0.89$ and $\phi = 0.173$.

The reflectivity of the coupled two-atom cavity system can be calculated by following the treatment in reference [164]. Assuming a weak incident field and therefore vanishing atomic excitation, the field reflectivity of the two-atom cavity system is:

$$r_2(\Delta, \Delta_{a,1}, \Delta_{a,2}) = 1 - \frac{2\kappa_{\mathrm{OC}}}{i\Delta + \kappa + \frac{g_1^2}{i(\Delta+\Delta_{a,1})+\gamma} + \frac{g_2^2}{i(\Delta+\Delta_{a,2})+\gamma}}. \tag{6.16}$$

Here, $\Delta, \Delta_{a,1}$ and $\Delta_{a,2}$ are the detunings of the probe laser and the first and second atom from the resonance frequency of the empty resonator. g_1 and g_2 are the coherent coupling strengths of the two atoms, and κ and κ_{OC} are the resonator's total field decay rate and the partial decay rate caused by transmission through the output coupling mirror. γ describes the atomic polarization decay rate. For $g_1 = g_2 = 0$ the equation collapses into equation 2.1 describing the empty cavity reflectivity. The effect of an additional reflected field that has not interacted with the cavity mode is accounted for in the same manner as in Chapter 2.2 and the following expression for the modified reflectivity of the two-atom cavity system is found:

$$R_2(\Delta, \Delta_{a,1}, \Delta_{a,2}) = \frac{|\eta r_2(\Delta, \Delta_{a,1}, \Delta_{a,2}) + (1-\eta)e^{i\phi}|^2}{\eta^2 + (1-\eta)^2 + 2\eta(1-\eta)\cos(\phi)}. \tag{6.17}$$

Figure 6.6(b) shows the phase $\mathrm{Arg}(r_2(\Delta, 0, 0))$ of the reflected field for an empty cavity and with a single atom coupled to the cavity[4]. The curves were calculated with the parameters $(\kappa, \kappa_{\mathrm{OC}}, \gamma) = 2\pi \cdot (2.75, 2.42, 3.03)\,\mathrm{MHz}$ and the theory value $g = 2\pi \cdot 7.84\,\mathrm{MHz}$ for the light-matter coupling constant. Due to the normal mode splitting caused by the atom, no energy eigenstate of the coupled system can be resonantly excited at the frequency of the empty cavity resonance. The phase of the reflected field differs by exactly π in the two cases. The effect of imperfect mode matching shown in Fig. 6.6(c) is therefore less pronounced in the case of a single coupled atom with respect to the empty cavity. It fails to explain the high reflectivity $R \approx 0.25$ that is observed on the single-atom normal mode resonances in the experiment.

Inhomogeneous broadening of the atoms must be considered another important experimental imperfection. Following the derivation in chapter 3.3.1, an uncorrelated convolution of the two atoms' detunings with a three-dimensional Boltzmann distribution was carried out to account for the effect of residual thermal excitation. Based on Equation 3.15, this yielded the following integral

[4]The single atom case is found by setting $g_2 = 0$ in equation 6.16

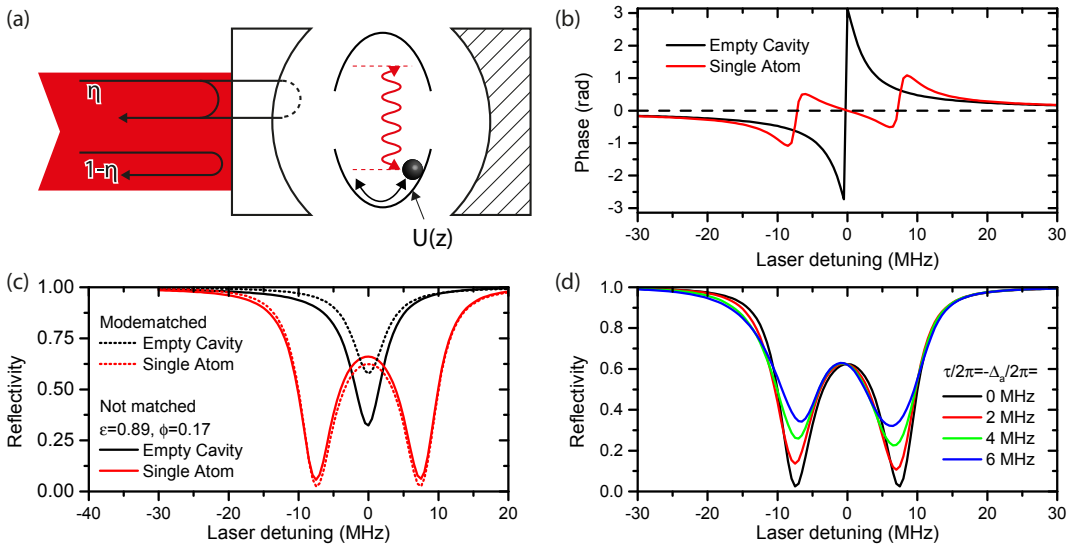

Figure 6.6.: Reflectivity of the coupled atom-cavity system (a) A fraction η of the incident field couples to the resonator, which contains a single atom. The residual thermal motion of the atom in the trapping potential $U(\vec{r})$ leads to an inhomogeneous broadening of the measured reflectivity. (b) The phase of the coupling part of the field reflected off of the cavity in the case of an empty cavity and a single atom coupled to the cavity. (c) Expected effective reflectivity in a well-coupled atom-cavity system and an imperfectly mode matched system that is described by the parameters found in Chapter 2.2. Owing to the phase difference of π on resonance of the empty cavity, the effect is more pronounced for the empty cavity. (d) Expected reflectivity of a mode-matched system containing a single atom that is inhomogeneously broadened due to residual thermal excitation. The atomic detuning $\Delta_a = -\tau$ was chosen to counteract the line shifting effect of the thermal excitation described by the temperature parameter τ (see Chapter 3.3.1).

expression for the expected reflectivity

$$R_2(\Delta, \Delta_a) = \frac{16}{\pi} \int_0^\infty \int_0^\infty |r(\Delta, \Delta_a + \tau r_1^2, \Delta_a + \tau r_2^2)|^2 r_1 r_2 e^{-r_1^2 - r_2^2} dr_1 dr_2, \quad (6.18)$$

where $\tau = \frac{\alpha_e - \alpha_g}{\alpha_g \hbar} k_B T$ measures the atomic temperature in terms of a typical shift in the atomic detuning that results from fluctuating AC Stark shifts. α_e and α_g are the polarizabilities of the excited and ground state (see Chapter 3.3.1). Thermal excitation will cause an asymmetric shift of the measured frequency-dependent reflectivity. Symmetry of the observed signal with respect to the empty cavity resonance $\Delta = 0$ can be regained by introducing a small initial atomic detuning $\Delta_a = -\tau$[5]. This is the situation that is aimed for when aligning the apparatus. Figure 6.6(d) shows numerical simulations of the reflectivity of

[5]The atoms assume this detuning only when it is located precisely at the center of the trap.

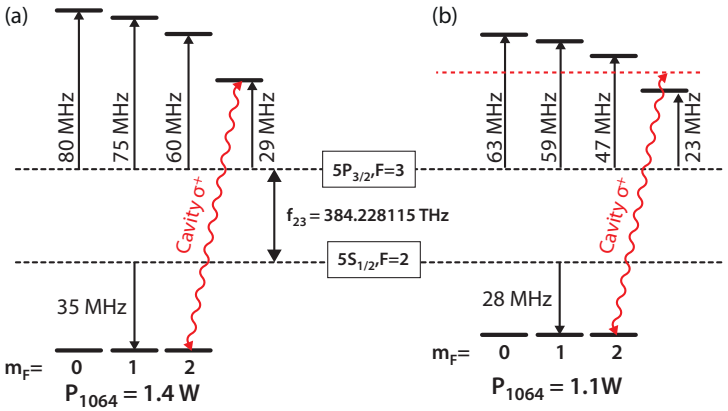

Figure 6.7.: Excited energy eigenstates (a) Energy eigenstates of the $|5S_{1/2}, F = 2\rangle$ and $|5P_{3/2}, F = 3\rangle$ manifolds for a 1064 nm trap power of $P_{1064} = 1.4\,\mathrm{W}$. At this setting of the trap power, the σ^+-polarized cavity mode is resonant with the cycling transition. During optical pumping, a single atom appearing in the coupling ground state suppresses the intracavity intensity so strongly that the second atom won't be pumped. (b) Same as (a) but for the setting of the trap power $P_{1064} = 1.1\,\mathrm{W}$ which is used during optical pumping. The cavity is no longer resonant with the cycling transition and impinging circular polarized light allows to optically pump both atoms instead of only a single atom. The light shifts in both cases depend only on $|m_F|$ and the schemes are thus symmetric (see chapter 3.2).

the single-atom cavity system for different temperatures in the case of $\Delta_a = -\tau$. The dominant remaining effect is an increased reflectivity on the normal mode resonances, while the reflectivity $R(\Delta = 0)$ at empty cavity resonance remains almost constant.

A third experimental imperfection that must be considered is non-unity efficiency of optical pumping. The theory curves in Fig. 6.6 were calculated for a coherent coupling strength of $g = 2\pi \cdot 7.84\,\mathrm{Mhz}$, which assumes a circular polarized cavity mode that interacts with the cycling transitions of ^{87}Rb. When the atom is initialized in the wrong Zeeman state, its effect is reduced to a negligible, dispersive shift of the cavity resonance (see energy structure shown in Fig. 6.8 and discussion below). This effect is modeled by assuming uncorrelated optical pumping of the two atoms described by the single-atom pumping efficiency η_{pump}. The observed reflectivity $R^1_{\mathrm{eff}}(\Delta)$ for a single atom and $R^2_{\mathrm{eff}}(\Delta)$ can then be expressed as weighted averages over the different contributions:

$$R^1_{\mathrm{eff}} = \eta_{\mathrm{pump}} R_1(\Delta) + (1 - \eta_{\mathrm{pump}}) R_{\mathrm{cav}} \quad (6.19)$$

$$R^2_{\mathrm{eff}} = \eta^2_{\mathrm{pump}} R_2(\Delta) + 2\eta_{\mathrm{pump}}(1 - \eta_{\mathrm{pump}}) R_1(\Delta) + (1 - \eta_{\mathrm{pump}})^2 R_{\mathrm{cav}} \quad (6.20)$$

where $R_1(\Delta)$ is the single-atom reflectivity (equation 6.18 with $g_2 = 0$) and $R_{\mathrm{cav}}(\Delta)$ is the empty cavity reflectivity given by equation 2.2.

Problems with optical pumping that are related to the energy structure of the excited energy eigenstates and the presence of the cavity are discussed in the following paragraph. Figure 6.8(a) shows the energy eigenvalues of the $|5S_{1/2}, F = 2, m_F\rangle$ and $|5P_{3/2}, F = 3, m_F\rangle$ states perturbed by the 1064 nm trapping light for a trap power of $P_{1064} = 1.4\,\mathrm{W}$. The cavity frequency is stabilized such that the cycling transition is resonant with the cavity for this setting of P_{1064}. The values were calculated using the theory developed in Chapter 3.2.2. In order to optically pump the atoms to the $|5S_{1/2}, F = 2, m_F = 2\rangle$ state, the cavity is excited with σ^+ polarized light that drives $\Delta m_F = +1$ transitions. Two problems for optical pumping appear. First, due to the strong tensor light shift on the excited F=3 state, some excitation pathways are highly detuned. The transition from the $m_F = -1$ ground state to the $m_F = 0$ excited state e.g. is detuned by 50 MHz, leading to a low excitation rate and a consequently high probability of the atom remaining in ground states with $m_F < 0$. The second problem was discovered during the first attempts to optically pump two atoms. Although two atoms were clearly visible on the camera images, reflection spectroscopy of the coupled system did not deviate significantly from the case of a single atom. This is a consequence of the resonance of the cavity with the cycling transitions. The first atom to appear on the cycling transition will lead to a normal mode splitting in the cavity excitation probability and the intracavity intensity will be suppressed [63] by a factor $(1 + 2C)^2$ with the cooperativity $C = g^2/2\kappa\gamma$. Thus, for the parameters of this system, the first atom leads to a seventy-fold reduction of the pumping light intensity in the resonator, which tremendously slows pumping of the second atom.

As a solution, the trap power of the 1064 nm trap was reduced to 1.1 W during the optical pumping, leading to the structure of excited energy eigenstates shown in Fig. 6.8(b). The cavity is now not resonant with any atomic transitions while the average detuning on all excitation pathways is decreased, which solved the described problem of pumping two atoms.

Figure 6.8 shows experimental data for a single atom and two atoms coupled to the cavity. Probing of reflectivity for 10 μs is preceded by 80 μs of optical pumping and followed by optical molasses cooling. This sequence is repeated at a rate of 500 Hz. The single resonance observed for the empty cavity (black dots) is clearly split up into two resonances when a single atom is coupled (red dots) corresponding to excitation of the single-atom normal modes of the coupled system. The red line is a fit to the data. The parameters $(\kappa, \kappa_{\mathrm{OC}}, \gamma) = 2\pi\cdot(2.75, 2.42, 3.03)\,\mathrm{MHz}$ and $\eta = 0.89, \phi = 0.173$ were taken from the evaluation of the empty cavity data (see Chapter 2.2). The fitted parameters were $g = 2\pi \cdot 7.62\,\mathrm{MHz}$, $\Delta_a = -2.82\,\mathrm{MHz}$, $\tau = 2.01\,\mathrm{MHz}$, and $\eta_{\mathrm{pump}} = 0.87$. The fitted value of g deviates only by 3 % from the theoretical maximum. This experimentally found value is used for all further computations. The blue line is calculated using equation 6.20 for the two-atom case with the parameters that were determined by spectroscopy of the single-atom system and the empty cavity. No further free parameters were introduced. The curves match the experimental data well (blue

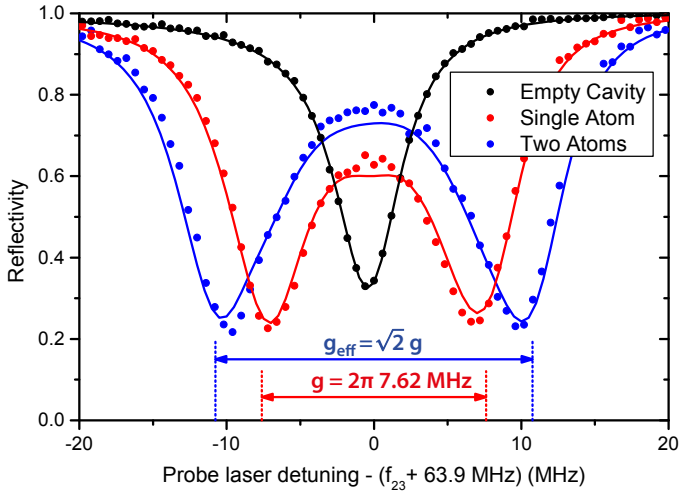

Figure 6.8.: Spectroscopy of the coupled one/two-atom-cavity system in reflection Reflectivity of the empty cavity (black dots) and the cavity containing a single (red dots) and two atoms (blue dots). The black and red lines are calculated with theoretical models and fit to the data using parameters describing the cavity itself and inhomogenous broadening of the atoms due to residual thermal excitation (see text for details) The blue line is calculated based upon the values found from the single-atom and empty cavity data without further free parameters.

dots) and an increased collective coupling strength of $g_{\text{eff}} = \sqrt{2}g = 2\pi \cdot 10.8\,\text{MHz}$ was found in the splitting of the normal modes.

6.4.2. Transversal Excitation: Single Atom

Transversal excitation experiments with a single atom in the resonator were initially carried out to calibrate the Rabi frequency of the excitation laser and on a regular basis during the data collection of the two-atom interference experiments. The results of these calibration experiments allow to monitor small changes in the alignment that manifest themselves in a different Rabi frequency of the excitation laser, or a different atomic detuning or temperature. A sketch of the experiment is shown in Fig. 6.9(a). The polarization of the excitation laser is linear perpendicular to the cavity axis. In the atomic coordinate frame, the σ^+-components of this laser thus couples to the cycling transition $|5S_{1/2}, \text{F}{=}2, m_F{=}2\rangle \leftrightarrow |5P_{3/2}, \text{F}{=}3, m_F{=}3\rangle$. It's σ^- components would drive a $\Delta m_F = -1$ transition, but this is highly unlikely due to the strong tensor light shift caused by the π-polarized dipole trap (see Fig. 6.7(b)).

Figure 6.9(b) shows the measured rate of photons as a function of the excitation laser's detuning from resonance with the cavity. The red line is a fit to the data of a single-atom model. The model is analogous to that described in Chapter 6.3.1 but extended by fluctuating atomic detuning and imperfect op-

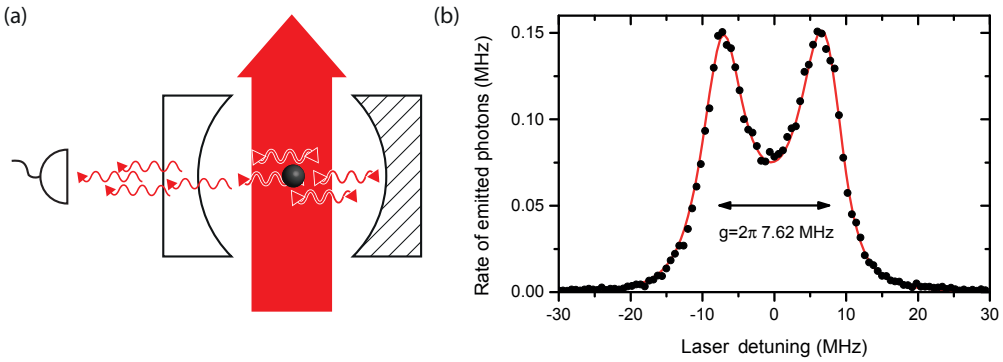

Figure 6.9.: Transversal excitation of a single atom in the cavity (a) Sketch of the scheme. A running-wave excitation laser propagates perpendicular to the cavity axis and illuminates a single atom trapped in the cavity. The excitation laser is linearly polarized perpendicular to the cavity axis with a power of 10 nW. Light emitted from the output coupling mirror is detected with single photon detectors. (b) Rate of photons emitted from the cavity versus frequency of the excitation laser. Zero on the x-axis marks the resonance of the excitation laser with the empty cavity and the bare atom.

tical pumping in the manner that was discussed in the preceding chapter. The only free parameters for fitting are the atomic detuning at the bottom of the trap $\Delta_a = -2\pi \cdot 2.41\,\mathrm{MHz}$, the atomic temperature described by the parameter $\tau = 2\pi \cdot 2.31\,\mathrm{MHz}$, and the Rabi frequency of the excitation laser $\Omega = 940\,\mathrm{kHz}$. The optical pumping efficiency $\eta_{\mathrm{pump}} = 0.89$ that was found from cavity reflection spectroscopy was used. The data agrees well with the fitted theory curve and a normal-mode splitting of the resonance is clearly visible.

The detection setup allows for polarization-sensitive detection of the emitted light (see Chapter 2.1). Insertion of a $\lambda/4$ wave plate maps circular polarizations onto the two orthogonal linear polarizations which are discriminated by the polarizing beam splitter in front of each detector pair. In this case and for the described experiment, most of the fluorescence signal emitted from the cavity appears on the detector that is sensitive to right-circular polarization. The ratio of the two signals is 1:100 and is and therefore already close to the technically limited extinction ratio of the detection setup. This polarization is expected, as the light used for initial optical pumping of the atom onto a cycling transition is right-circular polarized as well.

Experiments like the one described were performed periodically during the two-atom data collection in order to verify the system's alignment and the stability of all of the relevant parameters.

6.5. Phase Calculation

As discussed in Chapter 2.4, unambiguous single-site resolved detection of the difference vector between an atom pair was achieved. For the two-atom experiments, this technique is employed to detect the value of the relevant phase difference ϕ for every loaded atom pair. The excitation laser was carefully aligned to propagate colinearly with the 1064 nm trap beam along the x-axis. Because the 780 nm wavelength of the excitation laser is incommensurable with the spatial periodicity of the trapping potential (532 nm), ϕ will increase by an odd fraction of 2π with each additional site, by which the atom pair is separated along the x-axis. Along the z-axis, the spatial periodicity of the trapping potential ($1/2 \cdot 772\,\text{nm} = 386\,\text{nm}$) is also incommensurable with the 780 nm wavelength of the resonant intracavity mode. Yet, while the phase of the electric field of a propagating wave changes continuously and the field's amplitude is constant, the phase of a standing wave field is constant between two nodes of the light field and undergoes a discontinuous jump of π at each light node. The jump is accompanied by a zero transition of the field's amplitude. For a given atom pair with an integer number of trapping sites n_x and n_z along the x- and z-axis between them, the value of ϕ is:

$$\phi = n_z \cdot \pi + n_x \cdot \frac{532}{780} \cdot 2\pi. \tag{6.21}$$

The small non-orthogonality found in the lattice (see Chapter 2.4) does not alter the calculation of ϕ if the excitation laser propagates colinearly with the x-axis trap.

The atoms are trapped in a region along the cavity where the 772 nm mode that is used for trapping and the 780 nm mode that is held resonant with the atoms are out-of-phase. The repulsive intracavity trap thus confines the atoms to antinodes of the resonant mode. When the displacement of the atoms along the z-axis increases, this no longer holds. The beating pattern of the two modes has a spatial periodicity of 37 μm and the intensity of the mode at the trapping sites of the blue trap is modulated sinusoidally. In all of the experiments that are discussed in this chapter only loading attempts were evaluated, which resulted in atoms that were located within a region of interest that extended 6 μm along the z-axis. It was made sure in independent experiments that the center of this region of interest coincides with a maximum of the beating pattern between the two longitudinal modes. Thus, the greatest displacement of 3 μm from this maximum leads to a decrease of less than half a percent of the mode's amplitude and therefore the value of g.

Along the x-axis, the mode intensity is given by the Gaussian envelope of the cavity field with its $1/e^2$ intensity radius of $w = 29.6\,\mu$m. The evaluated region of interest extents 15 μm along the x-axis, chosen symmetrically around the center of the cavity mode. The maximum displacement of 7 μm of a single atom from

the cavity center thus leads to a maximum decrease in g of 3 %. Both effects are negligible compared to other experimental imperfections such as residual thermal excitation, which were discussed Chapter 6.4 and are neglected in the analysis of the presented experiments.

6.6. Experimental Results

Several two-atom experiments were conducted with different experimental settings. During application of the experimental sequence, the $1/e$ single-atom trapping time was $\approx 20\,\mathrm{s}$. This value is decreased by a factor of two for an atom pair, as the loss of one of the two atoms destroys the pair. Because the loading is less reliable for two atoms in comparison to a single atom, the experimental duty cycle is further reduced. Still, data was collected approximately 25 % of the available laboratory time and the experimental sequence was repeated with a rate of 0.75 kHz during that time. This resulted in a comfortable data rate that permitted frequency- and phase-resolved measurements in an acceptable time.

Figure 6.10(a) shows a sketch of the experiment. After optical pumping of the two atoms for 80 μs with a reduced trap power (see Chapter 6.4.1), the atom pair was transversally excited with a laser that was linearly polarized with its electric field oriented perpendicular to the cavity axis. Owing to the tensor light shift caused by the dipole trap, only the σ^+ component of this laser couples resonantly to the atoms' cycling transition (see Chapter 6.4.2). While the excitation laser was applied, light transmitted through the outcoupling mirror of the cavity was coupled to an optical fibre (not shown in the figure) and directed to a Hanbury-Brown and Twiss type detection setup [165]. The setup consists of a single-photon detectors behind each output port of a non-polarizing beam splitter. This setup enables simultaneous recording of the rate of emitted photons and evaluation of the $g^{(2)}(\tau)$ correlation function. Simultaneously recorded fluorescence images were used to attribute the recorded data to a certain value of the phase difference ϕ (see preceding chapter).

Figure 6.10(b) shows the data that was collected while exciting the atom pair at a Rabi frequency of $\Omega = 2\pi \cdot 300\,\mathrm{kHz}$ and scanning the detuning of the excitation laser. The atoms were kept on resonance with the cavity. The two datasets show the extreme cases of in-phase emission ($\phi = 0$) and out-of-phase emission ($\phi = \pi$). The solid lines were calculated with parameters for the residual temperature ($\tau = 2\pi \cdot 2.3\,\mathrm{MHz}$) and atomic detuning at the bottom of the trap ($\Delta_a = -2\pi \cdot 3.0\,\mathrm{MHz}$), found from independent single-atom experiments (see Chapter 6.4.2). The dashed line shows the theory curve fitted to these single-atom data. The two-atom data reproduce all features that are expected from the theoretical treatment, including the relatively small (1.2-fold) increase of emitted power when comparing the two-atom in-phase data to the single-atom data for resonant driving ($\Delta = 0$).

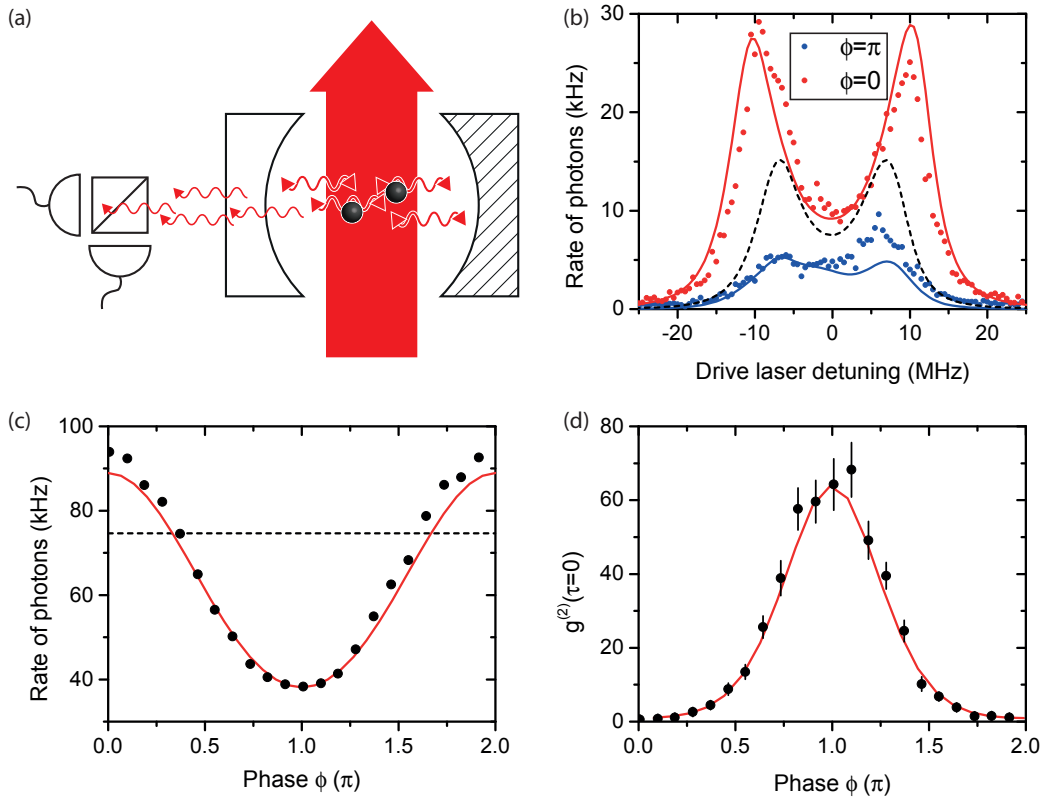

Figure 6.10.: Two-atom experiments: Intensity and fluctuations (a) Rate of photons emitted from the cavity while driving the atoms with a Rabi frequency of $\Omega = 2\pi \cdot 300\,\mathrm{kHz}$ and a variable detuning of the drive laser from the bare atoms' resonance, which coincides with the cavity resonance. The two data sets are evaluated for the out-of-phase situation $\phi = \pi$ and in-phase emission $\phi = 0$ of the two atoms. The dashed line is the fit result to a corresponding single-atom verification measurement. (b) Rate of photons emitted from the cavity as a function of the interatomic phase ϕ while driving the atoms on resonance with a Rabi frequency $\Omega = 2\pi \cdot 940\,\mathrm{kHz}$. The dashed line marks the single-atom value of 75 kHz. (c) Second-order correlation function $g^{(2)}(\tau = 0)$ recorded in the same setting as the data in panel (b). A transition from almost Poissonian to strongly super-Poissonian photon emission is visible as the phase changes from constructive interference $\phi = 0$ to destructive interference $\phi = \pi$.

Furthermore, the detunings that maximize the emitted power and mark excitation of the collective normal modes are further apart for the two-atom in-phase data compared to the single-atom data; this is consistent with cavity-reflection spectroscopy (see Chapter 6.4.1). In the out-of-phase case, the calculated theory curve strongly deviates from the numerical analysis of the perfect system (see Figure 6.3). This is mainly a consequence of imperfect optical pumping. In the majority of the cases in which optical pumping of two atoms did not

succeed, light is still emitted by one single atom. The rate of emitted photons is then by far larger as for two atoms emitting destructively and will display a normal-mode spectrum as a function of the laser frequency (see Figure 6.9(b)).

The data shown in panel (b) of Fig. 6.10 show the rate of emitted photons as a function of the phase ϕ while resonantly exciting the system. The excitation power was increased with respect to the experiments shown in panel (a) from 1 nW to 10 nW. This setting and the corresponding increased rate of photon emission permitted a measurement of the second-order correlation function in acceptable time (one week) while fulfilling $\Omega < g$ and causing negligible heating of the atoms. The dashed line at 75 kHz shows the single-atom value that was found for the same experimental circumstances in independent single-atom experiments. The red solid line was calculated with the theoretical model, using parameters found from the same single-atom experiments ($\Omega = 2\pi \cdot 940\,\mathrm{kHz}$, $\tau = 2\pi \cdot 1.9\,\mathrm{Mhz}$, $\Delta_a = -2\pi \cdot 2.6\,\mathrm{MHz}$). From the ten-fold increase in excitation power, a $\sqrt{10} = 3.2$ fold increase in the Rabi frequency is expected, which is in accordance with the measured values. The data shows a sinusoidal modulation of the emitted power as a function of the phase and is congruent with the theoretical expectation. Consistent with the data shown in panel (a), the emitted power is increased by a factor $1.25 < 4$, which is well below the simple expectation of a fourfold increase for free-space emission (see Chapter 6.3.2). For growing interference phase $\phi > 0$, the observed intensity drops below the single-atom value and assumes a non-zero minimum of 40 kHz for $\phi = \pi$.

Panel (d) of Fig. 6.10 shows the theoretical expectation (red line) and the measured value (black dots) of the second-order correlation function $g^{(2)}(\tau = 0)$. All detection events of two single-photon detectors that observed the output of two ports of a non-polarizing beam splitter (see Fig. 6.9(a)) during excitation of the atom were denoted as timestamps with an electronic resolution of 160 ps. Pairs of detection events (within one experimental shot), one of which occurred on one detector and one on the other, were evaluated by denoting their detection time difference in a table. The light path from the beam splitter to the two detectors differs by 66 cm, which is accounted for by subtracting 2.2 ns from every detected pair. As the correlation function is intrinsically symmetric, the sign of the detected pairs does not bare any physical relevance and the found values are replaced by their modulus. The registered values are subsequently binned in 2 ns wide bins and finally normalized to the expected number of pairs per bin, assuming a Poissonian distributed number of temporally uncorrelated detected photons per experimental shot. In the case of n detected photons in a particular shot, $n(n-1)$ detection time differences between photon pairs are detected. The average number of detection time differences for a Poissonian distributed number of detected photons will therefore be $\langle n(n-1)\rangle = \sum_{k=0}^{\infty} \frac{\langle n\rangle^k}{k!} e^{-\langle n\rangle} k(k-1) = \langle n\rangle^2$. The beam splitter distributes the photons randomly onto the two detectors and only pairs of photons that were registered on different detectors enter the evaluation. This procedure eliminates half of the data but avoids problems that

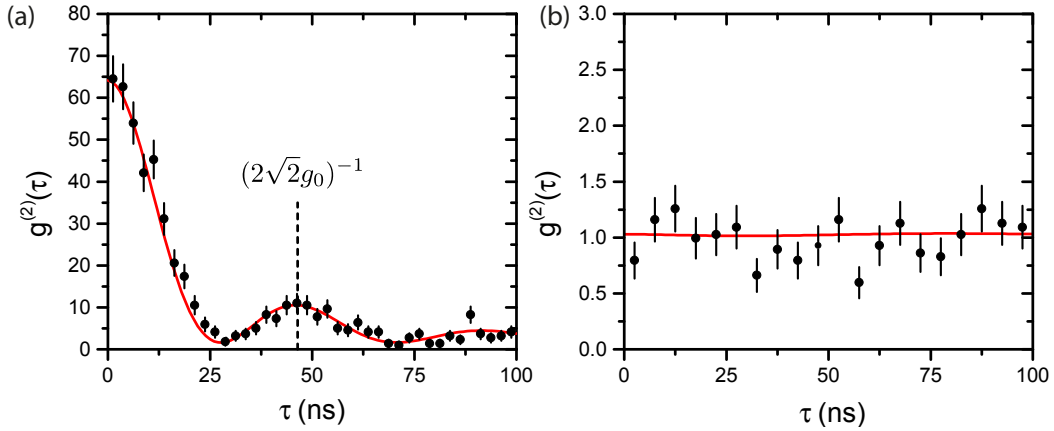

Figure 6.11.: Second-order correlation functions The second-order correlation function $g^{(2)}(\tau)$ is shown as a function of the detection-time difference (τ) for the cases of two atoms (a) emitting with opposite phases ($\phi = \pi$) and (b) emitting in-phase ($\phi = 0$). In the case of destructive interference, an oscillatory decay of the initial bunching peak $g^{(2)}(0) = 64 \pm 7$ to the uncorrelated steady-state value was observed. For in-phase emission of the atom pair, uncorrelated photon emission was observed, as expected from a coherent intracavity field.

are caused by detector dead time. The expected number of correlations is thus reduced to $\langle n \rangle^2/2$. Owing to the limited probing time T, the detection time differences are not expected to be equally distributed. It is unlikely to find two photons exactly at the boundaries of the probing time generating a data point at $\tau = (\pm)T$, whereas there are many possible realizations of a closely spaced photon pair ($\tau < T$) within the pulse. In case of a constant ensemble-averaged intensity during probing, a pyramidal envelope of the number of correlations per bin is expected, reflecting the autocorrelation function of the pulse envelope. For a total number N of experiments, the number of detection time differences (after taking the absolute value) in a bin with width w at detection time difference τ will be $(1 - \tau/T)N\langle n \rangle^2 w/(2\,T)$. As the maximum evaluated detection time difference $\tau = 100\,\text{ns}$ is small compared to the probing time $T = 5\,\mu\text{s}$, the τ-dependency of the normalization was ignored during data evaluation.

The strong dependence on the phase predicted by the theory is found in the experiment and the data agree quantitatively within error bars. For destructive interference, the light emitted from the cavity is strongly super-Poissonian with $g^{(2)}(0) = 64 \pm 7$. For in-phase emission of the atoms, build-up of an almost perfectly coherent field in the cavity is expected. A value of $g^{(2)}(0) = 0.79 \pm 0.16$ is measured. The deviation from the expected value is only $1.5\,\sigma$ and evaluating $g^{(2)}(\tau > 0)$ provided additional supporting data to rule out photon antibunching on atomic time-scales. These data will be discussed in the following.

The second-order correlation functions evaluated for detection-time differences $\tau > 0$ are shown in Fig. 6.11 for $\phi{=}\pi$ in panel (a) and $\phi{=}0$ in panel (b) to-

gether with the theoretical expectation (red lines). In the out-of-phase emission, the rapid oscillatory decay of the initial peak that is predicted by theory is reproduced well by the data. A second maximum was found at $(2\sqrt{2}\,g)^{-1} = 46\,\mathrm{ns}$. As discussed above, this can be interpreted in a particle- or wave-like manner. It can either be seen as the first maximum in the beating pattern of emission from the two normal modes, or as the single photon that remains in the cavity after emission of a first photon undergoing one full cycle of collective vacuum Rabi oscillations. The theoretical expectation in the case of $\phi = 0$ is hardly distinguishable from a perfectly constant function indicating absolutely uncorrelated emission. Within error bars, the data agrees with this expectation. The fact that the correlation functions in both cases do not settle to $g^{(2)}(\tau \to \infty) = 1$ is supported by the theory. It is a consequence of the ensemble average over different realizations of the same experiment, each of which is performed with a different realization of fluctuating parameters, such as atom position and success of optical pumping. This leads to an intrinsic bunching that is not associated with any time-scale.

7. Summary and Outlook

Throughout this thesis project full experimental control over a pair of atoms that are permanently coupled to the single mode of a miniaturized Fabry-Perot resonator was achieved. A mechanism to isolate exactly two atoms from a random initial sample was implemented. Moreover, a two-dimensional optical lattice in combination with single-site resolved imaging of the atom pair allowed exact determination of the atoms' relative spatial position. Breakdown of the atomic hyperfine structure caused by the dipole trap was experimentally observed. A technique to measure the population of individual motional eigenstates of the trapping potential was developed. This topic transcends characterization measurements and was presented as a self-contained chapter. An outlook for future research opportunities made possible by these findings was given in this chapter.

The achieved single-site resolution allows measurement of the relative optical phases that appear when the atom pair is driven with a laser that is propagating transversally through the resonator. In a scattering experiment, light emitted from the resonator was observed as a function of the optical phases, with which the atoms couple to the cavity mode and a transversal excitation laser. In this experimental setup, the excitation laser in dependency of the phase difference couples the system's ground state to states that are symmetric or antisymmetric with respect to the exchange of atoms. Emission of coherent light and a weak dependency of the emission power on the number of atoms was found when atomic symmetric states were excited and the atoms correspondingly emitted constructively into the cavity mode. Excitation of atomic antisymmetric states leads to reduced, though non-zero, light emission. In contrast to the uncorrelated photon emission observed for constructive interference, antisymmetric excitation and therefore destructive emission was characterized by huge photon bunching.

It is precisely these differences in the radiative behaviour of atomic symmetric and antisymmetric states which are at the heart of many theoretical proposals that are relevant for *quantum information processing*. Kastoryano et al. proposed an experimental scheme for dissipative preparation of entangled states between two atoms embedded in an optical cavity [41]. In this scheme, application of a single optical pumping field drives the atoms into a maximally entangled steady state that is realized in the atoms' ground state manifolds. The entangled state is then made available by simply switching off the light whenever needed, e.g. in a quantum repeater scheme [166]. The underlying Tavis-Cummings dynamics has been simulated on an ion-trap apparatus in David Wineland's group [167], yet its realization in the optical domain remains an open goal. The

experimental techniques developed and characterized in this thesis provide all the necessary building blocks.

Instead of the expectation value and fluctuation of emitted light's intensity that were observed in this thesis, field quadratures of the emitted light could be recorded as a function of the phase between the atoms. The huge photon bunching that was observed for destructive interference, i.e. excitation via atomic antisymmetric states, was explained as a consequence of excitation to a doubly excited state, followed by photon-pair emission. Also for higher rungs of the Tavis-Cummings ladder of states it remains true that the antisymmetric excitation pathway excites only energy eigenstates with an even number of photons. This excitation pathway can thus lead to squeezed-vacuum states of the cavity field. This topic has been covered in theory [17, 32, 33] and the only addition to the apparatus required is a homodyne-detection setup.

The possibility to trap and control several atoms as stationary quantum bits coupled to the single light mode of a cavity as a shared resource is a prototypical system for quantum information processing. Quantum computer architectures and quantum logic gates [35, 38–40] have been proposed. The required control over single atoms without illuminating other atoms can be provided by the optical addressing system that was implemented; for the experiments reported in this thesis this system was only used to resonantly excite atoms and remove them from the trap. Initial experiments that aim to extend an already demonstrated quantum memory process [78] to multiple atoms were conducted and promising results were found.

A. Reduced Matrix Elements

Transition	**Wavelength**	$\langle nJ\|\|d\|\|n'J'\rangle/(ea_0)$	**Reference**
$5S_{1/2} \rightarrow 5P_{1/2}$	794.7603 nm	2.992	[168]
$5S_{1/2} \rightarrow 5P_{3/2}$	780.0268 nm	4.225	[168]
$5S_{1/2} \rightarrow 6P_{1/2}$	421.5524 nm	0.2356	[168]
$5S_{1/2} \rightarrow 6P_{3/2}$	420.1792 nm	0.3601	[168]
$5S_{1/2} \rightarrow 7P_{1/2}$	359.1572 nm	0.08132	[168]
$5S_{1/2} \rightarrow 7P_{3/2}$	358.705 nm	0.1344	[168]
$5S_{1/2} \rightarrow 8P_{1/2}$	335.0812 nm	0.04069	[168]
$5S_{1/2} \rightarrow 8P_{3/2}$	334.8696 nm	0.07129	[168]
$5S_{1/2} \rightarrow 9P_{1/2}$	322.9156 nm	0.02527	[168]
$5S_{1/2} \rightarrow 9P_{3/2}$	322.7979 nm	0.04611	[168]
$5S_{1/2} \rightarrow 10P_{1/2}$	315.8259 nm	0.01768	[168]
$5S_{1/2} \rightarrow 10P_{3/2}$	315.7530 nm	0.03242	[168]
$5P_{1/2} \rightarrow 4D_{3/2}$	1475.64 nm	5.684	[169]
$5P_{1/2} \rightarrow 6S_{1/2}$	1323.88 nm	2.932	[169]
$5P_{1/2} \rightarrow 7S_{1/2}$	728.2 nm	0.674	[169]
$5P_{1/2} \rightarrow 7D_{3/2}$	564.93 nm	0.564	[169]
$5P_{1/2} \rightarrow 8S_{1/2}$	607.24 nm	0.355	[169]
$5P_{1/2} \rightarrow 8D_{3/2}$	536.41 nm	0.433	[169]
$5P_{3/2} \rightarrow 4D_{3/2}$	1529.26 nm	1.814	[169]
$5P_{3/2} \rightarrow 4D_{5/2}$	1529.37 nm	5.445	[169]
$5P_{3/2} \rightarrow 5D_{3/2}$	776 nm	0.333	[170]
$5P_{3/2} \rightarrow 5D_{5/2}$	776 nm	0.992	[170]
$5P_{3/2} \rightarrow 6S_{1/2}$	1366.87 nm	3.025	[169]
$5P_{3/2} \rightarrow 6D_{3/2}$	630 nm	0.253	[170]
$5P_{3/2} \rightarrow 6D_{5/2}$	630 nm	0.756	[170]
$5P_{3/2} \rightarrow 7S_{1/2}$	741.02 nm	0.675	[169]
$5P_{3/2} \rightarrow 7D_{3/2}$	572.62 nm	0.187	[169]
$5P_{3/2} \rightarrow 7D_{5/2}$	572.57 nm	0.559	[169]
$5P_{3/2} \rightarrow 8S_{1/2}$	616.13 nm	0.353	[169]
$5P_{3/2} \rightarrow 8D_{3/2}$	543.33 nm	0.143	[169]
$5P_{3/2} \rightarrow 8D_{5/2}$	543.3 nm	0.427	[169]
$5P_{3/2} \rightarrow 9S_{1/2}$	566 nm	0.233	[170]
$5P_{3/2} \rightarrow 9D_{3/2}$	526 nm	0.113	[170]
$5P_{3/2} \rightarrow 9D_{5/2}$	526 nm	0.336	[170]
$5P_{3/2} \rightarrow 10S_{1/2}$	539 nm	0.171	[170]

B. 1D Lattice Calculation

The derivation is carried out following the treatment in [171]. The result will be an energy spectrum that is parametrized by a discrete band index n and a continuous quasi-momentum q. The potential is denoted as

$$U(x) = -U_0 \cos(k\,x)^2 = \frac{-U_0}{2} - \frac{1}{4}e^{i2kx} - \frac{1}{4}e^{-i2kx}$$

where k is the wave vector of the light used to generate the periodic potential. The generated dipole potential has twice the periodicity. To find the eigenstates, the following ansatz is chosen that factorizes into a plain wave with momentum q and a lattice-periodic function $u_q^{(n)}(x) = u_q^{(n)}(x + \pi/k)$

$$\Psi_q^{(n)}(x) = e^{\frac{iqx}{\hbar}} u_q^{(n)}(x)$$

Introducing this ansatz into the Hamiltonian yields

$$H_B u_q^{(n)}(x) = E_q^{(n)} u_q^{(n)}(x) \qquad \text{with} \qquad H_B = \frac{1}{2m}(p+q)^2 + U(x)$$

The potential $U(x) = \sum_r U_r e^{i2rkx}$ and $u_q^{(n)} = \sum_l c_l^{(n,q)} e^{i2lkx}$ are epxressed as Fourier series. The potential's Fourier coefficients are given by the definition of the potential $U_{-1} = U_1 = \frac{1}{4}$, $U_0 = -\frac{1}{2}U_0$. Inserting this into the Hamiltonian yields:

$$\begin{aligned}
\text{pot. energy: } U(x)u_q^{(n)}(x) &= \sum_{l,r} c_l^{(n,q)} U_r e^{i2(r+l)kx} \\
&= \sum_l c_l^{(n,q)} U_0 \left(-\frac{1}{2}e^{i2lkx} - \frac{1}{4}e^{i2(l-1)kx} - \frac{1}{4}e^{i2(l+1)kx} \right) \\
\text{kin. energy: } \frac{(p+q)^2}{2m} u_q^{(n)} &= \sum_l \frac{(2\hbar kl + q)^2}{2m} c_l^{(n,q)} e^{i2lkx}
\end{aligned}$$

This is a recursive expression for the Fourier coefficients of the solution, which may be expressed as an eigenvalue problem:

$$\sum_{l'} H_{l,l'} c_{l'}^{(n,q)} = E_q^{(n)} c_l \quad \text{with} \quad H_{l,l'} = \begin{cases} -\frac{1}{2}U_0 + \frac{2\hbar kl+q)^2}{2m} & l = l' \\ -\frac{1}{4}U_0 & |l - l'| = 1 \\ 0 & \text{else} \end{cases}$$

Bibliography

[1] M. Planck. Zur Theorie des Gesetzes der Energieverteilung im Normalspektrum. *Verhandlungen der deutschen physikalischen Gesellschaft* **2**(17), 237–245 (1900).

[2] A. Einstein. Über einen die Erzeugung und Verwandlung des Lichtes betreffenden heuristischen Gesichtspunkt. *Annalen der Physik* **17**, 132–148 (1905).

[3] T. H. Maiman. Stimulated Optical Radiation in Ruby. *Nature* **187**, 493–494 (1960).

[4] B. Mollow. Power Spectrum of Light Scattered by Two-Level Systems. *Phys. Rev.* **188**(5), 1969–1975 (1969).

[5] H. J. Carmichael and D. F. Walls. A Quantum-Mechanical Master Equation Treatment of the Dynamical Stark Effect. *J. Phys. B: Atom. Molec. Phys.* **9**(8), 1199–1219 (1976).

[6] D. F. Walls and P. Zoller. Reduced Quantum Fluctuations in Resonance Fluorescence. *Phys. Rev. Lett.* **47**(10), 709–711 (1981).

[7] F. Schuda, C. R. Stroud, and M. Hercher. Observation of the Resonant Stark Effect at Optical Frequencies. *J. Phys. B.* **7**(7), 198–202 (1974).

[8] F. Y. Wu, R. E. Grove, and S. Ezekiel. Investigation of the Spectrum of Resonance Fluorescence Induced by a Monochromatic Field. *Phys. Rev. Lett.* **35**(21), 1426–1429 (1975).

[9] F. Diedrich and H. Walther. Nonclassical Radiation of a Single Stored Ion. *Phys. Rev. Lett.* **58**(3), 203–206 (1987).

[10] C. H. H. Schulte, J. Hansom, A. E. Jones, C. Matthiesen, C. Le Gall, and M. Atatüre. Quadrature Squeezed Photons From a Two-Level System. *Nature* **525**, 222–225 (2015).

[11] W. Neuhauser, M. Hohenstatt, P. E. Toschek, and H. Dehmelt. Localized Visible Ba+ Mono-Ion Oscillator. *Phys. Rev. A* **22**(3), 1137–1140 (1980).

[12] J. C. Bergquist, R. G. Hulet, W. M. Itano, and D. J. Wineland. Observation of Quantum Jumps in a Single Atom. *Phys. Rev. Lett.* **57**(14), 1699–1702 (1986).

[13] W. Nagourney, J. Sandberg, and H. Dehmelt. Shelved Optical Electron Amplifier: Observation of Quantum Jumps. *Phys. Rev. Lett.* **56**(26), 2797–2799 (1986).

[14] T. Sauter, W. Neuhauser, R. Blatt, and P. E. Toschek. Observation of Quantum Jumps. *Phys. Rev. Lett.* **57**(14), 1696–1698 (1986).

[15] T. Young. The Bakerian Lecture: On the Theory of Ligght and Colours. *Phil. Trans. R. Soc. Lond.* **92**, 12–48 (1802).

[16] L. Mandel. Photon Interference and Correlation Effects Produced by Independent Quantum Sources. *Phys. Rev. A* **28**(2), 929–943 (1983).

[17] W. Vogel and D. G. Welsch. Squeezing Pattern in Resonance Fluorescence from a Regular N-Atom System. *Phys. Rev. Lett.* **54**(16), 1802–1805 (1985).

[18] T. Richter. Interference Between the Resonance Fluorescence Fields from Two Independent Atoms and Spatial Two-Photon Correlations. *Opt. Commun.* **80**(3), 285–294 (1991).

[19] T. G. Rudolph, Z. Ficek, and B. J. Dalton. Two-Atom Resonance Fluorescence in Running-and Standing-Wave Laser Fields. *Phys. Rev. A* **52**(1), 636–656 (1995).

[20] T. Rudolph and Z. Ficek. Interference Pattern with a Dark Center From Two Atoms Driven by a Coherent Laser Field. *Phys. Rev. A* **58**(1), 748–751 (1998).

[21] C. Skornia, J. von Zanthier, G. S. Agarwal, E. Werner, and H. Walther. Nonclassical Interference Effects In The Radiation From Coherently Driven Uncorrelated Atoms. *Phys. Rev. A* **64**(6), 063801 (2001).

[22] C. Schoen and A. Beige. An Analysis of a Two-Atom Double-Slit Experiment Based on Environment-Induced Measurements. *Phys. Rev. A* **64**(2), 023806 (2001).

[23] G. S. Agarwal, J. von Zanthier, C. Skornia, and H. Walther. Intensity-Intensity Correlations as a Probe of Interferences under Conditions of Noninterference in the Intensity. *Phys. Rev. A* **65**(5), 053826 (2002).

[24] J. Von Zanthier, T. Bastin, and G. S. Agarwal. Measurement-Induced Spatial Modulation of Spontaneous Decay and Photon Arrival Times. *Phys. Rev. A* **74**(6), 061802 (2006).

[25] L. L. Jin, M. Macovei, S. Q. Gong, C. H. Keitel, and J. Evers. Squeezing in Strong Light Scattered by a Regular Structure of Atoms. *Opt. Commun.* **283**(5), 790–794 (2010).

[26] P. Grünwald and W. Vogel. Entanglement in Atomic Resonance Fluorescence. *Phys. Rev. Lett.* **104**(23), 233602 (2010).

[27] U. Eichmann, J. C. Bergquist, J. J. Bollinger, J. M. Gilligan, W. M. Itano, D. J. Wineland, and M. G. Raizen. Youngs Interference Experiment with Light Scattered from Two Atoms. *Phys. Rev. Lett.* **70**(16), 2359–2362 (1993).

[28] R. DeVoe and R. Brewer. Observation of Superradiant and Subradiant Spontaneous Emission of Two Trapped Ions. *Phys. Rev. Lett.* **76**(12), 2049–2052 (1996).

[29] P. Kochan, H. J. Carmichael, P. R. Morrow, and M. G. Raizen. Mutual Coherence and Interference in Resonance Fluorescence. *Phys. Rev. Lett.* **75**(1), 45–48 (1995).

[30] G. M. Meyer and G. Yeoman. Cavity-Induced Interference Pattern with Dark Center from Two Fluorescing Atoms. *Phys. Rev. Lett.* **79**(14), 2650–2653 (1997).

[31] S. Zippilli, G. Morigi, and H. Ritsch. Suppression of Bragg Scattering by Collective Interference of Spatially Ordered Atoms with a High-Q Cavity Mode. *Phys. Rev. Lett.* **93**(12), 123002 (2004).

[32] S. Fernández-Vidal, S. Zippilli, and G. Morigi. Nonlinear Optics with Two Trapped Atoms. *Phys. Rev. A* **76**(5), 053829 (2007).

[33] H. Habibian, S. Zippilli, and G. Morigi. Quantum Light by Atomic Arrays in Optical Resonators. *Phys. Rev. A* **84**(3), 033829 (2011).

[34] H. Habibian, S. Zippilli, F. Illuminati, and G. Morigi. Stationary Entanglement of Photons and Atoms in a High-Finesse Resonator. *Phys. Rev. A* **89**(2), 023832 (2014).

[35] T. Pellizzari, S. A. Gardiner, J. I. Cirac, and P. Zoller. Decoherence, Continuous Observation, and Quantum Computing: A Cavity QED Model. *Phys. Rev. Lett.* **75**(21), 3788–3791 (1994).

[36] E. Solano, G. S. Agarwal, and H. Walther. Strong-Driving-Assisted Multipartite Entanglement in Cavity QED. *Phys. Rev. Lett.* **90**(2), 027903 (2003).

[37] H. Nihira and C. Stroud. Steady-State Two-Atom Entanglement in a Pumped Cavity. *Phys. Rev. A* **80**(4), 042329 (2009).

[38] J. Pachos and H. Walther. Quantum Computation with Trapped Ions in an Optical Cavity. *Phys. Rev. Lett.* **89**(18), 187903 (2002).

[39] L.-M. Duan and H. J. Kimble. Efficient Engineering of Multiatom Entanglement through Single-Photon Detections. *Phys. Rev. Lett.* **90**(25), 253601 (2003).

[40] L.-M. Duan, B. Wang, and H. J. Kimble. Robust Quantum Gates on Neutral Atoms with Cavity-Assisted Photon Scattering. *Phys. Rev. A* **72**(3), 032333 (2005).

[41] M. J. Kastoryano, F. Reiter, and A. S. Sørensen. Dissipative Preparation of Entanglement in Optical Cavities. *Phys. Rev. Lett.* **106**(9), 090502 (2011).

[42] F. Reiter, M. J. Kastoryano, and A. S. Sørensen. Driving Two Atoms in an Optical Cavity into an Entangled Steady State using Engineered Decay. *New. J. Phys.* **14**(5), 053022 (2012).

[43] G. R. Guthöhrlein, M. Keller, K. Hayasaka, W. Lange, and H. Walther. A Single Ion as a Nanoscopic Probe of an Optical Field. *Nature* **414**, 49–51 (2001).

[44] B. Casabone, K. Friebe, B. Brandstätter, K. Schüppert, R. Blatt, and T. E. Northup. Enhanced Quantum Interface with Collective Ion-Cavity Coupling. *Phys. Rev. Lett* **114**(2), 023602 (2015).

[45] R. Reimann, W. Alt, T. Kampschulte, T. Macha, L. Ratschbacher, N. Thau, S. Yoon, and D. Meschede. Cavity-Modified Collective Rayleigh Scattering of Two Atoms. *Phys. Rev. Lett.* **114**(2), 023601 (2015).

[46] S. Chu. The Manipulation of Neutral Particles. *Rev. Mod. Phys.* **70**(3), 685–706 (1998).

[47] W. D. Phillips. Laser Cooling and Trapping of Neutral Atoms. *Rev. Mod. Phys.* **70**(3), 721–741 (1998).

[48] C. Cohen-Tannoudji. Manipulating Atoms with Photons. *Rev. Mod. Phys.* **70**(3), 707–719 (1998).

[49] H. J. Kimble. Strong Interactions of Single Atoms and Photons in Cavity QED. *Phys. Scripta* **T76**, 127–137 (1998).

[50] M. G. Raizen, L. A. Orozco, M. Xiao, T. L. Boyd, and H. J. Kimble. Squeezed-State Generation by the Normal Modes of a Coupled System. *Phys. Rev. Lett.* **59**(2), 198–201 (1987).

[51] R. J. Thompson, G. Rempe, and H. J. Kimble. Observation of Normal-Mode Splitting for an Atom in an Optical Cavity. *Phys. Rev. Lett.* **68**(8), 1132–1135 (1992).

[52] A. Kuhn, M. Hennrich, and G. Rempe. Deterministic Single-Photon Source for Distributed Quantum Networking. *Phys. Rev. Lett.* **89**(6), 067901 (2002).

[53] T. Legero, T. Wilk, M. Hennrich, G. Rempe, and A. Kuhn. Quantum Beat of Two Single Photons. *Phys. Rev. Lett.* **93**(7), 070503 (2004).

[54] T. Wilk, S. C. Webster, A. Kuhn, and G. Rempe. Single-Atom Single-Photon Quantum Interface. *Science* **317**(5837), 488–490 (2007).

[55] J. McKeever, J. R. Buck, A. D. Boozer, A. Kuzmich, H.-C. Nägerl, D. M. Stamper-Kurn, and H. J. Kimble. State-Insensitive Cooling and Trapping of Single Atoms in an Optical Cavity. *Phys. Rev. Lett.* **90**(13), 133602 (2003).

[56] S. Nußmann, M. Hijlkema, B. Weber, F. Rohde, G. Rempe, and A. Kuhn. Submicron Positioning of Single Atoms in a Microcavity. *Phys. Rev. Lett.* **95**(17), 173602 (2005).

[57] J. Bochmann, *Coherent Dynamics and State Detection of Single Atoms in a Cavity*, Phd thesis, TU München (2010).

[58] M. Mücke, *Elektromagnetisch induzierte Transparenz mit einem einzelnen Atom*, Phd thesis, TU München (2011).

[59] C. Hahn, *Remote Entanglement of Two Single Atoms*, Phd thesis, TU München (2014).

[60] G. M. Langfahl-Klabes, *Aufbau eines Experimentes zum Fangen kalter Atome in einem optischen Resonator ultrahoher Finesse*, Diploma thesis, LMU München (2006).

[61] S. Nußmann, *Kühlen und Positionieren eines Atoms in einem optischen Resonator*, Phd thesis, Technische Universität München (2006).

[62] A. Kochanke, *A High Resolution Optical System for Imaging and Addressing of Single Atoms*, Master thesis, Technische Universität München (2012).

[63] N. Kalb, *Heralded Storage of Photonic Polarization in a Single Atom*, Master thesis, TU München (2014).

[64] E. D. Black. An Introduction to PoundDreverHall Laser Frequency Stabilization. *Am. J. Phys.* **69**(1), 79–87 (2001).

[65] J. Gallego, S. Ghosh, S. K. Alavi, W. Alt, M. Martinez-Dorantes, D. Meschede, and L. Ratschbacher. High Finesse Fiber Fabry-Perot Cavities: Stabilization and Mode Matching Analysis. *arXiv:1508.05289* (2015), e-print `1508.05289`.

[66] D. A. Shaddock, M. B. Gray, and D. E. McClelland. Frequency Locking a Laser to an Optical Cavity by Use of Spatial Mode Interference. *Opt. Lett.* **24**(21), 1499–1501 (1999).

[67] R. Gutteres, C. Amiot, A. Fioretti, C. Gabbbanini, M. Mazzoni, and O. Dulieu. Determination of the 87Rb 5P State Dipole Matrix Element and Radiative Lifetime from the Phoassociation Spectroscopy of the Rb2 0g-(P3/2) Long-Range State. *Phys. Rev. A* **66**(2), 024502 (2002).

[68] B. Weber, *Distribution of Quantum Information Between an Atom and Two Photons*, Phd thesis, Technische Univerisität München (2008).

[69] C. Weitenberg, M. Endres, J. F. Sherson, M. Cheneau, P. Schauss, T. Fukuhara, I. Bloch, and S. Kuhr. Single-Spin Addressing in an Atomic Mott insulator. *Nature* **471**, 319–324 (2011).

[70] D. Schrader, I. Dotsenko, M. Khudaverdyan, Y. Miroshnychenko, A. Rauschenbeutel, and D. Meschede. Neutral Atom Quantum Register. *Phys. Rev. Lett.* **93**(15), 150501 (2004).

[71] H. Specht, *Einzelatom-Quantenspeicher für Polarisations-Qubits*, Phd thesis, TU München (2010).

[72] J. F. Sherson, C. Weitenberg, M. Endres, M. Cheneau, I. Bloch, and S. Kuhr. Single-Atom-Resolved Fluorescence Imaging of an Atomic Mott Insulator. *Nature* **467**, 68–72 (2010).

[73] M. Karski, L. Förster, J. Choi, W. Alt, A. Widera, and D. Meschede. Nearest-Neighbor Detection of Atoms in a 1D Optical Lattice by Fluorescence Imaging. *Phys. Rev. Lett.* **102**(5), 053001 (feb 2009).

[74] S. Bize, Y. Sortais, M. S. Santos, C. Mandache, A. Clairon, and C. Salomon. High-accuracy Measurement of the 87Rb Ground-State Hyperfine Splitting in an Atomic Fountain. *Europhys. Lett.* **45**(5), 558–564 (1999).

[75] A. Fuhrmanek, R. Bourgain, Y. R. P. Sortais, and A. Browaeys. Free-Space Lossless State Detection of a Single Trapped Atom. *Phys. Rev. Lett.* **106**(13), 133003 (2011).

[76] J. Volz, R. Gehr, G. Dubois, J. Estève, and J. Reichel. Measurement of the Internal State of a Single Atom Without Energy Exchange. *Nature* **475**, 210–213 (2011).

[77] J. Bochmann, M. Mücke, C. Guhl, S. Ritter, G. Rempe, and D. L. Moehring. Lossless State Detection of Single Neutral Atoms. *Phys. Rev. Lett.* **104**(20), 203601 (may 2010).

[78] H. P. Specht, C. Nölleke, A. Reiserer, M. Uphoff, E. Figueroa, S. Ritter, and G. Rempe. A Single-Atom Quantum Memory. *Nature* **473**, 190–193 (2011).

[79] A. D. Boozer. Theory of Raman Transitions in Cavity QED. *Phys. Rev. A* **78**(3), 033406 (2008).

[80] R. Han, H. K. Ng, and B.-G. Englert. Raman Transitions without Adiabatic Elimination: A Simple and Accurate Treatment. *Journal of Modern Optics* **60**(4), 255–265 (2013).

[81] A. M. Kaufman, B. J. Lester, and C. A. Regal. Cooling a Single Atom in an Optical Tweezer to its Quantum Ground State. *Phys. Rev. X* **2**(4), 041014 (2012).

[82] A. Reiserer, S. Ritter, and G. Rempe. Nondestructive Detection of an Optical Photon. *Science* **342**(6164), 1349–1351 (2013).

[83] A. D. Boozer, A. Boca, R. Miller, T. E. Northup, and H. J. Kimble. Cooling to the Ground State of Axial Motion for One Atom Strongly Coupled to an Optical Cavity. *Phys. Rev. Lett.* **97**(8), 083602 (2006).

[84] A. Reiserer, C. Nölleke, S. Ritter, and G. Rempe. Ground-State Cooling of a Single Atom at the Center of an Optical Cavity. *Phys. Rev. Lett.* **110**(22), 223003 (may 2013).

[85] J. D. Thompson, T. G. Tiecke, A. S. Zibrov, V. Vuletić, and M. D. Lukin. Coherence and Raman Sideband Cooling of a Single Atom in an Optical Tweezer. *Phys. Rev. Lett.* **110**(13), 133001 (2013).

[86] R. Reimann, W. Alt, T. Macha, D. Meschede, N. Thau, S. Yoon, and L. Ratschbacher. Carrier-Free Raman Manipulation of Trapped Neutral Atoms. *New. J. Phys.* **16**(11), 113042 (2014).

[87] R. Grimm, M. Weidemüller, and Y. B. Ovchinnikov. Optical Dipole Traps for Neutral Atoms. *Adv. At. Mol. Opt. Phys.* **42**, 95–170 (2000).

[88] S. Chu, J. E. Bjorkholm, A. Ashkin, and A. Cable. Experimental Observation of Optically Trapped Atoms. *Phys. Rev. Lett.* **57**(3), 314–317 (1986).

[89] P. S. Jessen. Optical Lattices. *Adv. At. Mol. Opt. Phys.* **37**, 95–138 (1996).

[90] B. Bransden and C. Joachain, *Physics of Atoms and Molecules* (Prentice-Hall, 2003) 2nd ed.

[91] P. Rosenbusch, S. Ghezali, V. Dzuba, V. Flambaum, K. Beloy, and A. Derevianko. AC Stark Shift of the Cs Microwave Atomic Clock Transitions. *Phys. Rev. A* **79**(1), 013404 (2009).

[92] F. Le Kien, P. Schneeweiss, and A. Rauschenbeutel. Dynamical Polarizability of Atoms in Arbitrary Light Fields: General Theory and Application to Cesium. *EPJ D* **67**(5), 1–16 (2013).

[93] Simon Elias Baur, *A Single-Photon Switch and Transistor based on Rydberg Blockade*, Phd, TU München (2014).

[94] W. R. Johnson, D. Kolb, and K.-N. Huang. Electric-Dipole, Quadrupole, And Magnetic-Dipole Susceptibilities and Shielding Factors For Closed-Shell Ions Of the He,Ne,Ar,Ni,Kr,Pb and Xe Isoelectronic Sequences. *Atom. Data Nucl. Data* **28**(2), 333–340 (1983).

[95] W. D. Hall and J. C. Zorn. Measurement of Alkali-Metal Polarizabilities by Deflection of a Velocity-Selected Atomic Beam. *Phys. Rev. A* **10**(4), 1141–1144 (1974).

[96] B. Arora and B. K. Sahoo. State-insensitive Trapping of Rb Atoms: Linearly versus Circularly Polarized Light. *Phys. Rev. A* **86**(3), 033416 (2012).

[97] M. Safronova. Private Communication.

[98] L. Armstrong, *Theory of the Hyperfine Structure of Free Atoms* (Wiley-Interscience, 1971).

[99] J. Mitroy, M. S. Safronova, and C. W. Clark. Theory and Applications of Atomic and Ionic Polarizabilities. *J. Phys. B* **43**(20), 202001 (2010).

[100] D. A. Steck. Rubidium 87 D Line Data 2.1.4, 2010.

[101] J. Ye, H. J. Kimble, and H. Katori. Quantum State Engineering and Precision Metrology Using State-Insensitive Light Traps. *Science* **320**(5884), 1734–1738 (2008).

[102] M. K. Tey, Z. Chen, S. A. Aljunid, B. Chng, F. Huber, G. Maslennikov, and C. Kurtsiefer. Strong Interaction Between Light and a Single Trapped Atom Without the Need for a Cavity. *Nat. Phys.* **4**(12), 924–927 (2008).

[103] C.-Y. Shih and M. S. Chapman. Nondestructive Light-Shift Measurements of Single Atoms in Optical Dipole Traps. *Phys. Rev. A* **87**(6), 063408 (jun 2013).

[104] M. Abramowitz and I. A. Stegun, *Handbook of Mathematical Functions* (National Bureau of Standards, Washington, D.C., 1972) 10 ed.

[105] A. Neuzner, M. Körber, S. Dürr, G. Rempe, and S. Ritter. Breakdown of Atomic Hyperfine Coupling in a Deep Optical-Dipole Trap. *Phys. Rev. A* **92**(5), 053842 (2015).

[106] G. P. Barwood, P. Gill, and W. R. C. Rowley. Frequency Measurements on Optically Narrowed Rb-stabilised Laser Diodes at 780 nm and 795 nm. *Appl. Phys. B* **53**(3), 142–147 (1991).

[107] A. Banerjee, D. Das, and V. Natarajan. Absolute Frequency Measurements of the D1 Lines in 39K, 85Rb and 87Rb with 0.1ppb Uncertainty. *Europhys. Lett.* **65**(2), 172–178 (2004).

[108] J. Bochmann, M. Mücke, G. Langfahl-Klabes, C. Erbel, B. Weber, H. P. Specht, D. L. Moehring, and G. Rempe. Fast Excitation and Photon Emission of a Single-Atom-Cavity System. *Phys. Rev. Lett.* **101**(22), 223601 (2008).

[109] M. Mücke, E. Figueroa, J. Bochmann, C. Hahn, K. Murr, S. Ritter, C. J. Villas-Boas, and G. Rempe. Electromagnetically Induced Transparency with Single Atoms in a Cavity. *Nature* **465**, 755–758 (2010).

[110] S. Ritter, C. Nölleke, C. Hahn, A. Reiserer, A. Neuzner, M. Uphoff, M. Mücke, E. Figueroa, J. Bochmann, and G. Rempe. An Elementary Quantum Network of Single Atoms in Optical Cavities. *Nature* **484**, 195–200 (2012).

[111] M. Mücke, J. Bochmann, C. Hahn, A. Neuzner, C. Nölleke, A. Reiserer, G. Rempe, and S. Ritter. Generation of Single Photons from an Atom-Cavity System. *Phys. Rev. A* **87**(6), 063805 (2013).

[112] C. Nölleke, A. Neuzner, A. Reiserer, C. Hahn, G. Rempe, and S. Ritter. Efficient Teleportation Between Remote Single-Atom Quantum Memories. *Phys. Rev. Lett.* **110**(14), 140403 (2013).

[113] S. Nußmann, K. Murr, M. Hijlkema, B. Weber, A. Kuhn, and G. Rempe. Vacuum-Stimulated Cooling of Single Atoms in Three Dimensions. *Nat. Phys.* **1**(2), 122–125 (2005).

[114] I. Bloch. Ultracold Quantum Gases in Optical Lattices. *Nat. Phys.* **1**, 23–30 (2005).

[115] I. Bloch, J. Dalibard, and W. Zwerger. Many-Body Physics with Ultracold Gases. *Rev. Mod. Phys.* **80**(3), 885–964 (2008).

[116] A. Kubanek, M. Koch, C. Sames, A. Ourjoumtsev, P. W. H. Pinkse, K. Murr, and G. Rempe. Photon-by-Photon Feedback Control of a Single-Atom Trajectory. *Nature* **462**, 898–901 (2009).

[117] J. D. Thompson, T. G. Tiecke, N. P. de Leon, J. Feist, A. V. Akimov, M. Gullans, A. S. Zibrov, V. Vuletić, and M. D. Lukin. Coupling a Single Trapped Atom to a Nanoscale Optical Cavity. *Science* **340**(6137), 1202–1205 (2013).

[118] T. Kampschulte, W. Alt, S. Manz, M. Martinez-Dorantes, R. Reimann, S. Yoon, D. Meschede, M. Bienert, and G. Morigi. Electromagnetically-Induced-Transparency Control of Single-Atom Motion in an Optical Cavity. *Phys. Rev. A.* **89**(3), 033404 (2014).

[119] A. M. Kaufman, B. J. Lester, C. M. Reynolds, M. L. Wall, M. Foss-Feig, K. R. A. Hazzard, A. M. Rey, and C. A. Regal. Two-Particle Quantum Interference in Tunnel-Coupled Optical Tweezers. *Science* **345**(6194), 306–309 (2014).

[120] T. Müller, S. Fölling, A. Widera, and I. Bloch. State Preparation and Dynamics of Ultracold Atoms in Higher Lattice Orbitals. *Phys. Rev. Lett.* **99**(20), 200405 (2007).

[121] M. Mcdonald, B. H. Mcguyer, G. Z. Iwata, and T. Zelevinsky. Thermometry via Light Shifts in Optical Lattices. *Phys. Rev. Lett.* **114**(2), 023001 (2015).

[122] D. Leibfried, R. Blatt, C. Monroe, and D. Wineland. Quantum Dynamics of Single Trapped Ions. *Rev. Mod. Phys.* **75**(1), 281–324 (2003).

[123] H. J. Metcalf and P. van der Straten, *Laser Cooling and Trapping* (Springer, 1999).

[124] L. Förster, M. Karski, J.-M. Choi, A. Steffen, W. Alt, D. Meschede, A. Widera, E. Montano, J. H. Lee, W. Rakreungdet, and P. Jessen. Microwave Control of Atomic Motion in Optical Lattices. *Phys. Rev. Lett.* **103**(23), 233001 (2009).

[125] X. Li, T. A. Corcovilos, Y. Wang, and D. S. Weiss. 3D projection Sideband Cooling. *Phys. Rev. Lett.* **108**(10), 103001 (2012).

[126] G. Raithel, G. Birkl, W. Phillips, and S. Rolston. Compression and Parametric Driving of Atoms in Optical Lattices, 1997.

[127] M. Morinaga, I. Bouchoule, J.-C. Karam, and C. Salomon. Manipulation of Motional Quantum States of Neutral Atoms. *Phys. Rev. Lett.* **83**(20), 4037–4040 (1999).

[128] I. Bouchoule, H. Perrin, A. Kuhn, M. Morinaga, and C. Salomon. Neutral Atoms Prepared in Fock States of a One-Dimensional Harmonic Potential. *Phys. Rev. A* **59**(1), R8–R11 (1999).

[129] C. Tuchendler, A. Lance, A. Browaeys, Y. Sortais, and P. Grangier. Energy Distribution and Cooling of a Single Atom in an Optical Tweezer. *Phys. Rev. A* **87**(3), 033425 (2008).

[130] H. Perrin, A. Kuhn, I. Bouchoule, and C. Salomon. Sideband Cooling Of Neutral Atoms In A Far-Detuned Optical Lattice. *Europhys. Lett.* **42**(4), 395–400 (1998).

[131] C. Monroe, D. M. Meekhof, B. E. King, and D. J. Wineland. A "Schrodinger Cat" Superposition State of an Atom. *Science* **272**(5265), 1131–1136 (1996).

[132] P. Richerme, Z.-X. Gong, A. Lee, C. Senko, J. Smith, M. Foss-Feig, S. Michalakis, A. V. Gorshkov, and C. Monroe. Non-local propagation of correlations in quantum systems with long-range interactions. *Nature* **511**(7508), 198–201 (2014).

[133] F. Schmidt-Kaler, H. Häffner, M. Riebe, S. Gulde, G. P. T. Lancaster, T. Deuschle, C. Becher, C. F. Roos, J. Eschner, and R. Blatt. Realization of the Cirac-Zoller controlled-NOT quantum gate. *Nature* **422**(6930), 408–411 (2003).

[134] S. D. Bartlett, H. de Guise, and B. C. Sanders. Quantum Encodings in Spin Systems and Harmonic Oscillators. *Phys. Rev. A* **65**(5), 052316 (2002).

[135] K. Eckert, J. Mompart, X. X. Yi, J. Schliemann, D. Bruss, G. Birkl, and M. Lewenstein. Quantum Computing in Optical Microtraps Based on the Motional States of Neutral Atoms. *Phys. Rev. A* **66**(4), 042317 (2002).

[136] P. I. Schneider and A. Saenz. Quantum Computation with Ultracold Atoms in a Driven OpticalLlattice. *Phys. Rev. A* **85**(5), 050304(R) (2012).

[137] A. S. Parkins and H. J. Kimble. Quantum State Transfer Between Motion and Light. *J. Opt. B* **1**, 496–504 (1999).

[138] A. S. Parkins and H. J. Kimble. Position-Momentum Einstein-Podolsky-Rosen State of Distantly Separated Trapped Atoms. *Phys. Rev. A* **61**(5), 052104 (2000).

[139] E. Hutchisson. Band Spectra Intensities for Symmetric Diatomic Molecules. *Phys. Rev.* **36**(3), 410–420 (1930).

[140] W. L. Smith. The Overlap Integral of Two Harmonic-Oscillator Wave Functions. *J. Phys. B* **2**(1), 1–4 (1969).

[141] A. Görlitz, M. Weidemüller, T. W. Hänsch, and A. Hemmerich. Observing the Position Spread of Atomic Wave Packets. *Phys. Rev. Lett.* **78**(11), 2096–2099 (1997).

[142] N. Poli, R. J. Brecha, G. Roati, and G. Modugno. Cooling Atoms in an Optical Trap by Selective Parametric Excitation. *Phys. Rev. A* **65**(2), 021401 (jan 2002).

[143] H. P. Yuen. Two-Photon Coherent States of the Radiation Field. *Phys. Rev. A* **13**(6), 2226–2243 (1976).

[144] P. Dirac, *The Principles of Quantum Mechanics* (Clarendon Press, 1981) 4th editio ed.

[145] G. Magyar and L. Mandel. Interference Fringes Produced by Superposition of Two Independent Maser Light Beams. *Nature* **198**, 255–256 (1963).

[146] R. J. Glauber. One Hundred Years of Light Quanta. *Rev. Mod. Phys.* **78**(4), 1267–1278 (2006).

[147] G. Raithel, G. Birkl, A. Kastberg, W. D. Phillips, and S. L. Rolston. Cooling and Localization Dynamics in Optical Lattices. *Phys. Rev. Lett.* **78**(4), 630–633 (1997).

[148] C. Weitenberg, P. Schauß, T. Fukuhara, M. Cheneau, M. Endres, I. Bloch, and S. Kuhr. Coherent Light Scattering from a Two-Dimensional Mott Insulator. *Phys. Rev. Lett.* **106**(21), 215301 (2011).

[149] K. Baumann, C. Guerlin, F. Brennecke, and T. Esslinger. Dicke Quantum Phase Transition with a Superfluid Gas in an Optical Cavity. *Nature* **464**(7293), 1301–6 (2010).

[150] S. Bux, C. Gnahm, R. A. W. Maier, C. Zimmermann, and P. W. Courteille. Cavity-Controlled Collective Scattering at the Recoil Limit. *Phys. Rev. Lett.* **106**(20), 203601 (2011).

[151] B. Casabone, A. Stute, K. Friebe, B. Brandstätter, K. Schüppert, R. Blatt, and T. E. Northup. Heralded Entanglement of two Ions in an Optical Cavity. *Phys. Rev. Lett.* **111**(10), 100505 (2013).

[152] M. Tavis and F. W. Cummings. Exact Solution for an N-MoleculeRadiation-Field Hamiltonian. *Phys. Rev.* **170**(2), 379–384 (1968).

[153] Q.-H. Chen, T. Liu, Y.-Y. Zhang, and K.-L. Wang. Quantum Phase Transitions in Coupled Two-Level Atoms in a Single-Mode Cavity. *Phys. Rev. A* **82**(5), 053841 (nov 2010).

[154] Y.-Q. Zhang, L. Tan, and P. Barker. Effects of Dipole-Dipole Interaction on the Transmitted Spectrum of Two-Level Atoms Trapped in an Optical Cavity. *Phys. Rev. A* **89**(4), 043838 (2014).

[155] G. Rempe, H. Walther, and N. Klein. Observation of Quantum Collapse and Revival in a One-Atom Maser. *Phys. Rev. Lett.* **58**(4), 353–356 (1987).

[156] K. M. Birnbaum, A. Boca, R. Miller, A. D. Boozer, T. E. Northup, and H. J. Kimble. Photon Blockade in an Optical Cavity with one Trapped Atom. *Nature* **436**, 87–90 (2005).

[157] A. Kubanek, A. Ourjoumtsev, I. Schuster, M. Koch, P. Pinkse, K. Murr, and G. Rempe. Two-Photon Gateway in One-Atom Cavity Quantum Electrodynamics. *Phys. Rev. Lett.* **101**(20), 203602 (2008).

[158] I. Schuster, A. Kubanek, A. Fuhrmanek, T. Puppe, P. W. H. Pinkse, K. Murr, and G. Rempe. Nonlinear Spectroscopy of Photons Bound to One Atom. *Nat. Phys.* **4**(5), 382–385 (2008).

[159] R. H. Dicke. Coherence in Spontaneous Radiation Processes. *Phys. Rev.* **93**(1), 99–110 (1954).

[160] M. Gross and S. Haroche. Superradiance: An Essay on the Theory of Collective Spontaneous Emission. *Physics Reports* **93**(5), 301–396 (1982).

[161] Y. Colombe, T. Steinmetz, G. Dubois, F. Linke, D. Hunger, and J. Reichel. Strong Atom Field Coupling for Bose Einstein Condensates in an Optical Cavity on a Chip. *Nature* **450**, 272–276 (2007).

[162] P. M. Alsing, D. A. Cardimona, and H. J. Carmichael. Suppression of Fluorescence in a Lossless Cavity. *Phys. Rev. A* **45**(3), 1793–1803 (1992).

[163] H. Tanji-Suzuki, I. D. Leroux, M. H. Schleier-Smith, M. Cetina, A. T. Grier, J. Simon, and V. Vuletić. Interaction Between Atomic Ensembles and Optical Resonators. Classical Description. *Adv. At. Mol. Opt. Phys.* **60**, 201–237 (2011).

[164] C. Y. Hu, A. Young, J. L. O'Brien, W. J. Munro, and J. G. Rarity. Giant Optical Faraday Rotation Induced by a Single-Electron Spin in a Quantum Dot: Applications to Entangling Remote Spins via a Single Photon. *Phys. Rev. B* **78**(8), 085307 (2008).

[165] R. Hanbury Brown and R. Q. Twiss. A Test of a New Type of Stellar Interferometer on Sirius. *Nature* **178**, 1046–1048 (1956).

[166] H.-J. Briegel, W. Dür, J. I. Cirac, and P. Zoller. Quantum Repeaters: The Role of Imperfect Local Operations in Quantum Communication. *Phys. Rev. Lett.* **81**(26), 5932–5935 (1998).

[167] Y. Lin, J. P. Gaebler, F. Reiter, T. R. Tan, R. Bowler, A. S. Sørensen, D. Leibfried, and D. J. Wineland. Dissipative Production of a Maximally Entangled Steady State of two Quantum Bits. *Nature* **504**, 415–418 (2013).

[168] NIST. Atomic Spectra Database, 2014.

[169] M. S. Safronova and U. I. Safronova. Critically Evaluated Theoretical Energies, Lifetimes, Hyperfine Constants, and Multipole Polarizabilities in 87Rb. *Phys. Rev. A* **83**(5), 052508 (2011).

[170] B. Arora, M. S. Safronova, and C. W. Clark. Magic Wavelengths for the np-ns Transitions in Alkali-metal Atoms. *Phys. Rev. A* **76**(5), 052509 (nov 2007).

[171] M. Greiner, *Ultracold Quantum Gases in Three-Dimensional Optical Lattice*, PhD thesis, LMU München (2003).

Publications

- Interference and Dynamics of Light from a Distance-Controlled Atom Pair in an Optical Cavity
  A. Neuzner, M. Körber, O. Morin, S. Ritter, and G. Rempe
  Nature Photonics (under consideration)

- Breakdown of Atomic Hyperfine Coupling in a Deep Optical-Dipole Trap
  A. Neuzner, M. Körber, S. Dürr, G. Rempe, and S. Ritter
  Physical Review A **92**, 053842 (2015)

- Efficient Generation of Single Photons from an Atom-Cavity System
  M. Mücke, J. Bochmann, C. Hahn, A. Neuzner, C. Nölleke, A. Reiserer, G. Rempe, and S. Ritter
  Physical Review A **87**, 063805 (2013)

- Efficient Teleportation Between Remote Single-Atom Quantum Memories
  C. Nölleke, A. Neuzner, A. Reiserer, C. Hahn, G. Rempe, and S. Ritter
  Physical Review Letters **110**, 140403 (2013)

- Qubits und verschränkte Atome.
  V. Winkler, and A. Neuzner.
  c't - Zeitschrift für Computer und Technik (2012).

- An Elementary Quantum Network of Single Atoms in Optical Cavities
  S. Ritter, C. Nölleke, C. Hahn, A. Reiserer, A. Neuzner, M. Uphoff, M. Mücke, E. Figueroa, J. Bochmann, and G. Rempe.
  Nature **484**, 195–200 (2012).

Acknowledgments

Throughout my time in the Quantum Dynamics division of the Max Planck Institute for Quantum Optics, I had the pleasure to work with many people who I found inspiring as professionals and as human beings. Here, I want to express my gratitude to these people for numerous contributions to the actual project and for maintaining an enjoyable working atmosphere in the group.

I am deeply thankful to my advisor, Prof. Gerhard Rempe, for making this thesis possible and realizing his promise that *"in this group, one is only limited by himself"*. Nothing ever prevented Gerhard from discussing not yet understood results with almost childish joy; in doing so, he many times succeeded to pick up the one loose thread that eventually lead to an explanation. Many of the topics that are covered in this thesis were not foreseen and I am particular thankful for allowing me to also pick these *"flowers by the roadside"*.

When I started my thesis, Dr. Stephan Ritter was my supervisor. His high professional standards made him a valued partner for discussion and his incorruptible moral integrity made him a role model. Working with him was always a pleasure and by the time I finish my thesis, the supervisor has turned into a friend.

Dr. Stephan Dürr is a seemingly endless source of movie trivia, soccer results and some of the most reliable - and even well explained - physics I encountered throughout my studies. He was a reliable climbing partner in steep rock and slippery math.

Operating the complex experimental apparatus would not have been possible without the support of the colleagues with whom I shared the lab. I thank Martin Mücke and Jörg Bochmann for introducing me to the apparatus that they had set up. I vividly recall the long nights shared with Andreas Reiserer, Christian Nölleke and Carolin Hahn during the data collection for the combined experiments - two labs, ten lasers, a hard to quantify number of computers and a giant tangle of BNC cables orchestrated for two single atoms and one photon - that was great fun and will make a good story in the future. I thank Andre Kochanke for his design of the imaging and addressing optics, great music recommendations and his enjoyable laid-back attitude. Quickly after Matthias Körber had joined the experiment, his programming skills had already been proven indispensable for data evaluation. I thank him and Olivier Morin, who

recently joined, for supporting me during the acquisition of the data that is reported in this thesis and wish them the very best for the future on the experiment.

Andre Kochanke and Franko Saworski supported me in the initial development of a versatile radio-frequency source. Matthias Körber then finalized our proof-of-principle code into a stable software and Tom Wiesmeier did a great job in turning a set of loose schematics into a fantastic piece of hardware that can bear comparison with commercial products.

The working atmosphere has been wonderful and I thank all members of the Quantum Dynamics group for sustaining this well-balanced environment.

Studying physics and doing a PhD is a roller-coaster ride. The highs would have been less enjoyable and the lows would have been lower without a kindred spirit to share both. I am very thankful to Simon Baur for a friendship that started on the first day of university and so far has brought us to Russia, Central Asia, the Caucasus, America and England. Thank you, Siona Laverty, for proof reading parts of the final manuscript.

Finally, I would like to thank Eva and my parents for providing a perfect blend of support and distraction.